이학박사 학위논문

Molecular genetic studies on the adaptive strategies of plants in changing environments

환경 변화 속 식물의 적응 전략에 대한
분자 유전학적 연구

2015년 8월

서울대학교 대학원
화학부
박 미 정

Molecular genetic studies on the adaptive strategies of plants in changing environments

환경 변화 속 식물의 적응 전략에 대한 분자 유전학적 연구

지도교수 박 충 모

이 논문을 이학박사학위논문으로 제출함

2015년 6월

서울대학교 대학원

화학부 생화학 전공

박 미 정

박미정의 박사학위논문을 인준함

2015년 8월

위 원 장 이 형 호 (인)

부위원장 박 충 모 (인)

위 원 백 경 희 (인)

위 원 백 남 천 (인)

위 원 배 현 숙 (인)

ABSTRACT

Unlike animals, plants spend their entire lifetime in one position and are unable to escape from the unfavorable environmental conditions. As a consequence, plants have evolved diverse and effective strategies to monitor and adapt to various environmental conditions. For instance, it is well known that controlled cleavage of membrane-bound transcription factors ensures rapid transcriptional responses to abrupt environmental stresses in plants.

In this study, I investigated diverse molecular mechanisms allowing plants to cope with environmental changes.

In **Chapter 1**, I examined the regulatory mechanism of the membrane-bound transcription factor (MTF). NTL6 is a plasma membrane-associated transcription factor and positively regulates drought resistance in *Arabidopsis*. I found that SnRK2.8 directly interacts with NTL6 in the cytoplasm. SnRK2.8 phosphorylates NTL6 primarily at Thr^{142} and SnRK2.8-mediated phosphorylation is required for the nuclear import of NTL6. Futhermore, the drought-resistant phenotype of 35S:*NTL6* transgenic plants was compromised in 35S:*NTL6* X *snrk2.8-1* plants. These observations indicate that SnRK2.8-mediated protein phosphorylation, in addition to a proteolytic processing event, is required for NTL6 function in drought-stress signaling.

In **Chapter 2**, I investigated the roles of *BCD1* in iron homeostasis under osmotic stress. The *BCD1* gene is regulated by the iron availability: induced by excessive iron, but repressed by iron deficiency. It is also induced under osmotic stress conditions such as high salinity and drought. Whereas the activation-tagged mutant *bcd1-1D* accumulated a lower amount of iron, the iron level was elevated in the knockout mutant *bcd1-1*. I also found that the BCD1 protein is localized to the Golgi complex. I propose

that the BCD1 transporter plays a role in the iron homeostasis by reallocating excess iron released from the damaged cells exposed to osmotic stress.

In the study of iron in plants, the conventional histochemical staining methods, such as Perls staining are still widely used. I also adopted Perls staining to determine the localization of iron in *Arabidopsis* in Chapter 2. However, it suffers from relatively poor resolution and detection limit. To improve the detection of iron in plants, in **Chapter 3**, I described a nobel method for high-sensitivity fluorescence imaging of iron, which demonstrates the amount and distribution of iron in plant tissues more precisely than conventional methods.

Changes in day-length accompanied by seasonal changes are one of the major environmental factors that affect flowering time. In *Arabidopsis*, the diurnal control of CONSTANS (CO) accumulation by the circadian clock and light signals is critical for day-length measurement and therefore, for the photoperiodic flowering. While diverse molecular mechanisms are known to regulate the diurnal CO dynamics, it has never been explored whether and how CO itself contributes to this process. In **Chapter 4**, I demonstrated that *CO* undergoes alternative splicing, producing two protein isoforms, the full-size COα that is equivalent to the canonical CO transcription factor and the C-terminally truncated COβ. Notably, I found that COβ, which is resistant to the E3 enzymes, facilitates COα degradation by modulating the accessibility of COα to E3 ubiquitin ligases, providing a self-regulatory role of CO in its own diurnal dynamics.

Keywords: membrane-bound transcription factor, iron homeostasis, fluorescent probe for iron detection, photoperiodic flowering, alternative splicing

Student Number: 2010-20277

CONTENTS

LIST OF FIGURES

LIST OF TABLES

ABBREVIATIONS

ABA	Abscisic acid
ACC	1-Aminocyclopropane-1-carboxylic acid
BCD	BUSH-AND-CHLOROTIC-DWARF
BiFC	Bimolecular fluorescence complementation
BL	Brassinolide
cDNA	Complementary DNA
CHX	Cycloheximide
CO	CONSTANS
C_T	Threshold cycle
DIC	Differential interference contrast
FT	FLOWERING LOCUS T
GA	Gibberellic acid
GFP	Green fluorescence protein
GST	Glutathione S-transferase
GUS	β-glucuronidase
IAA	Indole-3-acetic acid
LDs	Long days
MATE	MULTIDRUG AND TOXIC COMPOUND EXTRUSION
MBP	Maltose-binding protein
MPNBD	7-(4-Methylpiperazin-1-yl)-4-nitrobenzo-2-oxa-1,3-diazole
MS	Murashige and Skoog
MTF	Membrane-bound transcription factor
NAC	NAM/ATAF1/2/CUC2
PAC	Paclobutrazol
PET	Photoinduced electron transfer

PL	Photoluminescence
qRT	Quantitative reverse transcription
RFP	Red fluorescent protein
RNAi	RNA interference
SA	Salicylic acid
SDs	Short days
SnRK	Snf1-related protein kinases
TBA	Tetrabutyl ammonium
TM	Transmembrane motif
UTR	Untranslated region

CHAPTER 1

Controlled nuclear import of NTL6 transcription factor reveals a cytoplasmic role of SnRK2.8 in drought stress response

ABSTRACT

Controlled proteolytic activation of membrane-anchored transcription factors provides an adaptation strategy that guarantees rapid transcriptional responses to abrupt environmental stresses in both animals and plants. NTL6 is a plant-specific NAM/ATAF1/2/CUC2 (NAC) transcription factor that is expressed as a dormant plasma membrane-associated form in *Arabidopsis*. Proteolytic processing of NTL6 is triggered by abiotic stresses and abscisic acid. In the present study, I show that NTL6 is linked directly with Snf1-related protein kinase (SnRK) 2.8-mediated signalling in inducing a drought-resistance response. SnRK2.8 phosphorylates NTL6 primarily at Thr^{142}. NTL6 phosphorylation by SnRK2.8 is required for its nuclear import. Accordingly, a mutant NTL6 protein, in which Thr^{142} was mutated to an alanine, was poorly phosphorylated and failed to enter the nucleus. In accordance with the role of SnRK2.8 in drought-stress signalling, transgenic plants overproducing either NTL6 or its active form 6ΔC (35S:*NTL6* and 35S:*6ΔC*) exhibited enhanced resistance to water-deficit conditions such as those overproducing SnRK2.8 (35S:*SnRK2.8*). In contrast, *NTL6* RNA interference (RNAi) plants were susceptible to dehydration as observed in the *SnRK2.8*-deficient *snrk2.8-1* mutant. Furthermore, the dehydration-resistant phenotype of 35S:*NTL6* transgenic plants was compromised in 35S:*NTL6* X *snrk2.8-1* plants. These observations indicate that SnRK2.8-mediated protein phosphorylation, in addition to a proteolytic processing event, is important for NTL6 function in inducing a drought-resistance response.

INTRODUCTION

Structural mechanisms for abscisic acid (ABA) perception and downstream signalling schemes have been characterized previously (Fujii *et al*., 2009; Ma *et al*., 2009; Melcher *et al*., 2009; Umezawa *et al*., 2010). The PYRABACTIN RESISTANCE 1 (PYR1) protein, a member of the star-related lipid-transfer (START) domain protein family, binds ABA and functions in earlier steps of ABA signalling (Fujii *et al*., 2009; Melcher *et al*., 2009). The ABA-bound PYR1 protein disrupts the interactions between Snf1-related protein kinases (SnRKs) and protein phosphatase 2C (PP2C). PYR1 inhibition of SnRK2 dephosphorylation by PP2C activates downstream events of ABA signalling (Fujii *et al*., 2007; Fujii *et al*., 2009; Park *et al*., 2009; Hubbard *et al*., 2010; Weiner *et al*., 2010), suggesting that SnRK2s are critical components of ABA receptor complexes.

The *Arabidopsis* genome contains ten SnRK2 members (Hrabak *et al*., 2003), and a few members have been functionally characterized. Consistent with the potential roles of SnRK2s in ABA signalling, it has been demonstrated that SnRK2.2, SnRK2.3, SnRK2.6 and SnRK2.8 are involved in plant responses to drought stress (Mustilli *et al*., 2002; Yoshida *et al*., 2002; Umezawa *et al*., 2004; Belin *et al*., 2006; Yoshida *et al*., 2006; Nakashima *et al*., 2009; Fujita *et al*., 2009). Upon exposure to drought conditions, they are likely to be nuclear-localized and phosphorylate ABA-responsive element (ABRE)-binding factors (ABFs) (Mizoguchi *et al*., 2010; Yoshida *et al*., 2010), indicating that they are intimately linked to gene transcriptional control. Consequently, overproduction of the transcription factor ABF2 does not lead to alterations in phenotypes and downstream gene expression without ABA-mediated protein phosphorylation (Uno *et al*., 2000). In addition, SnRK2.1/2.3/2.6 kinases also phosphorylate membrane proteins, such as POTASSIUM CHANNEL IN *ARABIDOPSIS THALIANA* 1 (KAT1),

SLOW ANION CHANNEL-ASSOCIATED 1 (SLAC1) and NADPH oxidase F (AtrbohF) (Geiger *et al*., 2009; Lee *et al*., 2009; Sato *et al*., 2009; Sirichandra *et al*., 2009; Vahisalu *et al*., 2010), further extending the repertoire of the SnRK2 targets.

Several transcription factors in plants, including the basic leucine zipper (bZIP) and NAM/ATAF1/2/CUC2 (NAC) members, are membrane-associated (Iwata and Koizumi, 2005; Kim *et al*., 2006; Liu *et al*., 2007a; Liu *et al*., 2007b; Seo *et al*., 2008). The membrane-bound transcription factors (MTFs) are released from the membranes through proteolytic cleavage under environmental stress conditions (Seo *et al*., 2008). Transgenic plants overproducing transcriptionally active MTF forms exhibit enhanced tolerance to endoplasmic reticulum stress (Liu *et al*., 2007a), high salinity (Liu *et al*., 2007b) and pathogen infection (Seo *et al*., 2010). It is now perceived that controlled proteolytic activation of MTFs is an adaptive strategy ensuring prompt transcriptional responses to environmental stimuli (Seo *et al*., 2008).

It has been recently reported that a plasma membrane-associated NAC transcription factor NTL6 plays a role in the cold induction of the pathogen-resistance response (Seo *et al*., 2010). Low temperatures trigger proteolytic cleavage of the NTL6 protein, and the processed NTL6 form enters the nucleus, where it regulates expression of *PATHOGENESIS-RELATED* (*PR*) genes. Notably, ABA also activates NTL6 processing, and transgenic plants overproducing a nuclear NTL6 form (35S:*6ΔC*) are hypersensitive to ABA (Kim *et al*., 2007; Seo and Park, 2010), suggesting that NTL6 is related to ABA signalling. A fundamental question as to the NTL6 function, and other MTFs as well, is whether membrane release is sufficient for its nuclear import and thus its physiological role.

In the present study, I demonstrate that SnRK2.8 phosphorylates

NTL6 in the cytoplasm. NTL6 phosphorylation by SnRK2.8 is necessary for its nuclear import and regulatory role in the drought-resistance response, revealing a cytoplasmic role for SnRK2.8 in ABA signalling.

MATERIALS AND METHODS

Plant materials and growth conditions

The *Arabidopsis thaliana* lines used were on the Col-0 background. Plants were grown in a controlled culture room set at 23◦C under long day conditions (16 h light/8 h dark) with white light illumination (120 μmol photons/m^2s). The *NTL6*-overexpressing transgenic plants and *NTL6* RNA interference (RNAi) plants have been described previously (Seo *et al*., 2010).

Drought-stress treatment

Drought stress was imposed on 2-week-old plants grown in soil using 36 cm^3 soil pots by halting watering. To prevent direct air-drying of seedlings, small pores were made in the plastic cover 7 days following the start of drought treatments, and the cover was removed 7 days later. Watering was reinitiated after 20 days, and the survival rates were calculated for each group of plants. To avoid experimental variations, the same numbers of each plant group were grown in the same tray. Three independent measurements, each consisting of 50 plants, were averaged.

For water loss assays, the 4th−7th leaves were detached from 4-week-old plants and put on 3MM paper at room temperature (23-25^{o}C) for the indicated time periods, and the fresh masses of the leaves were measured using a Sartorius Analytical Balance with a readability of 0.01 mg (DE/CP-225D). The leaves from seven plants were measured and averaged for each plant group.

Transcript level analysis

Quantitative real-time reverse transcription PCR (qRT-PCD) was employed for measuring transcript levels. Extraction of total RNA samples from appropriate plant materials and the reverse transcription PCR conditions have

been described previously (Seo *et al*., 2010). Total RNA samples were pre-treated extensively with an RNAse-free DNAse to eliminate any contaminating genomic DNA before use.

qRT-PCR was carried out in 96-well blocks with an Applied Biosystems 7500 Real-Time PCR system using the SYBR Green I master mix in a volume of 25 μl. The PCR primers were designed using the Primer Express Software installed into the system and are listed in Table 1. The two-step thermal cycling profile used was 15 s at 94^{o}C and 1 min at 68^{o}C. *eIF4A* [eukaryotic initiation factor 4A; tair (The *Arabidopsis* Genome Initiative) accession number At3g13920] was included in the assays as an internal control for normalizing the variations in amounts of cDNA used (Gutierrez *et al*., 2008). The qRT-PCRs were carried out in biological triplicates using total RNA samples extracted from three independent plant materials grown under identical growth conditions. The comparative $\Delta\Delta C_T$ method was used to evaluate the relative quantities of each amplified product in the samples. The threshold cycle (C_T) was automatically determined for each reaction by the system set with default parameters. The specificity of the PCR was determined by melt curve analysis of the amplified products using the standard method installed in the system.

Subcellular localization assays

A green fluorescent protein (GFP)-encoding sequence was fused in-frame to the 5'-ends of *NTL6*, and the gene fusions were subcloned into the p2FGW7 expression vector (Invitrogen). Protoplasts were prepared from well-expanded leaves of 4-week-old plants (Yoo *et al*., 2007). Approximately 2×10^4 protoplasts were mixed with 10 μg of plasmid DNA and 110 μl of poly (ethyleneglycol) (PEG)-calcium transfection solution [40% (w/v) PEG 4000, 0.2 M mannitol and 100 mM $CaCl_2$]. After incubation at 22^{o}C for 20 min, the transfection mixture was washed with W5 solution [154 mM NaCl, 125

mM $CaCl_2$, 5 mM KCl, 2 mM MES (pH 5.7) and 5 mM glucose] and centrifuged at 100 g for 2 min. Protoplasts were resuspended in 1 ml of WI solution [0.5 M mannitol, 4 mM MES (pH 5.7) and 20 mM KCl] and incubated in the dark at 22°C for 12−15 h. Subcellular distribution was visualized by differential interference contrast (DIC) microscopy and fluorescence microscopy.

Preparation of recombinant proteins

The *SnRK2.8* gene was fused in-frame either to the 5'-end of the maltose-binding protein (MBP)-encoding sequence in the pMBP-GW vector or to the 5'-end of the glutathione S-transferase (GST)-encoding sequence in the pET41a(+) vector. The *NTL6* gene sequences were similarly cloned into the pMBP-GW vector. The expression constructs were transformed into *Escherichia coli* strain BL21 cells. NTL proteins were also similarly produced in *E. coli* cells as MBP fusions. Cell cultures, induction and purification were carried out according to the manufacturer's instructions (Novagen). The *NTL6* and *SnRK2.8* genes were mutated by PCR using gene-specific primers with altered sequences (Table 2).

***In vitro* pull-down assays**

Recombinant GST−SnRK2.8 proteins were produced in *E. coli* BL21-CodonPlus (DE3)-RIL strains (Stratagene) and purified as follows. A one-tenth volume of precultured cells (5 ml) was added to 500 ml of fresh Luria−Bertani (LB) medium and cultured at 37°C until OD_{600} reached 0.3-0.6. Protein production was induced by adding isopropyl-β-D-thiogalacto-pyranoside (IPTG) at a final concentration of 0.5 mM and shaking at 37°C for 5 h. Cells were harvested and resuspended in buffer A [25 mM HEPES (pH 7.5), 20% glycerol, 1 mM dithiothreitol (DTT), 100 mM NaCl, 0.2 mM EDTA with protease inhibitor cocktail (Sigma-Aldrich), and 1 mM PMSF].

The cells were lysed using a French press [8500 psi (1 psi=6.9 kPa), once], sonicated for 30 s twice and centrifuged at 20000 g for 20 min. The supernatants were stored at -80°C until used.

The *NTL6* gene was subcloned into the pGADT7 vector. The NTL6 polypeptide was labelled with ^{35}S-methionine using the T_NT coupled reticulocyte lysate system (Promega). The GST−SnRK2.8 proteins were mixed with glutathione-agarose beads (Sigma-Aldrich) and agitated for 15 min at room temperature. The beads were washed three times with 1× PBS buffer and once with buffer A. ^{35}S-Labelled proteins (5 μl) were added and incubated for 2 h at 4°C. The beads were then washed five times with fresh buffer A. The bound proteins were eluted with 1× SDS loading buffer by boiling for 5 min at 100°C and subjected to SDS/PAGE (10% gel) and autoradiography.

Bimolecular fluorescence complementation (BiFC) assays

BiFC assays were carried out by co-transfection of nYFP-NTL6 and cYFP-SnRK2.8 vectors or vice versa into the *Arabidopsis* mesophyll protoplasts as described previously (Yoo *et al*., 2007). After incubation at room temperature for 16 h, reconstitution of yellow fluorescent protein (YFP) fluorescence was observed using a confocal microscope with the following YFP filter set up: excitation 515 nm, 458/514 dichroic and emission 560−615 BP filter.

Transcriptional activation activity assays

The pMin35S reporter plasmid contains a minimal cauliflower mosaic virus (CaMV) 35S promoter (a -56 to -8 sequence region including the TATA box) and the *β-glucuronidase* (*GUS*). The pNAC-BS reporter plasmid includes a NAC transcription factor-binding sequence (CAGTCTTG*CGT*GTT-GGAACACGCATGTAGT) upstream of the CaMV 35S minimal promoter.

To construct effector plasmids, the *NTL6* gene sequences were inserted into a plant expression vector containing the CaMV 35S promoter. The reporter and effector plasmids were co-transformed into *Arabidopsis* protoplasts. GUS activity was measured by a fluorimetric method as described previously (Jefferson *et al*., 1987). A luciferase (LUC) expression construct was also co-transformed as an internal control. The LUC assays were performed using the Luciferase Assay System kit (Promega).

***In vivo* phosphorylation assays**

The 35S:*NTL6* transgenic plants grown for 2 weeks on Murashige and Skoog (MS) agar plates were used for growth hormone treatments. Harvested plant materials were ground in liquid nitrogen, and total cellular extracts were analysed by SDS/PAGE (10%) and blotted on to Hybond-P+ membranes (Amersham Pharmacia). The blots were hybridized with an anti-MYC antibody (Santa Cruz Biotech). The in-gel kinase assays were carried out as described previously (Fujii *et al*., 2007).

***In vitro* phosphorylation assays**

The *in vitro* phosphorylation assays were carried out as described previously (Klimczak *et al*., 1992) in 10 μl of kinase reaction buffer [20 mM HEPES (pH 7.4), 10 mM $MgCl_2$, 1mM Na_3VO4, 2mM DTT, 0.5mM PMSF and 2mM EDTA]. Purified recombinant kinase and NTL6 proteins were added to the reaction mixture supplemented with 1 μCi of [γ-^{32}P]ATP. The reaction mixtures were incubated at 30^{o}C for 30 min and terminated by adding 4 μl of 6×SDS sample loading buffer. The mixtures were boiled for 5 min and loaded on to SDS-PAGE gels (10% gels). The gels were dried under vacuum and subject to autoradiography.

Two-dimensional gel electrophoresis (2-DE) analysis

Whole plants (2-week-old) grown on MS agar plates were ground in liquid nitrogen. Approximately 2 mg of total proteins was dissolved in 400 μl of rehydration buffer (9 M urea, 4% CHAPS, 100 mM DTT and 0.2% Bio-Lyte) and loaded on to a immobilized pH gradient (IPG) gel strip. After active rehydration for 12 h at 50 V, isoelectric focusing (IEF) was performed using a PROTEIN IEF cell at 10 kV to reach 60 kVh. After focusing, the strip was exposed to equilibrium buffer [6 M urea, 20% glycerol, 0.375 M Tris/HCl (pH 8.8) and 2% SDS] containing 130 mM DTT for 20 min followed by soaking in the same buffer containing 135 mM iodoacetamide. After electrophoresis in the second dimension on a 12% gel, the gel was blotted on to Hybond-P+ membranes (Amersham Pharmacia). The blots were hybridized with an anti-MYC antibody.

Primer	Usage	Sequence (5′→3′)
eIF4a-F	qRT-PCR	TGACCACACAGTCTCTGCAA
eIF4a-R	qRT-PCR	ACCAGGGAGACTTGTTGGAC
SnRK2.8-F	qRT-PCR	CCTGAAGTGCTCTCCACGAA
SnRK2.8-R	qRT-PCR	GCATTCATCCGAAACTCGAA
SnRK2.6-F	qRT-PCR	GATCCCGAGGAACCAAAGAA
SnRK2.6-R	qRT-PCR	ATCCTCTTTGCAGGGTCAGC
RD26-F	qRT-PCR	CCCAATAGAGTAGCCGGGTC
RD26-R	qRT-PCR	AGTGCCTTTGGGAGCTTTTC
COR15A-F	qRT-PCR	GCAGATGGTGAGAAAGCGAA
COR15A-R	qRT-PCR	GGCATCCTTAGCCTCTCCTG

Table 1. Primers used in the study

qRT-PCR primers were designed using the Primer Express software installed on the Applied Biosystems 7500 Real-Time PCR system. The sizes of PCR products ranged from 80 to 150 nucleotides in length. F, forward primer; R, reverse primer.

Gene	Mutant	Primer	Sequence (5′→3′)
NTL6	M1	N6-T142A-F	CATGAGTATCGTGCCgctGAGGATGATCTTAGT
		N6-T142A-R	ACTAAGATCATCCTCagcGGCACGATACTCATG
	M2	N6-S147A-F	ACGGAGGATGATCTTgctGGTACCAATCCTGGC
		N6-S147A-R	GCCAGGATTGGTACCagcAAGATCATCCTCCGT
	M3	N6-S174A-F	TTAGGGGAAGAAGATgctAAGTCAGATGAAGTT
		N6-S174A-R	AACTTCATCTGACTTagcATCTTCTTCCCCTAA
	M4	N6-S176A-F	GAAGAAGATTCGAAGgctGATGAAGTTGAAGAA
		N6-S176A-R	TTCTTCAACTTCATCagcCTTCGAATCTTCTTC
	pMBP-GW	N6-GW-F	AAAAAGCAGGCTTC*ATG*AATCAGAATCTTCATGTATTATCA
		N6-GW-R	AGAAAGCTGGGTT*TCA*GGACACTGCAGATGCTCTGAA
SnRK2.8	S154A/T158A	m2.8-F	AGGAGTTCTTCATgctCAACCAAAGgctACAGTAGGA
		m2.8-R	TCCTACTGTagcCTTTGGTTGagcATGAAGAACTCCT
	pMBP-GW	2.8-GW-F	AAAAAGCAGGCTTC*ATG*GAGAGGTACGAAATAGTG
		2.8-GW-R	AGAAAGCTGGGTT*TCA*CAAAGGGGAAAGGAGATC

Table 2. Oligonucleotides used to mutate NTL6 and SnRK2.8

Lower case letters indicate mutated residues and italic letters indicate start or stop codons.

RESULTS

NTL6 promotes dehydration resistance

The *NTL6* gene is induced by ABA and abiotic stresses, such as cold, salt and drought (Kim *et al*., 2007). In addition, proteolytic processing of NTL6 is triggered by ABA (Kim *et al*., 2007), and seed germination of transgenic plants (35S:*6ΔC*) overproducing a truncated NTL6 form (6ΔC consisting of residues 1−329) is hypersensitive to ABA (Seo and Park, 2010) (Figure 1), suggesting that the *NTL6* gene is involved in the drought-stress response.

I examined responses of 35S:*6ΔC* transgenic plants and *NTL6* RNAi plants to drought stress. Although the 35S:*6ΔC* transgenic plants showed enhanced drought resistance, the *NTL6* RNAi transgenic plants were susceptible to drought stress (Figures 2A, 2B and 3). Notably, transgenic plants overexpressing a *MYC-NTL6* gene fusion (35S:*NTL6*), in which a MYC-coding sequence was fused in-frame to the 5'-end of the *NTL6* gene (Seo *et al*., 2010), also exhibited enhanced drought resistance without visible growth defects, although its survival rate was slightly lower than that of the 35S:*6ΔC* transgenic plants. To minimize indirect effects of drought stress caused by growth defects in the 35S:*6ΔC* transgenic plants, leaves were detached from the plants and incubated at room temperature. Water loss assays also showed that the rate of water loss of the 35S:*6ΔC* and 35S:*NTL6* transgenic leaves were lower, whereas that of the RNAi leaves were higher compared with that of the Col-0 leaves (Figure 2C). Consistently, germination of the 35S:*NTL6* and 35S:*6ΔC* transgenic seeds was also hypersensitive to ABA (Figures 1 and 4), supporting the fact that the *NTL6* gene is a component of ABA signalling that mediates the drought-stress response.

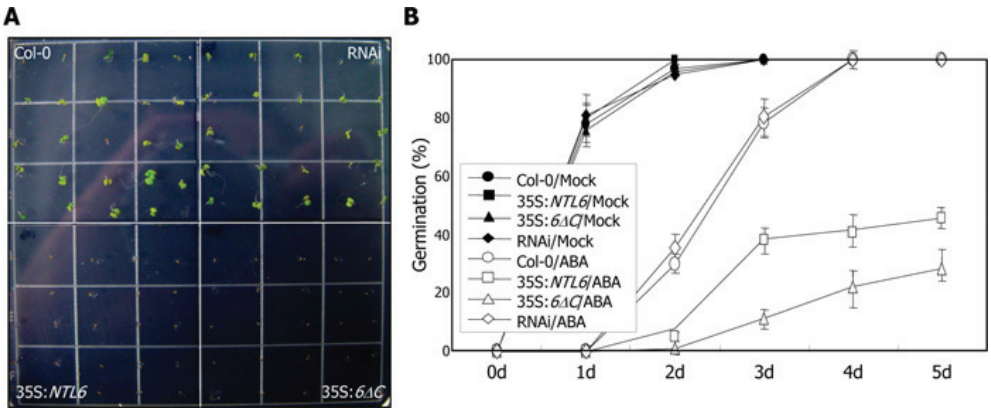

Figure 1. Germination responses of 35S:*NTL6* and 35S:*6ΔC* transgenic and RNAi seeds to ABA

Seeds air-dried for 2 weeks after harvesting were imbibed at 4°C on 1/2× MS agar plates for 3 days and allowed to germinate at 22°C under long days. The appearance of visible radicles was used as a morphological marker for seed germination. The 35S:*NTL6* transgenic plants overexpressing a *MYC-NTL6* gene fusion and the 35S:*6ΔC* transgenic plants overexpressing a truncated *NTL6* gene encoding residues 1-329, and the RNAi plants have been described previously (Seo *et al*., 2010).

(**A**) Seed germination on MS agar plates supplemented with 1 μM ABA. Seeds were photographed 3 days after cold imbibition.

(**B**) Germination percentages. Three measurements, each consisting of 50−70 seeds, were averaged and error bars indicate S.E.M.. d, days after cold imbibition.

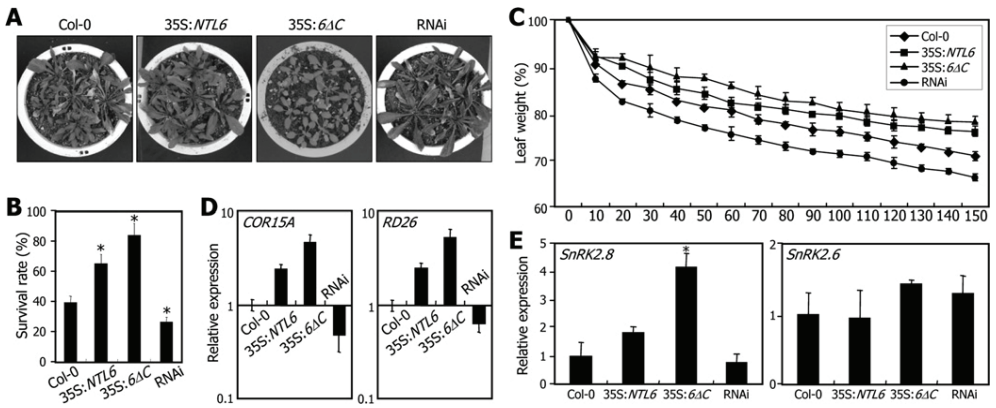

Figure 2. Enhanced drought resistance in NTL6-overexpressing plants

The 35S:*NTL6* transgenic plants overexpressing a MYC-NTL6 fusion and the 35S:*6ΔC* transgenic plants overexpressing a truncated NTL6 form (residues 1-329) have been described previously (Seo *et al*., 2008).

(**A**) Drought-stress responses. Drought was imposed on 2-week-old plants grown in soil by halting watering for 20 days. Plants were rewatered for 3 days before taking photographs.

(**B**) Survival rates. Three independent measurements, each consisting of 30 plants, were averaged for each plant group. Error bars indicate the S.E.M. (Student's *t* test, **P*<0.05).

(**C**) Water loss assays. The 4th−7th leaves of 4-week-old plants were detached and put on 3MM paper at room temperature for the indicated time periods (min). The fresh masses of the leaves were measured and averaged and the error bars indicate S.E.M.

(**D**) Expression of the *COR15A* and *RD26* genes.

(**E**) Expression of the *SnRK2.6* and *SnRK2.8* genes. In (**D**) and (**E**), transcript levels were determined by qRT-PCR using total RNA samples extracted from 2-week-old whole plants grown on MS agar plates. Biological triplicates were averaged. Bars indicate S.E.M. Statistical significance was determined using a Student's *t* test (**P*<0.01).

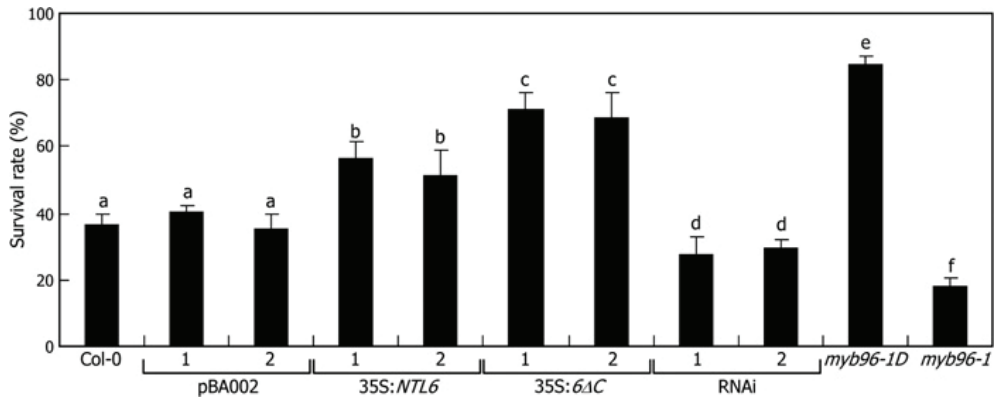

Figure 3. Drought-stress responses of 35S:*NTL6* and 35S:*6ΔC* transgenic and RNAi plants

Drought was imposed on 2-week-old plants grown in soil by halting watering for 20 days. Plants were rewatered for 3 days before measuring survival rates. The *myb96-1D* activation-tagging and *myb96-1* loss-of-function mutants, which have been described previously (Seo *et al*., 2009), were included for comparison. Biological triplicates, each consisting of 30 plants, were averaged and statistically treated using one-way ANOVA with Fisher's post-hoc test ($P<0.01$). Error bars indicate S.E.M. a-f indicate significant differences between columns.

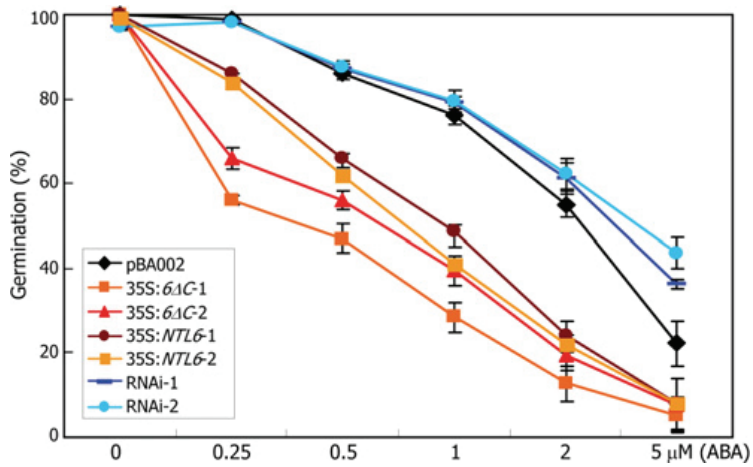

Figure 4. Germination responses to different ABA concentrations

Seeds were germinated for 4 days on MS agar plates containing various concentrations of ABA. Seeds appearance of visible radicles was used as a morphological marker for seed germination. Biological triplicates, each consisting of 50−70 seeds, were averaged and error bars indicate S.E.M.

To look into molecular mechanisms underlying the NTL6 function in the drought-resistance response, I examined expression of ABA- and drought-responsive genes in the 35S:*NTL6* and 35S:*6ΔC* transgenic and RNAi plants. Although the *COR15A* and *RD26* genes were up-regulated in the *NTL6*-overexpressing transgenic plants, they were suppressed in the RNAi plants (Figure 2D). The transcript level of the *COR15A* and *RD26* genes was relatively higher in the 35S:*6ΔC* transgenic plants than in the 35S:*NTL6* transgenic plants, which may be related to the membrane-anchoring of NTL6 (Seo *et al*., 2010). Interestingly, the *SnRK2.8* gene was also induced more than 4-fold in the 35S:*6ΔC* transgenic plants (Figure 2E), suggesting that the *SnRK2.8* gene is transcriptionally regulated by the NTL6 transcription factor. It has been reported that transgenic plants overexpressing the *SnRK2.8* gene (35S:*SnRK2.8*) are drought-resistant, whereas the *SnRK2.8*-deficient *snrk2.8-1* mutant is susceptible to drought stress (Umezawa *et al*., 2004; Mizoguchi *et al*., 2010). Likewise, germination of the 35S:*SnRK2.8* transgenic seeds was significantly delayed by ABA (Figure 5). These observations further support that NTL6 is functionally associated with SnRK2.8 in the drought-stress response.

SnRK2.8 phosphorylates NTL6

One plausible mechanism underlying the relationship between SnRK2.8 and NTL6 activity would be that SnRK2.8 phosphorylates NTL6 and modulates its nuclear import and/or transcriptional activation activity. To examine this hypothesis, I first analysed SnRK2.8-NTL6 protein interactions by *in vitro* pull-down assays using a recombinant GST-SnRK2.8 fusion protein and ^{35}S-labelled NTL6 polypeptide produced by *in vitro* translation. The GST-SnRK2.8 protein interacted with NTL6 (Figure 6A), but GST alone did not exhibit any visible interactions with NTL6. Yeast two-hybrid assays were also employed and β-galactosidase (β-Gal) activities were measured.

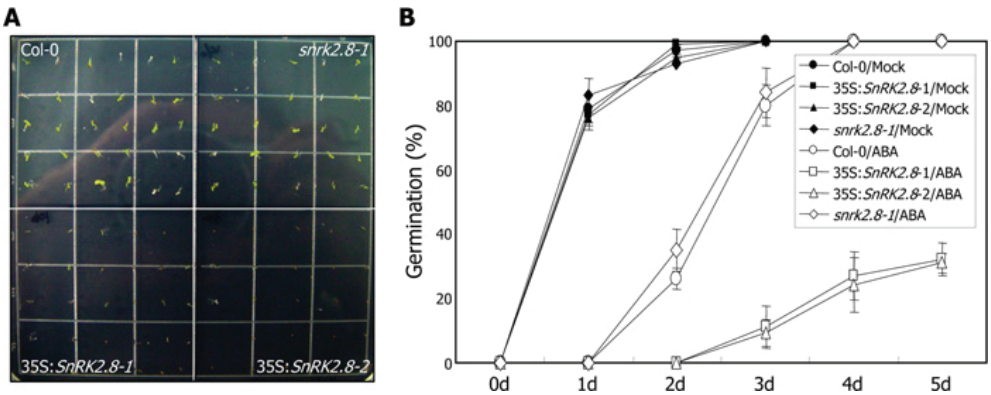

Figure 5. Germination responses of 35S:*SnRK2.8* transgenic and *snrk2.8-1* mutant seeds to ABA

Seeds air-dried for 2 weeks after harvesting were imbibed at 4°C on MS agar plates for 3 days and allowed to germinate at 22°C under long days. The appearance of visible radicles was used as a morphological marker for seed germination.

(**A**) Seed germination on MS agar plates supplemented with 1 μM ABA. Seeds were photographed 3 days after cold imbibition.

(**B**) Germination percentages. Three measurements, each consisting of 50−70 seeds, were averaged and error bars indicate S.E.M. d, days after cold imbibition.

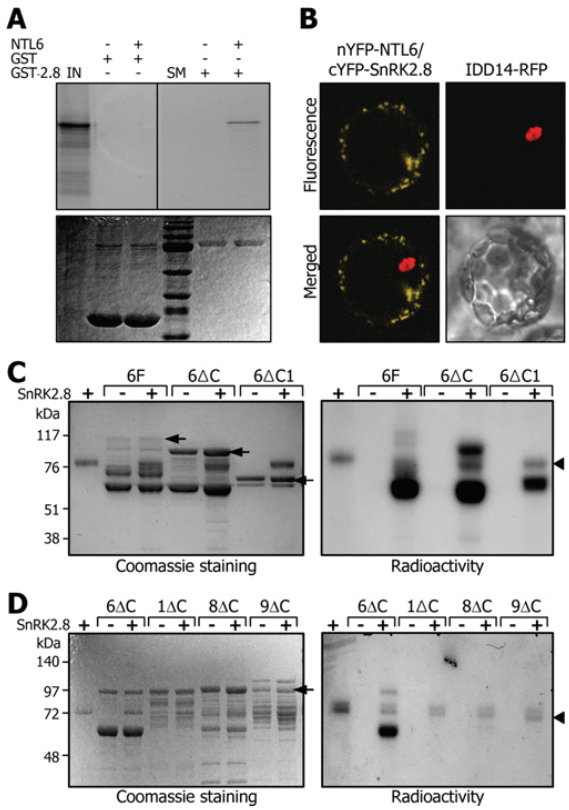

Figure 6. NTL6 phosphorylation by SnRK2.8

(**A**) Interaction of SnRK2.8 with NTL6. A recombinant GST-SnRK2.8 fusion protein (GST-2.8) was incubated with ^{35}S-labelled NTL6 proteins produced by in vitro translation. The proteins were separated by SDS/PAGE (10% gel; lower panel) and subject to autoradiography (upper panel). IN, input; SM, size marker.

(**B**) BiFC assays. Partial YFP fusion constructs were co-expressed transiently in *Arabidopsis* protoplasts. *Arabidopsis* protoplasts were visualized by DIC and fluorescence microscopy. A red fluorescent protein (RFP)-encoding sequence was fused in-frame to the 5'-end of the *INDETERMINATE (ID)-domain 14* (*IDD14*) transcription factor gene, and the *RFP-IDD14* gene fusion was used as a marker for nuclear localization.

(**C**) *In vitro* phosphorylation of NTL6 proteins by SnRK2.8. Recombinant MBP⁻NTL6 fusion proteins, including a full-size NTL6 form (6F) and a couple of truncated NTL6 forms (6ΔC and 6ΔC1), were expressed in *E. coli* cells and partially purified. The recombinant proteins were analysed by SDS-PAGE (10% gel) and Coomassie Blue staining (left-hand panel). The 6ΔC1 form consists of residues 1-180. Arrows indicate full-size forms of individual NTL6 constructs. The SnRK2.8 protein was prepared as a GST fusion in *E. coli* cells. The recombinant NTL6 proteins were subject to in vitro phosphorylation assays (right-hand panel). Arrowhead indicates the autophosphorylated SnRK2.8.

(**D**) *In vitro* phosphorylation assays of NTL proteins. The 6ΔC protein and similarly truncated forms of NTM1, NTL8 and NTL9 (1ΔC containing residues 1-327, 8ΔC containing residues 1-309 and 9ΔC containing residues 1-330) (Kim *et al*., 2006; Kim *et al*., 2007, Yoon *et al*., 2008) were prepared as MBP fusions in *E. coli* cells. The recombinant proteins were analysed by SDS-PAGE (10% gel) and Coomassie Blue staining (left-hand panel). Arrows indicate full-size forms of the NTL proteins. They were subject to *in vitro* phosphorylation assays (right-hand panel). Arrowhead indicates the autophosphorylated SnRK2.8. In (**C**) and (**D**) the molecular mass is given on the left-hand side in kDa.

SnRK2.8 interacted strongly with NTL6 and its truncated form 6ΔC (Figure 7). Among the NTL members, NTL9 is structurally most similar to NTL6, and the *NTL9* gene is induced by drought stress like *NTL6* (Kim *et al.*, 2007). Therefore I examined whether SnRK2.8 also interacts with NTL9. Yeast two-hybrid assays revealed that SnRK2.8 did not interact with NTL9 (Figure 7), supporting the specific interactions between SnRK2.8 and NTL6.

I next examined the SnRK2.8−NTL6 interactions *in vivo* using BiFC assays in *Arabidopsis* protoplasts. Split YFP−SnRK2.8/NTL6 fusions were co-expressed transiently in *Arabidopsis* protoplasts. The results showed that SnRK2.8 interacts with NTL6 (Figures 6B and 8). The fluorescence was detected exclusively in the cytoplasm and not in the nucleus.

To examine NTL6 phosphorylation by SnRK2.8 *in vitro*, I produced several recombinant NTL6 proteins, such as a full-size NTL6 form (6F) and a couple of truncated forms (6ΔC and 6ΔC1 containing 329 and 180 residues respectively) lacking the C-terminal sequence regions containing transmembrane motifs (Seo *et al.*, 2010), in *E. coli* cells and purified by affinity chromatography. The protein preparations always contained smaller polypeptides (Figure 6C, left-hand panel), which may be due to NTL6 processing occurring to some degree in *E. coli* cells. I also produced a recombinant SnRK2.8 protein in a similar manner. The SnRK2.8 protein possessed an autophosphorylation activity (Figure 6C, right-hand panel). The assays revealed that all of the NTL6 proteins are phosphorylated by SnRK2.8.

I next examined whether SnRK2.8 also phosphorylates other NTL proteins, which are structurally analogous to NTL6 in that they are associated with intracellular membranes and activated by proteolytic processing (Kim *et al.*, 2006; Kim *et al.*, 2007; Yoon *et al.*, 2008). A series of truncated forms of NAC WITH TRANSMEMBRANE MOTIF 1 (NTM1), NTL8 and NTL9 (1ΔC, 8ΔC and 9ΔC respectively), which were

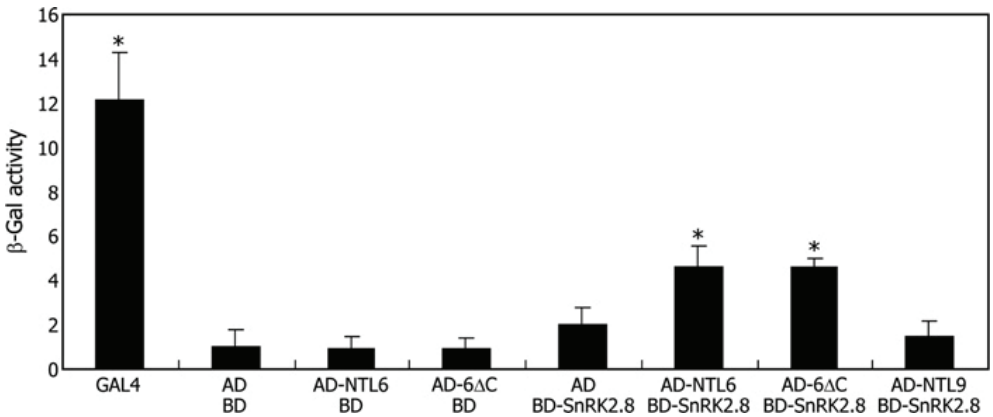

Figure 7. Interactions between SnRK2.8 and NTLs in yeast cells

Cell growth of yeast transformants was quantified. β-Gal activities were normalized by dividing total activity by optical cell density. Three measurements of β-Gal activities were averaged. Statistical significance was determined using a Student's *t* test (**P*<0.05). Error bars indicate S.E.M.

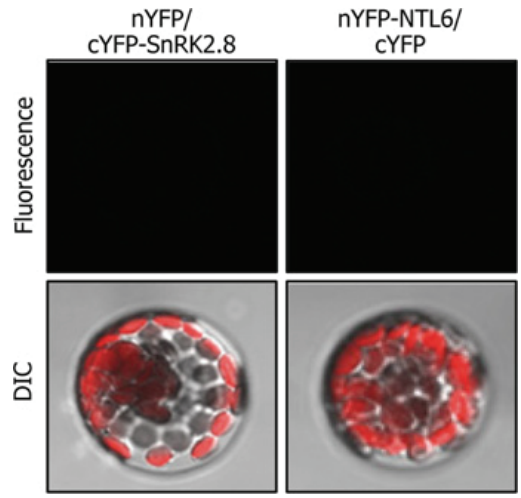

Figure 8. BiFC assays

Partial YFP fusion constructs containing either the *SnRK2.8* or *NTL6* gene were transiently co-expressed in *Arabidopsis* protoplasts and visualized by DIC and fluorescence microscopy. Chloroplasts appear red in the protoplasts because of autofluorescence.

similar in size to 6ΔC, were produced in *E. coli* cells. None of the NTL proteins other than NTL6 were phosphorylated by SnRK2.8 (Figure 6D), demonstrating that SnRK2.8 specifically phosphorylates NTL6.

Substitution of Thr^{142} reduces NTL6 phosphorylation

SnRK2.8 belongs to the serine/threonine kinase superfamily. I found that the NTL6 proteins are phosphorylated at serine/threonine residues present within the N-terminal 180-residue region by SnRK2.8 (Figure 6C). To determine the serine or threonine residues phosphorylated by SnRK2.8, putative target residues were predicted by comparing the N-terminal 180-residue region of NTL6 protein with potential target sequences of serine/threonine kinases. Basophilic kinases, such as SnRK2, preferentially phosphorylate the serine/threonine residues in the R/KXXS/T motifs (Shin *et al.*, 2007). Phosphorylation assays *in vitro* showed that serine/threonine residues, such as Thr^{22}, Ser^{69}, Ser^{83}, Ser^{107} and Thr^{132}, which are present in the R/KXXS/T motifs, are not phosphorylated by SnRK2.8 (Figure 9). It has been reported that even the serine/threonine residues in the S/TXXD/E motifs are also phosphorylated by basophilic kinases in some cases (Kennelly and Krebs, 1991; Zhu *et al.*, 2005). I therefore identified four additional serine/threonine residues belonging to the acidic motifs and mutated them to alanine, resulting in the proteins M1−M4 (Figure 10A).

Recombinant M1−M4 proteins were prepared in *E. coli* cells and subject to *in vitro* phosphorylation assays. The results showed that phosphorylation of M1 protein was significantly reduced by approximately 90%, whereas that of other mutant NTL6 proteins was not affected to a discernible level (Figures 10B and 10C), indicating that Thr^{142} is the primary site for the NTL6 phosphorylation by SnRK2.8.

To examine NTL6 phosphorylation by SnRK2.8 *in vivo*, I transformed the *snrk2.8-1* mutant with the *MYC⁻NTL6* gene fusion, in which

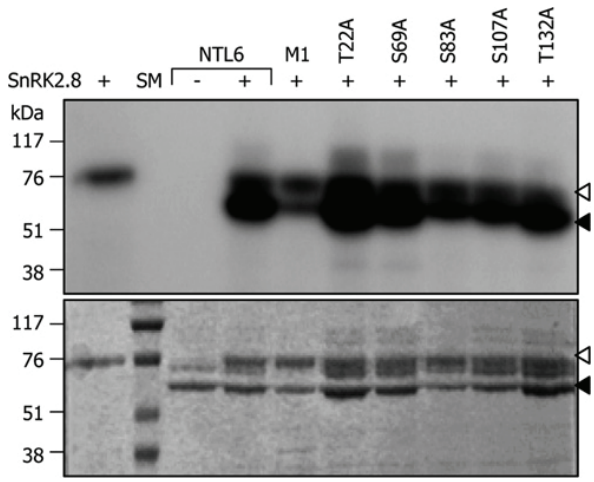

Figure 9. *In vitro* phosphorylation assays of NTL6 proteins

The NTL6 proteins containing a single mutation were prepared as MBP fusions in *E. coli* cells and subject to *in vitro* phosphorylation assays (upper panel). The protein preparations were analysed by SDS-PAGE (10% gel) and Coomassie Blue staining before drying and exposure to X-ray films (lower panel). The white arrowheads indicate SnRK2.8, and the black arrowheads indicate the NTL6 proteins. Molecular mass is shown on the left-hand side in kDa.

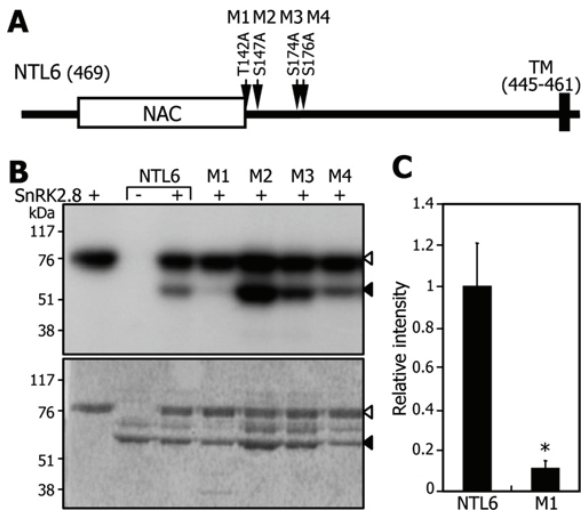

Figure 10. Determination of primary phosphorylation sites in NTL6

(**A**) Predicted phosphorylation residues. The residues were predicted through PROSITE-based searches. The predicted serine (S) and threonine (T) residues were mutated to alanine (A) as indicated, resulting in a series of mutant 6ΔC1 proteins (M1-M4). TM, transmembrane motif.

(**B**) *In vitro* phosphorylation assays. The M1-M4 proteins were prepared as MBP fusions in *E. coli* cells and subject to *in vitro* phosphorylation assays (upper panel). The protein preparations were analysed by SDS-PAGE (10% gel) and Coomassie Blue staining before use (lower panel). The white arrowheads indicate SnRK2.8, and the black arrowheads indicate the M1−M4 proteins. Molecular mass is given on the left-hand side in kDa.

(**C**) Quantification of M1 phosphorylation. The intensities of bands were quantified by densitometry of images using the Labwork image acquisition and analysis program (Media Cybernetics). The ratios of the phosphorylated band intensity relative to the protein bands stained by Coomassie Blue R250 were calculated. Three blots were measured and averaged. Error bars indicate S.E.M. (Student's *t* test, $*P<0.05$).

a MYC-encoding sequence was fused in-frame to the 5'-end of the *NTL6* gene, resulting in 35S:*NTL6* X *snrk2.8-1* plants. I also produced transgenic plants overexpressing the *MYC⁻M1* gene fusion (35S:*M1*), in which a MYC-encoding sequence was fused to the 5'-end of the full-size *NTL6* gene harboring a mutation at Thr^{142}. NTL6 proteins were immunologically detected using an anti-MYC antibody in the protein extracts prepared from the 35S:*NTL6* X *snrk2.8-1* and 35S:*M1* plants. Unexpectedly, no visible changes in NTL6 band patterns were observed in the protein samples extracted from the 35S:*M1* and 35S:*NTL6* X *snrk2.8-1* transgenic plants in comparison with those extracted from the 35S:*NTL6* transgenic plant (Figure 11). It is suspected that single residue phosphorylation by SnRK2.8 marginally affects the migration rate of phosphorylated NTL6 proteins. Similar results have been reported with several phosphorylated proteins (Grässer and König, 1992; Mok *et al.*, 2010).

I employed 2-DE to separate unphosphorylated and phosphorylated NTL6 forms. Total proteins were extracted from the 35S:*NTL6*, 35S:*M1* and 35S:*NTL6* X *snrk2.8-1* transgenic plants and subject to 2-DE. NTL6 proteins were immunologically detected using an anti-MYC antibody. In this assay system, NTL6 proteins having a molecular mass of 72 kDa were detected, but smaller NTL6 forms were not. This may be due to the protein instability of smaller processed forms (Seo *et al.*, 2010). Interestingly, whereas phosphorylated NTL6 forms were predominant in the protein samples extracted from the 35S:*NTL6* transgenic plants, unphosphorylated NTL6 forms were detected to a high level in the protein samples extracted from the 35S:*M1* and 35S:*NTL6* X *snrk2.8-1* transgenic plants (Figure 12), indicating that SnRK2.8-mediated NTL6 phosphorylation occurs *in vivo*.

It has been known that SnRK2.8 kinase is activated by osmotic stress (Umezawa *et al.*, 2004). I therefore investigated whether NTL6 phosphorylation by SnRK2.8 is influenced under osmotic stress conditions by

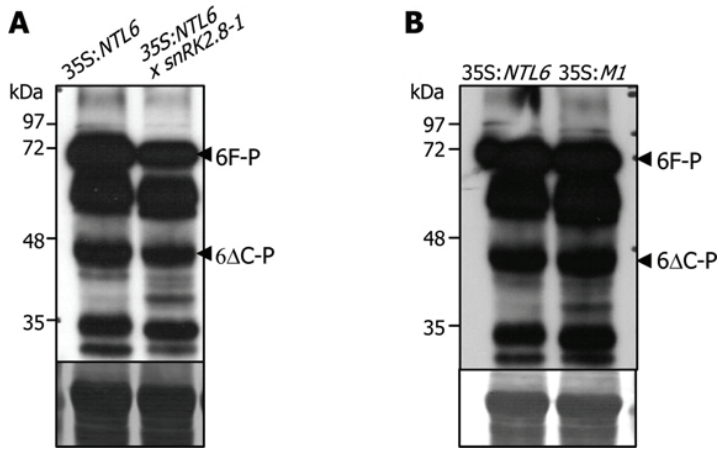

Figure 11. NTL6 phosphorylation in wild-type and *snrk2.8-1* mutant plants

Total proteins extracted from 2-week-old plants were analysed by immunoblot assays using an anti-MYC antibody.

(**A**) Immunoblot assays of protein extracts prepared from 35S:*NTL6* X *snrk2.8-1* plants.

(**B**) Immunoblot assays of protein extracts prepared from 35S:*M1* transgenic plants. Molecular mass is shown on the left-hand side in kDa.

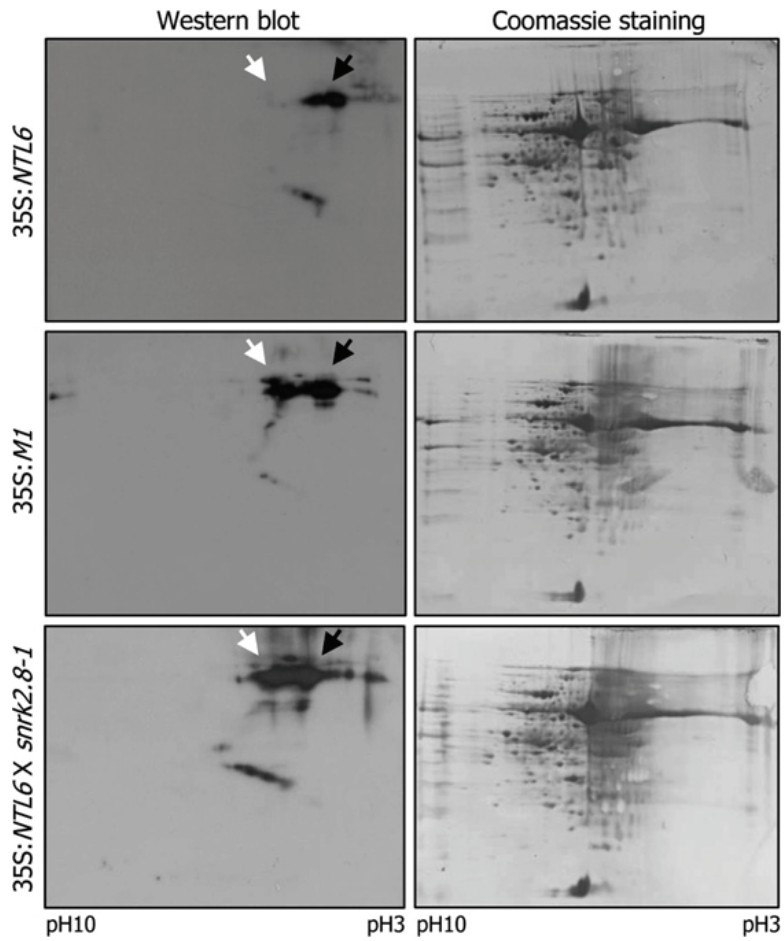

Figure 12. 2-DE of total proteins extracted from 35S:*NTL6*, 35S:*M1* and 35S:*NTL6* X *snrk2.8-1* transgenic plants

Whole plants (2-week-old) grown on MS agar plates were used for preparation of total protein extracts, which were analysed by 2-DE. The NTL6 proteins were detected by Western blot analysis using an anti-MYC antibody (left-hand panels), after which the membranes were stained with Coomassie Blue R250 (right-hand panels). The white arrows indicate NTL6 proteins that lack SnRK2.8-mediated phosphorylation. The black arrows indicate phosphorylated NTL6.

in-gel kinase assays (Fugii *et al.*, 2007). The assays using a recombinant MBP-6ΔC1 fusion protein as substrate revealed that SnRK2.8 kinase activity, and thus also NTL6 phosphorylation, was elevated under osmotic stress conditions (Figure 13). However, the elevation of NTL6 phosphorylation was not observed in the *snrk2.8-1* mutant, further supporting the phosphorylation of NTL6 by SnRK2.8.

SnRK2.6, SnRK2.7 and SnRK2.8 kinase proteins share a sequence identity of higher than 70%, and several residues, including Ser^{154} and Thr^{158}, are absolutely conserved (Umezawa *et al.*, 2004; Yoshida *et al.*, 2006), suggesting that they are important for kinase activity and autophosphorylation. The Ser^{154} and Thr^{158} residues of SnRK2.8 were mutated to alanine, resulting in mSnRK2.8. As inferred from the sequence analysis, *in vitro* phosphorylation assays using MBP-6ΔC protein as substrate revealed that both kinase activity and autophosphorylation was drastically reduced in the mSnRK2.8 protein (Figure 14).

Thr^{142} phosphorylation is important for nuclear import

To examine whether protein phosphorylation influences the subcellular localization of NTL6, a GFP-encoding sequence was fused in-frame to the 5'-ends of the *NTL6* and *NTL6-M1* genes, and the gene fusions were expressed transiently in *Arabidopsis* protoplasts. GFP signals were only present in the cytoplasm (Figure 15). When the GFP-NTL6 fusion was assayed, a large portion of GFP signals was detected in association with the plasma membranes (Figure 16A). GFP signals were also detected to a considerable level in the nucleus, which is certainly due to intrinsic NTL6 processing occurring in *Arabidopsis* protoplasts (Seo *et al.*, 2010) (Figure 17). When the GFP-NTL6-M1 fusion protein was assayed, the subcellular distribution of GFP signals was significantly altered: GFP signals were detected in a granular pattern in the cytoplasm and in association with the

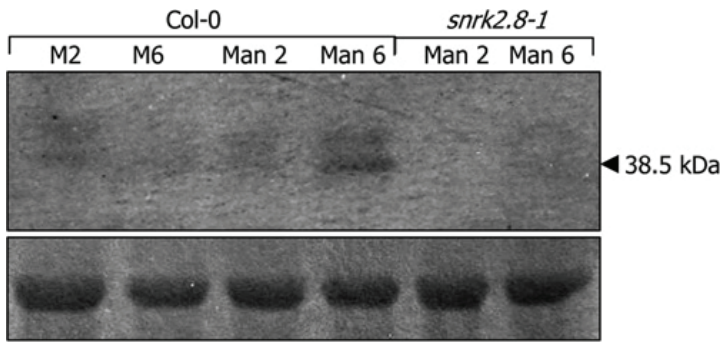

Figure 13. In-gel kinase assays

Plants grown for 2 weeks on MS agar plates under long days were transferred into MS liquid cultures supplemented with 150 mM mannitol and incubated for 2 (Man 2) or 6 (Man 6) h. Total proteins containing SnRK2.8 were extracted from whole plants and used in the assays. Recombinant MBP-6CΔ1 fusion proteins were used as substrate. The arrowhead indicates SnRK2.8 kinase.

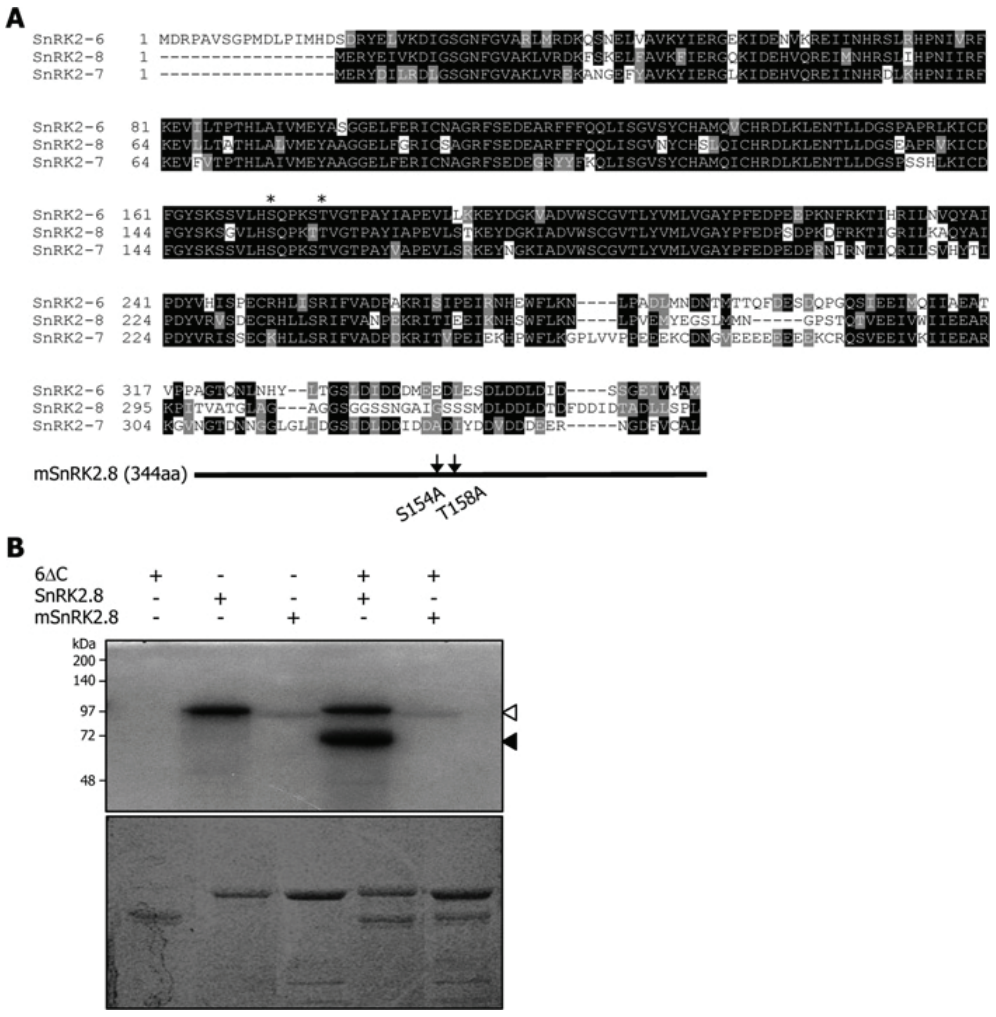

Figure 14. Generation of mutated SnRK2.8 and kinase activity assays

(**A**) Generation of mSnRK2.8. Amino acid residues that are critical for the SnRK2.8 kinase activity, such as Ser^{154} and Thr^{158} (marked by an asterisk), were mutated to alanine resulting in mSnRK2.8.

(**B**) *In vitro* phosphorylation assays. The 6ΔC protein was used as a substrate. The white arrowhead indicates the SnRK2.8 or mSnRK2.8 protein, and the black arrowhead indicates the 6ΔC protein. The recombinant proteins were prepared as MBP fusions in *E. coli* cells.

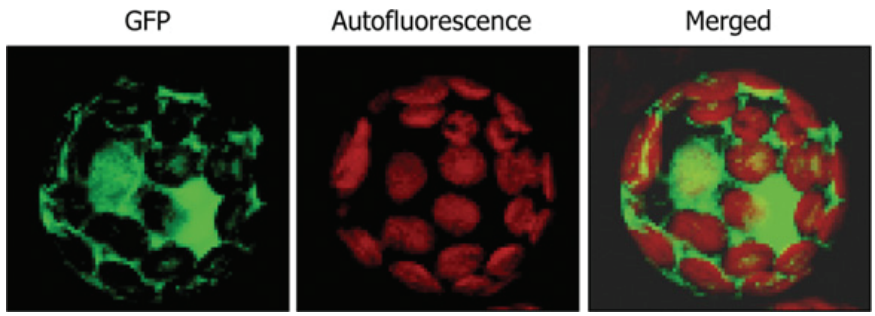

Figure 15. Expression of GFP alone in *Arabidopsis* protoplasts

The GFP-encoding gene was expressed transiently in *Arabidopsis* protoplasts and visualized by fluorescence microscopy. Chloroplasts appear red because of autofluorescence.

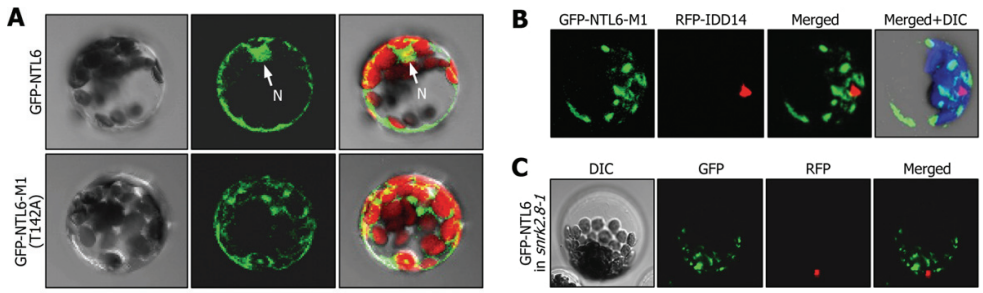

Figure 16. Nuclear localization of NTL6 proteins

(**A**) Subcellular localization of the NTL6 proteins. The *GFP-NTL6* and *GFP-NTL6-M1* gene fusions were transiently expressed in *Arabidopsis* protoplasts and visualized by DIC (left-hand panels) and fluorescence microscopy (middle panels). Chloroplasts appeared red because of autofluorescence. N, nucleus. See also Supplementary **Figure 17**.

(**B**) Exclusion of the NTL6-M1 protein from the nucleus. An RFP-encoding sequence was fused in-frame to the 5'-end of the *IDD14* transcription factor gene, and the *RFP-IDD14* gene fusion was assayed as described in (**A**). Chloroplasts appeared blue because of autofluorescence.

(**C**) Subcellular localization of the NTL6 proteins in the *snrk2.8-1* mutant. The *GFP-NTL6* gene fusion was transiently expressed in *Arabidopsis* protoplasts isolated from the *snrk2.8-1* mutant. Protoplasts were visualized by DIC and fluorescence microscopy. The *RFP-IDD14* gene fusion was included as a marker for nuclear localization.

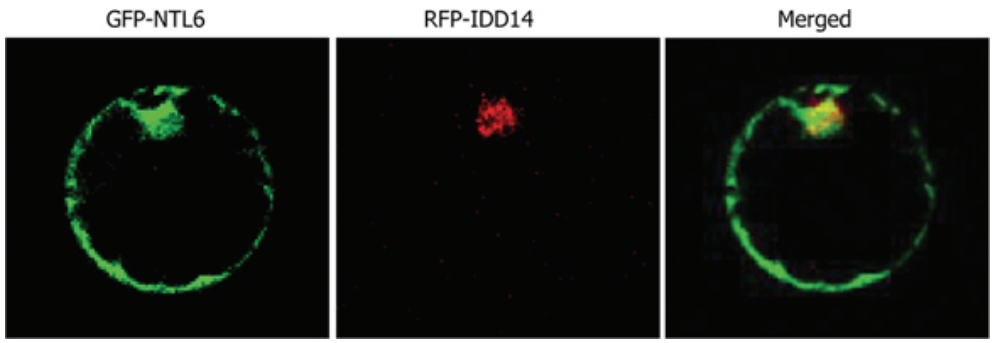

Figure 17. Co-expression of GFP-NTL6 and RFP-IDD14 in *Arabidopsis* protoplasts

The GFP-NTL6 construct was transiently co-expressed with an RFP-tagged IDD14 nuclear marker in *Arabidopsis* protoplasts and visualized by DIC microscopy.

plasma membranes, but were excluded from the nucleus (Figures 16A and 16B). The granular pattern of GFP signals was also observed when the GFP-NTL6 fusion protein was expressed in protoplasts prepared from the *snrk2.8-1* mutant (Figure 16C). Meanwhile, protein stability of the mutant NTL6 forms was unaffected in the *Arabidopsis* protoplasts (Figure 18). In support of this, the GFP signals were strongly detected in the nucleus when the *GFP-6ΔC* construct was expressed in the protoplasts prepared from the Col-0 strain, whereas GFP-6ΔC fusion proteins were not transported properly into the nucleus in the protoplasts isolated from the *snrk2.8-1* mutant (Figure 19). These observations indicate that SnRK2.8-mediated phosphorylation is required for nuclear import of the NTL6 protein.

I next carried out transcriptional activation activity assays in *Arabidopsis* protoplasts using a GAL4 transient expression system (Miura *et al.*, 2007). Since it was highly probable that both full-size NTL6 and 6ΔC are phosphorylated by SnRK2.8 (Figures 6C and 12), I carried out subsequent analyses using full-size NTL6 constructs. The *NTL6* and *NTL6-M1* gene sequences were fused in-frame to the 3'-end of the GAL4 DNA-binding domain-coding sequence in the effector plasmid (Figure 20A). The reporter plasmids contained *GUS* under the control of the CaMV 35S minimal promoter (pMin35S) or the NAC-binding sequence (NACBS; CAGTCTTGCGTGTTGGAACACGCATGTAGT), which has been proven to bind to the NAC domains (Olsen *et al.*, 2005), fused to the CaMV 35S minimal promoter (pNAC-BS). The effector plasmid, the reporter plasmid, and the plasmid containing the *Renilla* luciferase gene (Miura *et al.*, 2007), which is used to normalize activity measurements, were co-transformed into *Arabidopsis* protoplasts. The assays revealed that expression of the *NTL6* gene increased the GUS activity approximately 5-fold (Figure 20B), indicating that NTL6 is a transcriptional activator. In contrast, the transcriptional activation activity of the NTL6-M1 protein was reduced by

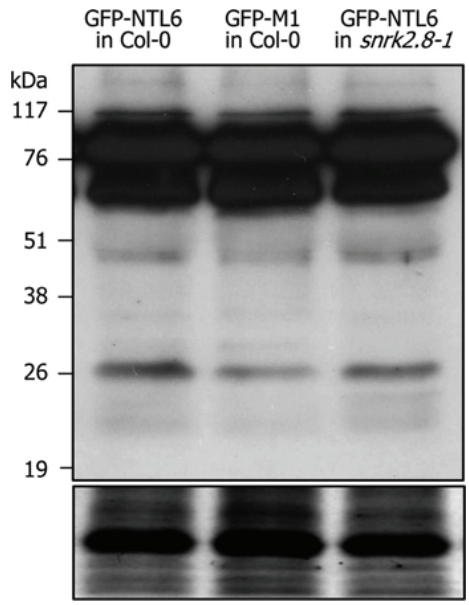

Figure 18. Protein stability of GFP−NTL6−M1 in *Arabidopsis* protoplasts

Total proteins were extracted from wild-type (Col-0) protoplasts expressing either the GFP-NTL6 or GFP-NTL6-M1 fusion and from *snrk2.8-1* mutant protoplasts expressing the GFP−NTL6 fusion. The NTL6 proteins were detected by Western blot analysis using an anti-GFP antibody. Part of a Coomassie Blue-stained gel is shown at the bottom. Molecular mass is shown on the left-hand side in kDa.

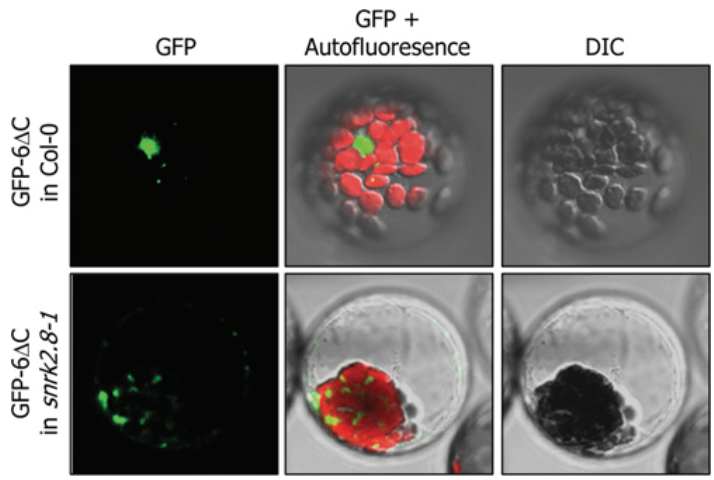

Figure 19. Subcellular localization of 6ΔC in the *snrk2.8-1* mutant

The *GFP-6ΔC* gene fusion was transiently expressed in *Arabidopsis* protoplasts isolated either from Col-0 plant or the *snrk2.8-1* mutant. Protoplasts were visualized by DIC and fluorescence microscopy.

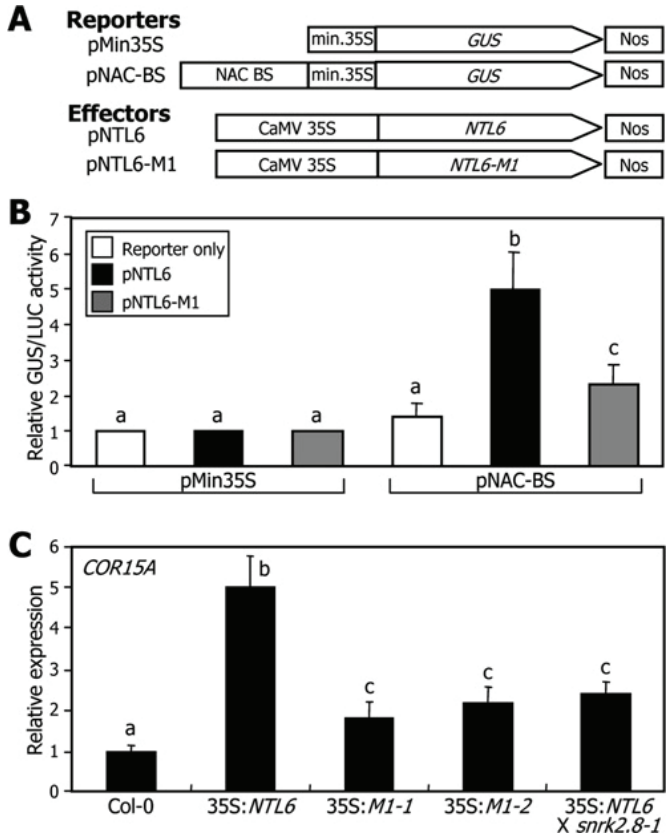

Figure 20. Transcriptional activation activity assays of NTL6 proteins

(**A**) Reporter and effector vectors used. The pMin35S reporter plasmid contains a minimal CaMV 35S promoter (a -56 to -8 sequence region including the TATA box) and GUS. The pNAC-BS reporter plasmid includes a putative NAC binding sequence (NAC BS) upstream of the minimal CaMV 35S (min.35S) promoter.

(**B**) Effects of M1 (T142A) mutation on the NTL6 transcriptional activation activity. The reporter and effector plasmids were co-transformed into *Arabidopsis* protoplasts. The GUS activities were measured by a fluorimetric method. A CaMV 35S promoter-LUC construct was also co-transformed as an internal control. Three measurements were averaged and statistically treated using one-way ANOVA with Fisher's post-hoc test (P<0.01). Error

bars indicate S.E.M.

(**C**) *COR15A* expression in transgenic plants expressing NTL6 proteins. Whole plants (2-week-old) grown on MS-agar plates were used for total RNA extraction. Transcript levels were determined by qRT-PCR. Biological triplicates samples were averaged. Error bars indicate S.E.M. ($P<0.01$, one-way ANOVA with Fisher's post-hoc test). Statistically significant differences between columns are shown by different letters.

more than 60%. Accordingly, expression of the *COR15A* gene was significantly reduced in the 35S:*M1* transgenic and 35S:*NTL6* X *snrk2.8-1* plants (Figure 20C). The reduced transcriptional activation activity of the NTL6−M1 protein may be because the mutant form is excluded from the nucleus. Alternatively, protein phosphorylation may be required for the interaction of NTL6 protein with a co-factor.

SnRK2.8 phosphorylation of NTL6 contributes to drought resistance

NTL6 and SnRK2.8 play a role in the drought-stress response (Umezawa *et al.*, 2004; Mizoguchi *et al.*, 2010). SnRK2.8 phosphorylates NTL6 and thus regulates its nuclear import. To determine the physiological relevance of NTL6 phosphorylation by SnRK2.8, I examined the drought stress response of the 35S:*NTL6* X *snrk2.8-1* plants. I found that the drought-resistant phenotype of 35S:*NTL6* transgenic plants was compromised in the 35S:*NTL6* X *snrk2.8-1* plants (Figure 21A). The 35S:*M1* transgenic plants were also more susceptible to drought stress than the 35S:*NTL6* transgenic plants. Water loss assays using detached leaves also showed similar results. The rate of water loss of the 35S:*NTL6* leaves was lower than those of the Col-0 leaves, 35S:*M1* transgenic leaves, and 35S:*NTL6* X *snrk2.8-1* leaves (Figure 22).

Together with previous reports (Kim *et al.*, 2007; Seo *et al.*, 2010; Seo and Park, 2010), the data indicate that upon exposure to water-deficit conditions, the NTL6 protein is activated through proteolytic cleavage. The processed NTL6 protein is phosphorylated by cytoplasmic SnRK2.8 and enters the nucleus (Figure 21B). Notably, SnRK2.8 does not influence the NTL6 processing step (Figure 23), showing that NTL6 phosphorylation and proteolytic cleavage are mutually independent processes.

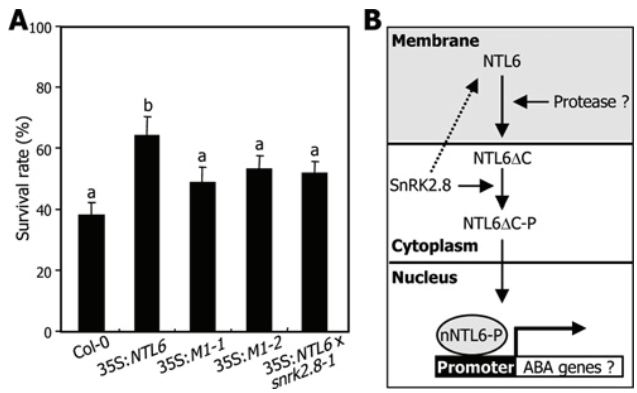

Figure 21. NTL6 phosphorylation by SnRK2.8 in the drought-resistance response

(**A**) Drought-resistance assays of 35S:*M1* transgenic and 35S:*NTL6* X *snrk2.8-1* plants. A total of three independent measurements of survival rates, each consisting of 30 seedlings, were averaged for each group. Error bars are S.E.M. (P<0.01, one-way ANOVA with Fisher's post-hoc test).

(**B**) Working model of SnRK2.8-mediated NTL6 phosphorylation. Under drought conditions, the membrane-bound NTL6 protein is activated through proteolytic cleavage, releasing the nuclear NTL6 form. The cytoplasmic SnRK2.8 mainly phosphorylates NTL6ΔC (NTL6ΔC-P). The phosphorylated nuclear NTL6 form enters the nucleus, where it regulates genes involved in drought-resistance response. Statistically significant differences between columns are shown by different letters.

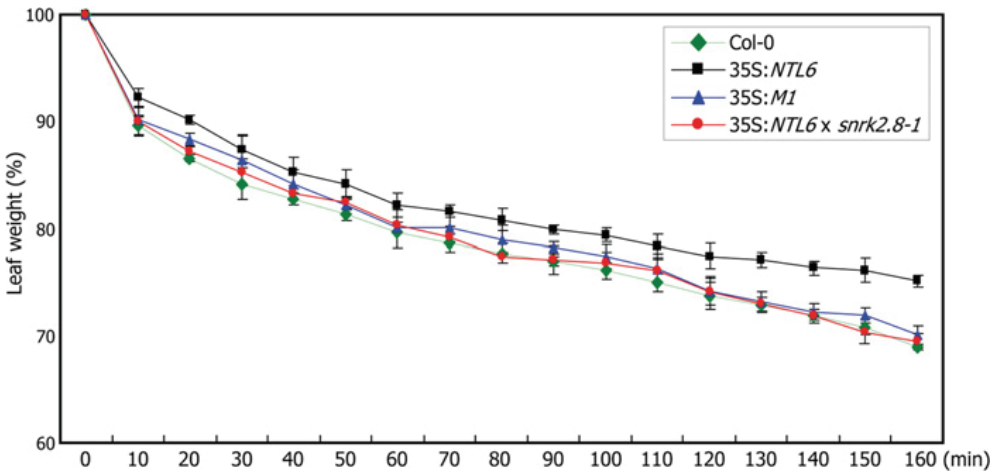

Figure 22. Water loss assays

The 4th-7th leaves of 4-week-old plants were detached and put on 3MM paper at room temperature for the indicated time periods. Three measurements were made and averaged for each plant genotype. Error bars indicate S.E.M..

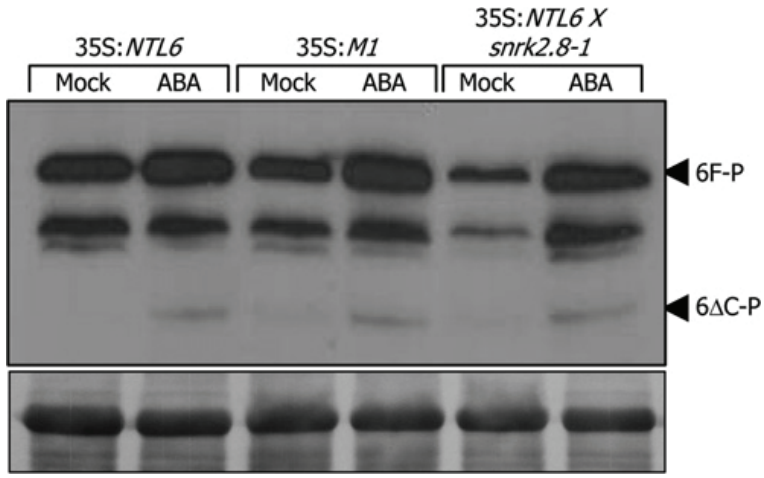

Figure 23. Effects of protein phosphorylation on NTL6 processing

A MYC-encoding sequence was fused in-frame to the 5'-end of the *NTL6-M1* gene sequence, and the fusion construct was expressed under the control of the CaMV 35S promoter in Col-0 plants, resulting in 35S:*M1* transgenic plants, similar to the generation of 35S:*NTL6* transgenic plants. The 35S:*NTL6* transgenic plants were crossed with the *snrk2.8-1* mutant, resulting in 35S:*NTL6* X *snrk2.8-1* plants. Two-week-old whole plants grown on MS agar plates were used for subsequent 20 μM ABA treatment. The NTL6 proteins were detected by Western blot analysis using an anti-MYC antibody.

DISCUSSION

Reversible phosphorylation of transcription factors has been evolved as a ubiquitous on/off switch in a wide array of cellular activities and signal transduction networks in eukaryotic cells (Halford and Hey, 2009). Phosphorylation of transcription factors has a profound effect on protein stability, nucleocytoplasmic translocation and DNA-binding activity (Kim *et al*., 2005; Vert and Chory, 2006; Ryu *et al*., 2007). In particular, it is well known that nuclear import of numerous transcription factors is regulated by protein phosphorylation in both animals and plants (Nardozzi *et al*., 2010). In plants, the best characterized are the BRI1 EMSSUPPRESSOR 1 (BES1) and BRASSINAZOLE RESISTANT 1 (BZR1) transcription factors functioning in brassinosteroid (BR) signal transduction (Vert and Chory, 2006; Ryu *et al*., 2007). Phosphorylation-mediated nucleocytoplasmic shuttling of the BES1 and BZR1 proteins constitutes a critical component of BR signalling.

The transcription factors that function in ABA-mediated stress signal transduction are also regulated by reversible phosphorylation, in which SnRKs may play a role (Yoshida *et al*., 2006; Fujii *et al*., 2007; Xu *et al*., 2009). A small group of SnRK2s is an important constituent of ABA receptors consisting of PYR1-like protein (PYR/PYL)/regulatory components of ABA receptor (RCAR) and PP2C. The PP2C protein phosphatases dephosphorylate SnRK2s in the absence of ABA. In the presence of ABA, the ABA-binding PYR protein inactivates the PP2C enzymes, resulting in rapid liberation of SnRK2s. Consistently, SnRK2s play a role in plant responses to osmotic stress (Umezawa *et al*., 2004). For example, the SnRK2.8 activity is moderately enhanced by ABA (Boudsocq *et al*., 2004). In addition, the promotion of the SnRK2.8 activity initiates within 2 min and reaches a maximum level 2 h after the application of high salt.

Subsequently, SnRK2.8 presumably regulates a large part of stress-responsive gene expression by reversibly phosphorylating the nuclear bZIP transcription factors AREBs/ABFs, as has been shown with other SnRK2s (Mizoguchi *et al*., 2010; Yoshida *et al*., 2010), suggesting that SnRK2.8-mediated protein phosphorylation is an early event in the osmotic stress signalling cascade (Umezawa *et al*., 2004).

It is largely unknown how environmental signals perceived at the plasma membranes are transmitted to the nucleus. Controlled proteolytic activation of the plasma membrane-bound NTL6 transcription factor would be a molecular event that transmits the signals from the plasma membranes to the nucleus. The plasma membrane-anchored NTL6 protein is rapidly processed and translocated into the nucleus after ABA and cold treatments (Kim *et al*., 2007; Seo *et al*., 2010). However, it has been unexplored whether membrane release is sufficient for nuclear import of NTL6. In the present study, I identified SnRK2.8 as a component of NTL6-mediated drought-stress signalling. SnRK2.8-mediated phosphorylation is required for nuclear import of NTL6. It is noteworthy that SnRK2.8 is linked with NTL6 signalling, showing that protein phosphorylation fine-tunes NTL6 activity in concert with proteolytic activation process.

Previous observations (Seo *et al*., 2010) and the results of the present study demonstrate that NTL6 activity is regulated at multiple steps, including transcriptional control, protein processing and nuclear translocation. These data indicate that SnRK2.8 phosphorylates both full-size (Figure 12) and processed (Figure 6C and 12) NTL6 proteins. Nevertheless, I assume that SnRK2.8 is mainly involved in processed NTL6 phosphorylation, based on the following observations. First, the 35S:*6ΔC* transgenic plants showed drought-resistant phenotypes (Figures 2A-2C). Secondly, GFP-6ΔC is clearly translocated into the nucleus, but its nuclear import is disrupted when *SnRK2.8* is non-functional (Figure 19). Thirdly, interactions of NTL6 with

SnRK2.8 are predominantly observed in the cytoplasm (Figure 6B). The phosphorylation of full-size NTL6 may take place under non-stress conditions, because of their intrinsic interactions. Notably, whereas phosphorylation status of NTL6 is important for its nuclear import, it does not affect the processing step. I propose that phosphorylation of NTL6 by SnRK2.8 would be a molecular link that incorporates various environmental cues, such as osmotic- and drought-stress signals, into gene regulatory networks that regulate plant stress responses.

The results of the present study support that the SnRK2.8 phosphorylation of NTL6 at Thr^{142} is critical for nuclear import and the physiological role of NTL6 in inducing a drought resistance response. I observed that site-directed mutation of the Thr^{142} residue considerably inhibits phosphorylation and nuclear import, resulting in reduced drought resistance in transgenic plants overexpressing the mutated *NTL6* gene (*M1*). It could be argued that the mutation-induced structural perturbation(s) could cause indirect effects on NTL6 phosphorylation. I showed that NTL6 stability and processing, which is closely associated with protein conformation (Seo *et al*., 2008; Kim *et al*., 2010; Srivastava *et al*., 2012), is uninfluenced in the 35S:*M1* transgenic plants (Figures 18 and 23), supporting that the NTL6 mutation does not influence protein conformation. NTL6 protein is highly unstable both in planta and in recombinant expression systems, such as *E. coli* cells (Seo *et al*., 2010), and thus it is practically difficult to obtain sufficient amount of the NTL6 protein for structural analysis. The following approach would be mass spectrometric analysis [MS/MS (tandem MS)] and/or co-immunoprecipitation assays using modification-specific antibodies raised against phosphorylated NTL6 proteins, if conditions for NTL6 purification and processing are improved in the future.

It is also currently unclear whether SnRK2.8 is the sole kinase that phosphorylates NTL6. NTL6 phosphorylation was not completely diminished

in the *snrk2.8-1* mutant (Figure 12). In addition, the high expression of *COR15A* and drought resistance in the 35S:*NTL6* transgenic plants were not fully compromised in the 35S:*M1* transgenic and 35S:*NTL6* X *snrk2.8-1* plants (Figures 20C and 21A). There are multiple putative phosphorylation sites in the NTL6 protein, suggesting that multiple kinases would be involved in NTL6 phosphorylation. It is therefore probable that other kinases may also phosphorylate the NTL6 protein to regulate its transcriptional activity, proteolytic cleavage or nuclear import.

SnRK2.8 phosphorylates NTL6. However, it does not phosphorylate other NAC transcription factors, including NTM1, NTL8 and NTL9. The other NAC transcription factors have protein structural organizations similar to those of NTL6 and play a role in various abiotic stress responses, such as salt and osmotic stress (Kim *et al*., 2007; Yoon *et al*., 2008). It is currently unclear whether protein phosphorylation is also important for the activities of other NAC MTFs. It is worth examining whether they are phosphorylated by other SnRK2 kinase(s) and whether different NAC MTFs are phosphorylated by different SnRK2s. A few bZIP transcription factors, such as bZIP17, bZIP28 and bZIP60, are also membrane-associated and involved in the endoplasmic reticulum stress response (Iwata and Koizumi, 2005; Liu *et al*., 2007a; Liu *et al*., 2007b). It will be interesting to see whether the co-ordinate regulation of NTL6 by protein phosphorylation and proteolytic processing is also relevant to the bZIP MTFs.

It is largely unknown how protein phosphorylation modulates nuclear import of transcription factors. Protein phosphorylation may increase the binding affinity of transcription factors for specific import factors or enhance the docking of the cargos to nuclear pore complexes (Nardozzi *et al*., 2010). Alternatively, it can modulate the recognition process of transcription factors by importin and activate non-canonical transport signals that mediate their nuclear import. Accordingly, NTL6 would be a potential

target for studies on the machinery and mechanisms involved in the transportation process of transcription factors into the nucleus.

CHAPTER 2

A Golgi-localized MATE transporter mediates iron homeostasis under osmotic stress in *Arabidopsis*

ABSTRACT

Iron is an essential micronutrient that acts as a cofactor in a wide variety of pivotal metabolic processes, such as the electron transport chain of respiration, photosynthesis and redox reactions, in plants. However, its overload exceeding the cellular capacity of iron binding and storage is potentially toxic to plant cells by causing oxidative stress and cell death. Consequently, plants have developed versatile mechanisms to maintain iron homeostasis. Organismal iron content is tightly regulated at the steps of uptake, translocation and compartmentalization. Whereas iron uptake is fairly well understood at the cellular and organismal levels, intracellular and intercellular transport is only poorly understood. In the present study, I show that a MATE (multidrug and toxic compound extrusion) transporter, designated BCD1 (BUSH-AND-CHLOROTIC-DWARF 1), contributes to iron homeostasis during stress responses and senescence in *Arabidopsis*. The *BCD1* gene is induced by excessive iron, but repressed by iron deficiency. It is also induced by cellular and tissue damage occurring under osmotic stress. The activation tagged mutant *bcd1-1D* exhibits leaf chlorosis, a typical symptom of iron deficiency. The chlorotic lesion of the mutant was partially recovered by iron feeding. Whereas the *bcd1-1D* mutant accumulated a lower amount of iron, the iron level was elevated in the knockout mutant *bcd1-1*. The BCD1 protein is localized to the Golgi complex. I propose that the BCD1 transporter plays a role in sustaining iron homeostasis by reallocating excess iron released from stress-induced cellular damage.

INTRODUCTION

In plants, the content of endogenous iron should be tightly regulated to supply sufficient amounts of this micronutrient while avoiding excess accumulation for optimal growth. Iron is an essential element for plant growth and development. It is required for various metabolic processes, such as chlorophyll biosynthesis, photosynthesis, respiration and redox reactions (Curie and Briat, 2003; Briat *et al.,* 2007). Therefore, deficiency of iron leads to diverse developmental defects, including chlorosis, growth retardation and reduced crop productivity (Briat *et al.*, 2007).

Although iron is one of the most abundant elements on earth (Staiger, 2002), it forms insoluble ferric iron [Fe(III)] in an aerobic environment at neutral or basic pH (Guerinot and Yi, 1994). Therefore, solubilization and uptake of iron from the soil is critical, and plants have evolved versatile biochemical mechanisms to deal with this difficulty. Dicots and non-graminaceous plants have developed an iron-uptake mechanism known as 'Strategy I'. In this strategy, plasma membrane-localized H^+-ATPases release protons from the roots to acidify the rhizosphere, resulting in an increase in iron solubility. The ferric chelate reductase FERRIC REDUCTASE OXIDASE 2 (FRO2) reduces Fe(III) to the soluble Fe(II) form (Robinson *et al.*, 1999). An iron transporter IRON-REGULATED TRANSPORTER 1 (IRT1), which belongs to the zinc-regulated transporter (ZRT)/IRT-like protein (ZIP) family, transports Fe(II) into root epidermal cells (Eide *et al.*,, 1996; Varotto *et al.*, 2002; Vert *et al.*, 2002). Expression of the *FRO2* and *IRT1* genes is transcriptionally regulated by a small set of bHLH (basic helix−loop−helix) transcription factors, Fe-REGULATED-LIKE IRON DEFICIENCY-INDUCED TRANSCRIPTION FACTOR (FIT), bHLH38 and bHLH39 (Colangelo and Guerinot, 2004; Jakoby *et al.*, 2004; Yuan *et al.*, 2005; Bauer *et al.*, 2007; Yuan *et al.*, 2008).

Grasses have employed a distinct mechanism, termed 'Strategy II', for iron uptake. These plant species release Fe(III)-specific chelators, called siderophores (Curie and Briat, 2003). The solubilized Fe(III)−siderophore complexes are transported through a specific transport system in the root plasma membranes. The maize YELLOW STRIPE 1 (YS1) protein, a member of the OLIGOPEPTIDE TRANSPORTER (OPT) family, has been identified as the transporter that mediates the uptake of the iron−siderophore complexes in response to iron deficiency (Curie *et al.*, 2001; Mori, 1999).

However, excess accumulation of iron is potentially toxic to plant cells by catalyzing the generation of reactive oxygen species (ROS) via the Fenton reaction (Staiger, 2002). Therefore proper maintenance of iron storage and distribution, which is achieved primarily by compartmentalization and translocation into specific cellular organelles and plant organs respectively (Curie and Briat, 2003; Hall and Williams, 2003; Jeong and Guerinot, 2009), is necessary for plant growth and survival. Vacuoles are an important cellular organelle for iron storage and sequestration (Lanquar *et al.*, 2005; Kim *et al.*, 2006). The VACUOLAR IRON TRANSPORTER 1 (VIT1) protein transports cellular iron into the vacuoles (Kim *et al.*, 2006). In contrast, two members of the NATURAL RESISTANCE-ASSOCIATED MACROPHAGE PROTEIN (NRAMP) family, NRAMP3 and NRAMP4, export iron from the vacuoles (Lanquar *et al.*, 2005), supporting the central role of vacuoles in iron homeostasis in plant cells. Chloroplasts and mitochondria are two major organelles that contain large amounts of iron (Jeong and Guerinot, 2009). For example, the chloroplasts contain approximately 80% of total cellular iron in a typical leaf cell (Shikanai *et al.*, 2003). Ferritins (FERs) act as iron-storage proteins in the organelles (Zancani *et al.*, 2004; Murgia *et al.*, 2007; Ravet *et al.*, 2009). Through the co-ordinated actions of the transporters and storage proteins, iron homeostasis is optimally maintained in plant cells.

Intercellular iron transporters also contribute to the maintenance of iron homeostasis and iron distribution. The plasma membrane-localized FERRIC REDUCTASE DEFECTIVE 3 (FRD3) protein, a member of the MULTIDRUG AND TOXIC COMPOUND EXTRUSION (MATE) family, facilitates the transport of Fe(III)-citrate from the roots to the shoots (Rogers and Guerinot, 2002; Grotz and Guerinot, 2006; Durrett *et al.*, 2007). Nicotianamine chelates both Fe(II) and Fe(III) and facilitates the intercellular transport through the phloem (Ling, *et al.*, 1999). Some members of the YELLOW STRIPE-LIKE (YSL) family have also been suggested to play a role in the intercellular transport of Fe(II)-nicotianamine complexes (Curie *et al.*, 2009; Klatte *et al.*, 2009). It has been reported that mutations in the *FRD3* or *YSL* genes induce chlorosis and hypersensitivity to iron deficiency (Ling *et al.*, 1999; Waters *et al.*, 2006; Klatte *et al.*, 2009), indicating that iron distribution between different plant organs is essential for maintaining iron homeostasis.

Iron homeostasis is influenced by endogenous and exogenous signalling cues. The *FER* genes are regulated transcriptionally by the senescence process and environmental stress conditions (Gaymard *et al.*, 1996; Tarantino *et al.*, 2003; Murgia *et al.*, 2007), showing that iron status is also dynamically fluctuated in response to developmental and environmental changes (Tarantino *et al.*, 2003; Murgia *et al.*, 2007).

The iron transporter systems, including the MATE transporters, have been studied extensively in recent years in several plant species. The MATE proteins are widely conserved in all living organisms. They are involved in the efflux of small organic molecules and excretion of toxic compounds and xenobiotics (Morita *et al.*, 1998; Morita *et al.*, 2000; Li *et al.*, 2002). The *Arabidopsis* genome encodes 58 MATE members (Hvorup *et al.*, 2003), and their biological functions have been studied in plant responses to diverse developmental and environmental stimuli. The MATE proteins characterized

so far are localized to either the vacuolar membranes or plasma membranes, and are involved in intercellular and intracellular transport of secondary metabolites and xenobiotics via the H^+ exchange mechanism (Omote *et al.*, 2006). Their physiological roles include protection of plant cells from inhibitory compounds (Diener *et al.*, 2001), anthocyanin accumulation (Debeaujon *et al.*, 2001; Marinova *et al.*, 2007; Zao and Dixon, 2009), salicylic acid (SA) signalling (Nawrath *et al.*, 2002), aluminum tolerance (Diener *et al.*, 2001; Magalhaes *et al.*, 2007; Liu *et al.*, 2009) and heavy metal detoxification (Li *et al.*, 2002; Omote *et al.*, 2006). In particular, they also play a role in maintaining iron homeostasis (Rogers and Guerinot, 2002; Durrett *et al.*, 2007), although the underlying regulatory mechanism remains to be elucidated.

In the present study, I found that a Golgi-localized MATE transporter BUSH-AND-CHLOROTIC-DWARF 1 (BCD1), which has previously been named as ZRIZI (ZRZ) and is involved in organ initiation (Burko *et al.*, 2011), also plays a role in maintaining iron homeostasis under osmotic stress. The *BCD1* gene is regulated by iron availability. It is also induced when cells are damaged by osmotic stress and senescence. The chlorotic leaves of the activation-tagged *bcd1-1D* mutant were rescued by iron feeding. These results support the hypothesis that the BCD1 MATE transporter contributes to the maintenance of iron homeostasis, possibly by secreting excess iron released from damaged leaf cells under adverse growth conditions.

MATERIALS AND METHODS

Plant materials and growth conditions

All *Arabidopsis thaliana* lines used were in the Columbia (Col-0) background. Plants were grown in a controlled culture room at 22°C with a relative humidity of 55% under long-day conditions (16 h light/8 h dark) with white light illumination (120 μmol of photons/m^2s) provided by fluorescent FLR40D/A tubes (Osram). The *bcd1-1* mutant (SALK-067667) was isolated from a T-DNA insertional mutant pool deposited into the ABRC (Arabidopsis Biological Resource Center, Ohio State University, Columbus, OH, U.S.A.). Homozygotic lines were obtained by herbicide selection for three or more generations and analysis of segregation ratios.

The *bcd1-1D* mutant was isolated from an activation-tagging mutant pool that was generated by transforming Col-0 plants with the activation-tagging vector pSKI015 (Weigel *et al.*, 2000). Collected T1 seeds were sown in soil, and a Finale solution (AgrEvo), which contains 5.78% Basta, was diluted 1000 times with deionized water and sprayed twice a week. Among the herbicide-resistant transformants, a morphogenic mutant (*bcd1-1D*) that showed dwarfed growth with reduced apical dominance and pale green leaves was chosen for analysis. Homozygotic T_3 mutant seeds that have a single T-DNA insertional event were used in further studies.

To produce transgenic plants overexpressing the *BCD1* gene, a full-size cDNA was subcloned into the binary pB2GW7 vector under the control of the CaMV (cauliflower mosaic virus) 35S promoter (Invitrogen). *Agrobacterium*-mediated *Arabidopsis* transformation was performed according to a modified floral dip method (Clough and Bent, 1998).

Treatments with growth hormones and abiotic stresses

Plants (2 weeks old) grown on 1/2× MS (Murashige and Skoog; Duchefa)

agar plates were transferred to MS liquid cultures supplemented with various growth hormones. Abscisic acid (ABA), indole-3-acetic acid (IAA), gibberellic acid (GA), 1-aminocyclopropane-1-carboxylic acid (ACC), paclobutrazol (PAC) and brassinolide (BL) were used at a final concentration of 20 μM. SA was used at a final concentration of 100 μM.

For the assays on the effects of drought on gene expression, 2-week-old plants grown on MS agar plates were placed on a dry 3MM paper (Whatman) at room temperature (23−25^{o}C) for the indicated time periods. To examine the effects of high salinity on gene expression, 2-week-old plants grown on MS agar plates were soaked in MS liquid cultures containing 150 mM NaCl and incubated under constant light for the indicated time periods. To examine the effects of osmotic stress on gene expression, 2-week-old plants were transferred to MS liquid cultures containing 150 mM mannitol or 150 mM sorbitol (Sigma) and incubated for the indicated time periods.

Analysis of transcript levels

Quantitative real-time reverse transcription (RT)−PCR (qRT-PCR) was employed to measure gene transcript levels. Preparation of total RNA samples and RT−PCR were carried out on the basis of the rules that have previously been proposed to ensure reproducible and accurate measurements of gene transcript levels (Udvardi *et al*., 2008). Extraction of total RNA samples from appropriate plant materials and RT−PCR conditions have been described previously (Yang *et al*., 2011). Total RNA samples pretreated extensively with an RNase-free DNase were used for RT by SuperScript II reverse transcriptase (Invitrogen) in a 20 μl reaction volume.

qRT−PCR was carried out in 96-well blocks with an Applied Biosystems 7500 Real-Time PCR System using the SYBR Green I master mix in a volume of 25 μl. A 1 μl volume (20−100 ng) of cDNA was used

as a template for individual qRT−PCR runs. The PCR primers were designed using the Applied Biosystems Primer Express® software and are listed in Table 3. The two-step thermal cycling profile used was 15 s at 94°C and 1 min at 68°C. An *EUKARYOTIC INITIATION FACTOR 4A* (*eIF4a*) gene (At3g13920) was included in the assays as an internal control for normalizing the variations in cDNA amounts used (Gutierrez *et al*., 2008). All of the qRT−PCRs were carried out in biological triplicates using total RNA samples extracted from three independent plant materials grown under identical conditions. The comparative $\Delta\Delta C_T$ method was used to evaluate the relative quantities of each amplified product in the samples. The threshold cycle (C_T) was automatically determined for each reaction by the system set with default parameters. The specificity of the PCRs was determined by melt curve analysis of the amplified products using the standard method installed in the system.

***Escherichia coli* complementation assays**

The *E. coli acrB* mutant strain was obtained from the NBRP (National BioResource Project, National Institute of Genetics, Mishima, Japan). This mutant is sensitive to many drugs, since the AcrAB system is non-functional. For complementation assays, the *Arabidopsis BCD1* gene was subcloned into the pET21c expression vector, and the construct was transformed into wild-type *E. coli* cells (BW25113) and the *acrB* mutant cells. Transformants were selected on LB (Luria−Bertani) agar plates containing 100 μg/ml ampicillin. The transformants were grown in LB liquid medium containing ampicillin and 1 mM isopropyl-β-D-thiogalactopyranoside (IPTG) for induction of *BCD1* gene expression. The cell cultures were diluted to a 10-fold gradient series and spotted on to LB-ampicillin plates containing different concentrations of tetrabutyl ammonium (TBA). Cell growth was also determined by measuring the attenuance at 600 nm of

liquid cultures grown at 37°C for 24 h.

Histological assays

The primers used for subcloning of the *BCD1* gene promoter were BCD1-GUS-F (5'-AAAAAGCAGGCTTTAGAATTGGTTAATTTGCGAT-3') and BCD1-GUS-R (5'-GAAAGCTGGGTGATTCTTAAGAGGAGTAAAC-3') (GUS is *β*-glucuronidase). The genomic PCR product was subcloned into the pHGWFS7 vector (Invitrogen), and the expression construct was transformed into Col-0 plants.

For histochemical analysis of GUS activities, appropriate plant materials were incubated in 90% acetone for 20 min on ice, washed twice with rinsing solution [50 mM sodium phosphate, pH 7.2, 0.5 mM $K_3Fe(CN)_6$ and 0.5 mM $K_4Fe(CN)_6$], and subsequently incubated at 37°C for 18−24 h in rinsing solution containing 2 mM 5-bromo-4-chloro-3-indolyl-β-D-glucuronide (X-Gluc, Duchefa). The plant samples were then incubated in a series of ethanol solutions ranging from 15% to 80% in order to remove chlorophylls from plant tissues. The plant samples were mounted on glass microscope slides and visualized using a Nikon SMZ 800 microscope (Nikon).

Measurements of chlorophyll content

Measurements of chlorophyll content were carried out as described previously (Oh *et al*., 1997). Chlorophylls were extracted with DMF (N,N-dimethylformamide), and the extracted solution was incubated at 4°C for 2 h in complete darkness. Chlorophyll contents were assayed by measuring the absorbance at 652 nm, 665 nm and 750 nm using a diode array spectrophotometer (WPA Biowave).

Iron treatments

Iron-sufficient media were standard half-strength MS media that were supplemented with 0.05% MES, 1% sucrose and 50 μM Fe-EDTA substituted for iron sulfate (Long *et al*., 2010). Agar (6%) was included to prepare agar medium plates. Iron-deficient media were prepared by including 300 μM ferrozine substituted for iron sulfate. For treatments with excessive iron, 400 μM $FeSO_4$ was added to fresh liquid medium, as described previously (Fukao *et al*., 2011). Ferric chelate reductase assays were performed as described previously (Yi and Guerinot, 1996).

Perls iron staining

Perls iron staining of plant materials was carried out to determine localization and intensity of Fe^{3+} in plant tissues, as described previously (Long *et al*., 2010). Briefly, 2-week-old *Arabidopsis* seedlings grown on iron-sufficient agar plates or detached leaves were thoroughly rinsed in deionized water before Perls iron staining. Equal amounts of 4% (v/v) HCl and 4% (w/v) potassium ferrocyanide were mixed immediately prior to use. Plant materials were then vacuum-infiltrated with the mixture for 30 min. The plant materials were subsequently incubated for 30 min in Perls staining solution. After rinsing three times with deionized water, they were observed using a Nikon SMZ 800 microscope.

Measurement of iron content

Approximately 300 plants grown on iron-sufficient agar plates for 3 weeks were washed for 10 min with washing solution (2 mM $CaSO_4$ and 10 mM EDTA) and rinsed for 10 min with deionized water. Iron contents were assayed at NICEM (National Instrumentation Center for Environmental Management, Seoul National University, Seoul, Korea) using a magnetic sector inductively coupled plasma mass spectrometer (ICP-MS; Varian

820-MS).

Subcellular localization assays

A red fluorescent protein (RFP)-coding sequence was fused in-frame to the 5'-end of the *BCD1* gene, and the gene fusion was subcloned into the p326-RFP vector (Choi, *et al*., 2005). The fusion construct was transformed into *Arabidopsis* protoplasts prepared from leaf mesophyll cells by a PEG-mediated transformation method (Yoo *et al*., 2007). The subcellular distribution of red fluorescence was visualized by differential interference contrast (DIC) microscopy and fluorescence microscopy.

Primer	Usage	Sequence (5′→3′)
BCD1-F	qRT–PCR	GATGGCCAAGTTTTCTGGAG
BCD1-R	qRT–PCR	GCATCGATATCATCGCTCTTG
SAG12-F	qRT–PCR	GCCGTATCCAATCGCAGTTA
SAG12-R	qRT–PCR	CTTCTATTACAGGTTATGAGGATGTC
IRT1-F	qRT–PCR	CATGGCACTCGTGGATCTTC
IRT1-R	qRT–PCR	CGATAATCGACATTCCACCG
FRO2-F	qRT–PCR	TCCACGTCGGCATAAGTTTC
FRO2-R	qRT–PCR	GGAAGGAAGAATCCGAGCAG
PYE-F	qRT–PCR	TCCCAGGACTTCCCATTTTC
PYE-R	qRT–PCR	GCGCTAGCATACCTTGGACA
VIT1-F	qRT–PCR	TTAACCGTTCCTTTTGCCCT
VIT1-R	qRT–PCR	AAGAAGAGATCGTGGCCGTT
PIC1-F	qRT–PCR	TGTGAAAGGTTTGAGGAGCG
PIC1-R	qRT–PCR	TCCTTGGTCTTGTTTGCTCG
eIF4a-F	qRT–PCR	TGACCACACAGTCTCTGCAA
eIF4a-R	qRT–PCR	ACCAGGGAGACTTGTTGGAC
BCD1-B1	Subcloning	AAAAAGCAGGCTTCATGTGTAATTCAAAACCATCTTCT
BCD1-B2	Subcloning	AGAAAGCTGGGTAAACCAACATGGTTCTCATCAT
BCD1–GUS-F	Subcloning	AAAAAGCAGGCTTTAGAATTGGTTAATTTGCGAT
BCD1–GUS-R	Subcloning	AGAAAGCTGGGTGATTCTTAAGAGGAGTAAAC

Table 3. Primers used in the study

F, forward primer; R, reverse primer.

RESULTS

bcd1-1D mutant exhibits stunted growth and leaf chlorosis

A morphogenic mutant, designated *bcd1-1D*, was isolated from screening of an *Arabidopsis* activation-tagged mutant pool generated by randomly integrating the CaMV 35S enhancer element into the genome of ecotype Col-0 (Figure 24A). *bcd1-1D* mutant exhibited stunted growth with reduced apical dominance and pale green leaves. The plant height of the *bcd1-1D* mutant was reduced approximately 2-fold in comparison with that of Col-0 plants (Figure 24B). The length of siliques was also significantly shorter in the mutant (Figure 24C). Notably, the mutant leaves were smaller and pale green (Figure 24D). It was found that the chlorophyll content was reduced by approximately 40% in the mutant (Figure 24E), suggesting that the pale green colour of the mutant leaves is caused by reduction in chlorophyll content.

Mapping the T-DNA insertional sites by a three-step thermal asymmetric interlaced (TAIL)-PCR (Liu *et al*., 1995) and gene expression analysis revealed that the *At1g58340* gene was activated by the nearby insertion of the 35S enhancer element in the *bcd1-1D* mutant (Figures 24F, 24G and 25). The tagged *At1g58340* gene has recently been named *ZRZ*/*ZF14* (Burko *et al*., 2011). However, I decided to designate it *BCD1* to depict more precisely the phenotypes of the *bcd1-1D* mutant. Transgenic plants overexpressing the *BCD1* gene under the control of the CaMV 35S promoter recapitulated the phenotypes of the *bcd1-1D* mutant (Figure 24A). At least seven independent transgenic lines were obtained from Col-0 transformation, all of which exhibited identical phenotypes. I therefore concluded that overexpression of the *BCD1* gene is the molecular cause of the *bcd1-1D* mutant phenotypes.

The T-DNA insertional knockout *bcd1-1* mutant did not show any

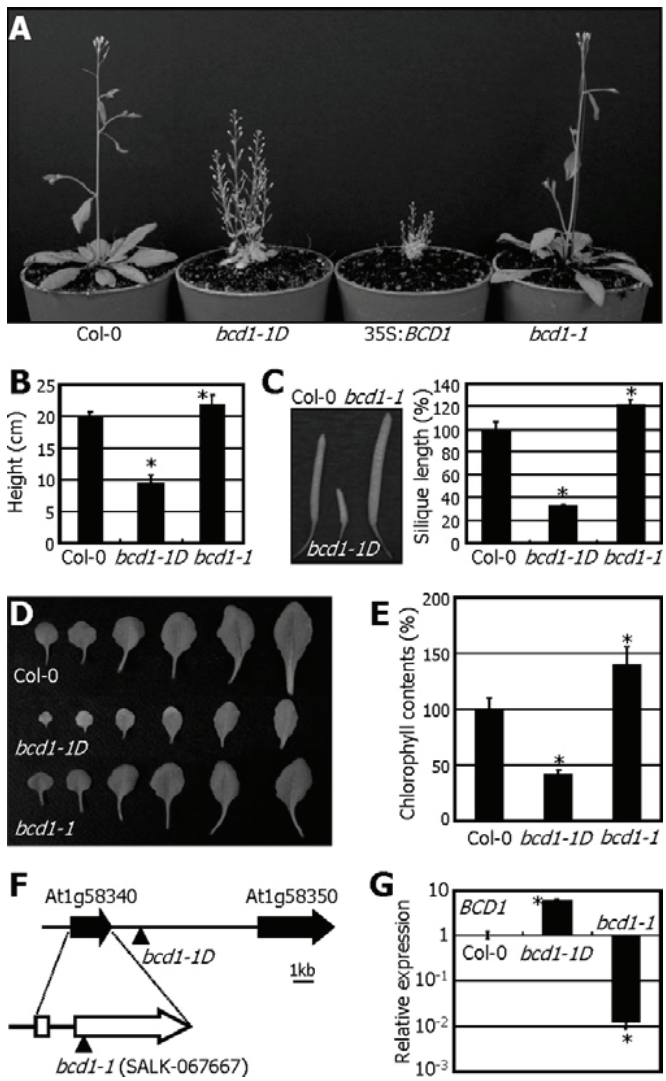

Figure 24. Reduced apical dominance and pale green leaves in the *bcd1-1D* mutant

(**A**) Phenotypes of *bcd1-1D* and *bcd1-1* mutants. Plants (5 weeks old) grown in soil were photographed. Transgenic plants overexpressing the *BCD1* gene under the control of the CaMV 35S promoter (35S:*BCD1*) were included for comparison.

(**B**) Plant heights. Plants were grown in soil for 5 weeks. Heights of 30

plants were measured for each plant genotype. Biological triplicates were averaged and statistically treated using a Student's *t* test (**P*<0.01). Error bars indicate S.E.M.

(**C**) Silique lengths. Siliques were detached from plants grown in soil for 8 weeks. In total, 50 siliques were measured for each plant genotype. Biological triplicates were averaged and statistically treated using a Student's *t* test (**P*<0.01). Error bars indicate S.E.M.

(**D**) Comparison of leaf morphology. The fifth to tenth rosette leaves of plants fully grown in soil were photographed.

(**E**) Chlorophyll contents. The fifth leaves of 30 plants grown in soil for 4 weeks were harvested. Biological triplicates were averaged and statistically treated using a Student's *t* test (**P*<0.01). Error bars indicate S.E.M.

(**F**) Mapping of T-DNA insertion sites in *bcd1-1D* and *bcd1-1* mutants. Black arrows indicate gene loci. White arrows indicate exons of the *BCD1* gene.

(**G**) Transcript levels of the *BCD1* gene in *bcd1-1D* and *bcd1-1* mutants. Transcript levels were determined by qRT−PCR using RNA samples extracted from 2-week-old whole plants grown on MS agar plates. Biological triplicates were averaged and statistically treated using a Student's *t* test (**P*<0.01). Error bars indicate S.E.M. The y-axis is presented on a logarithmic scale for better comparison of fold changes.

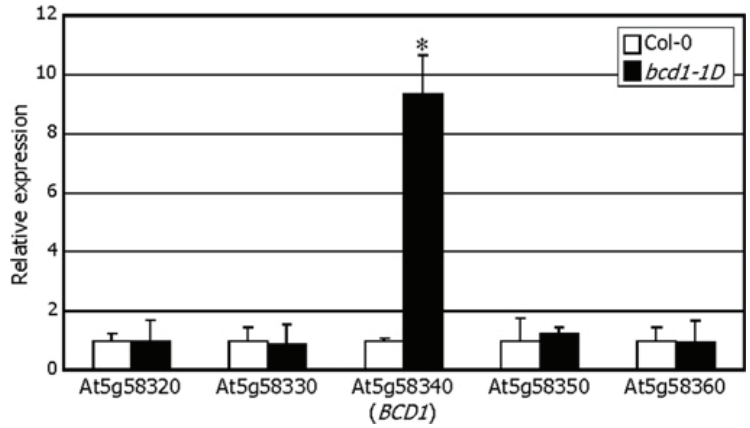

Figure 25. Relative transcript levels of the genes adjacent to the *BCD1* locus in the *bcd1-1D* mutant

Transcript levels were determined by qRT−PCR using total RNA samples extracted from 2-week-old whole plants grown on 1⁄2 × MS agar plates. Biological triplicates were averaged and statistically treated using a Student's *t* test (**P*<0.01). Error bars indicate S.E.M. Note that whereas the *BCD1* gene was activated, expression of other genes was unchanged in the *bcd1-1D* mutant.

visible phenotypes. However, the plant height and silique length were slightly but reproducibly higher and larger in the *bcd1-1* mutant than in Col-0 plants (Figures 24B and 24C). In addition, the chlorophyll content was discernibly elevated in the *bcd1-1* mutant (Figure 24E), which is in contrast with the reduced chlorophyll content in the *BCD1*-overexpressing *bcd1-1D* mutant. These observations further support that the *BCD1* gene is associated with the *bcd1-1D* mutant phenotypes. It was also implicated that the *BCD1* gene might underlie the chlorotic process observed in the *bcd1-1D* mutant leaves.

BCD1 is a member of the MATE family

Database analysis revealed that the *BCD1* gene encodes a membrane protein with 12 potential α-helical transmembrane domains (Figures 26A and 26B). Sequence analysis of the encoded protein showed that the BCD1 protein is highly homologous with other known MATE proteins (Figure 27) (Li *et al*., 2002; Rogers and Guerinot, 2002), such as ALF5 (Diener *et al*., 2001), DTX1 (Li *et al*., 2002) and TT12 (Debeaujon *et al*., 2001; Marinova *et al*., 2007), showing that it belongs to the MATE transporter family (Li *et al*., 2002) with its N-terminus towards the cytoplasmic side (Figure 26B).

To search for the functional nature of the BCD1 protein, I expressed the *BCD1* gene in an *Escherichia coli* mutant *acrB*, which lacks the multidrug efflux carrier AcrB system (Touzé *et al*., 2004). The transformed *E. coli* cells were grown in the presence or absence of TBA, which is toxic to *E. coli* cells, but is excreted by the AcrAB complex (Seeger *et al*., 2008). The *acrB* mutant cells did not grow on LB medium containing 400 mg/ml TBA (Figure 26C). In contrast, the *BCD1*-expressing *acrB* cells were able to continue their growth under the same toxic conditions, indicating that the BCD1 protein potentially acts as a MATE protein in *Arabidopsis*.

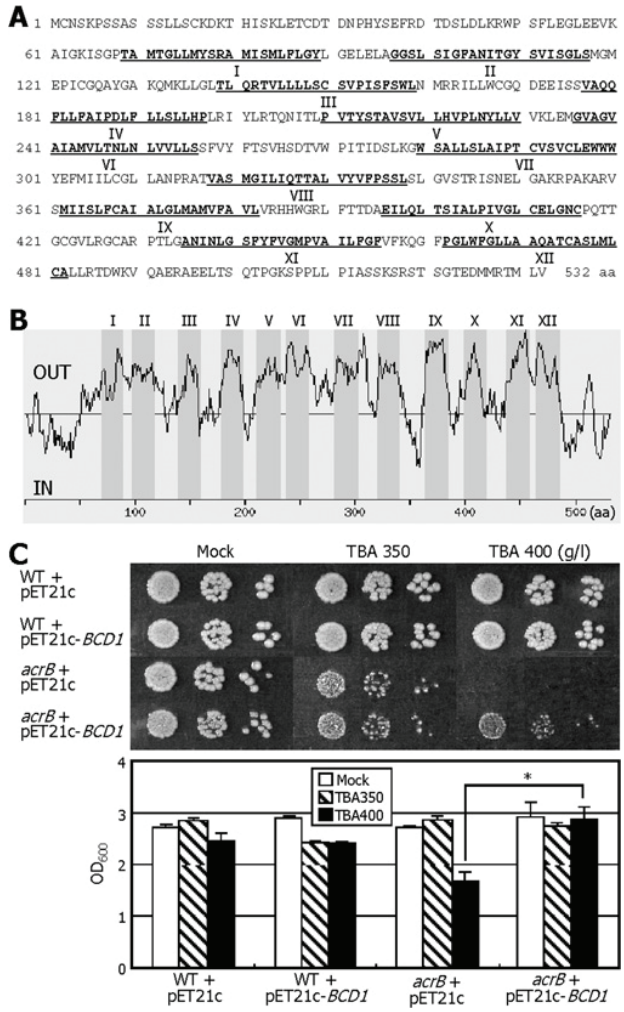

Figure 26. Biochemical characterization of the BCD1 MATE protein

(**A**) Amino acid sequence of BCD1 protein. Residues constituting the transmembrane motifs are underlined and marked I−XII. Numbers are residue positions. aa, amino acids.

(**B**) A hydrophobicity plot of the BCD1 protein was predicted using the ARAMEMNON database (http://aramemnon.botanik.uni-koeln.de/). The 12 transmembrane motifs are marked I−XII.

(**C**) Complementation of the *E. coli acrB* mutant by the *BCD1* gene. *E. coli*

acrB mutant cells were transformed with the empty expression vector or the expression vector containing the *BCD1* gene. The cultures were diluted to 10^{-3}-10^{-5} and spotted on to LB-ampicillin plates containing different concentrations of TBA (upper panel). Growth of transformed cells in liquid LB medium supplemented with ampicillin and different concentration of TBA was also measured (lower panel); OD_{600} values of cell cultures measured 24 h after the initiation of cultures are shown. Biological triplicates were averaged and statistically treated using a Student's *t* test (**P*<0.01). Error bars indicate S.E.M. WT, wild-type.

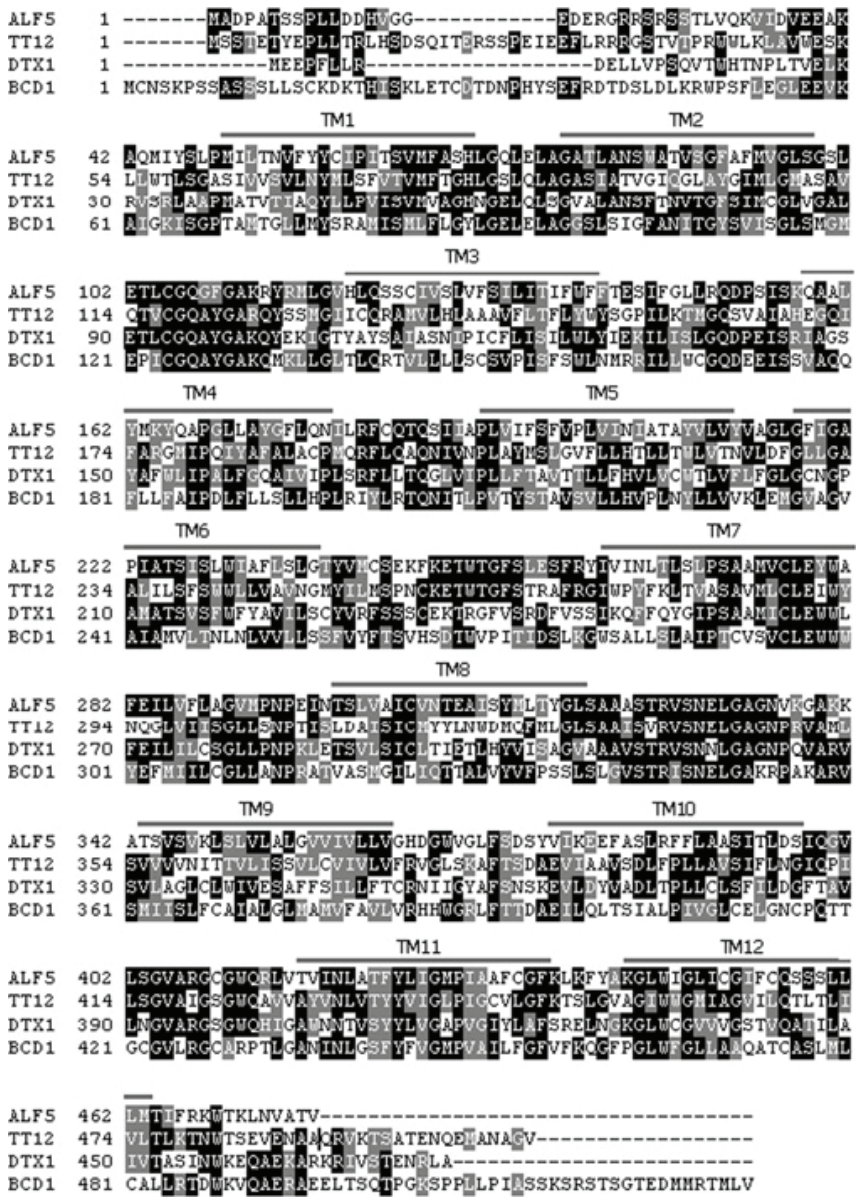

Figure 27. Multiple sequence alignment of BCD1 and related MATE transporters

Amino acid sequences were aligned using the ClustalW (http://www.genome.jp/tools/clustalw) and BoxShade (http://www.ch.embnet.org/software/BOX_form.html) tools. Residues that are absolutely conserved are shaded in black, and

biochemically conserved residues are shaded in grey. A total of 12 transmembrane motifs (TMs) are indicated. BCD1 protein and MATE transporters aligned were predicted to have N-termini towards the inside of cells. They include ALF5 (Diener *et al*., 2001), DTX1 (Li *et al*., 2002) and TT12 (Debeaujon *et al*., 2001; Marinova *et al*., 2007). A phylogenetic tree showing the relationship of the *Arabidopsis* MATE members has been reported previously (Li *et al*., 2002; Rogers and Guerinot; 2002).

***BCD1* is induced by dark and abiotic stress**

To obtain clues as to the physiological role played by the BCD1 protein, I investigated the effects of various growth hormones and environmental stress conditions on *BCD1* gene expression. Gene expression analyses by qRT⁻PCR showed that the *BCD1* gene is induced more than 6-fold in darkness (Figure 28A). The *BCD1* gene was also induced by osmotic stresses, such as high salinity and drought, as well as by mannitol and sorbitol, which impose osmotic stress on plants (Déjardin *et al*., 1999). These results suggest that the *BCD1* gene is involved in plant responses to osmotic stress.

I also examined the effects of several stress hormones on the expression of the *BCD1* gene. The *BCD1* gene was induced most strongly by ABA (Figures 28B and 29A), which is a primary growth hormone that mediates diverse aspects of plant responses to abiotic stress (Christmann *et al*., 2006). It was also induced moderately by IAA (Figures 28B and 29B). However, the *BCD1* gene was not influenced significantly by GA, PAC, ACC, BL or SA (Figure 28B). These observations support the role of the *BCD1* gene in ABA-mediated stress responses in plants.

BCD1 function is related to chlorosis

The *bcd1-1D* mutant had pale green leaves. It was found that the chlorophyll content was significantly reduced in the mutant leaves (Figures 24D and 24E). I also observed that the *BCD1* gene is induced by dark treatments and osmotic stresses, which are known to accelerate leaf senescence (Guo and Crawford, 2005; Seltmann *et al*., 2010; Yang *et al*., 2011). I therefore hypothesized that the *BCD1* gene might be related to leaf senescence.

To examine this hypothesis, I analysed the temporal expression patterns of the *BCD1* gene. qRT⁻PCR using total RNA samples extracted from different plant developmental stages showed that the transcript levels of

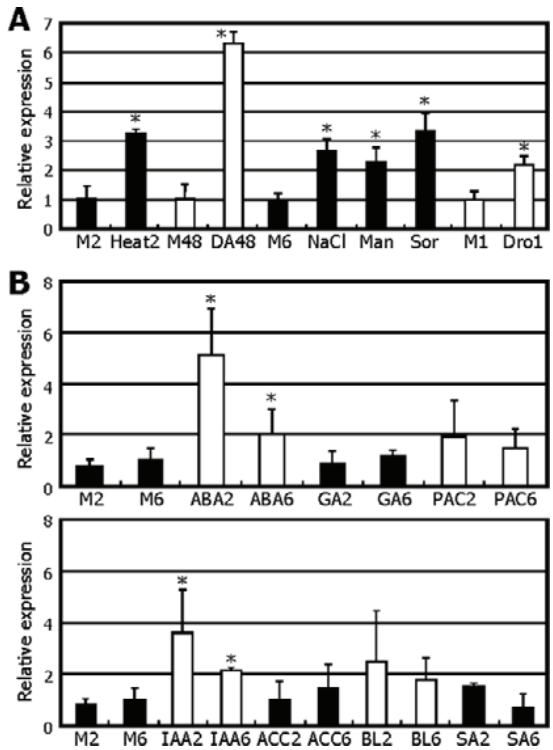

Figure 28. Induction of the *BCD1* gene in the dark and under abiotic stress conditions

Transcript levels were determined as described in **Figure 24G**. Whole plants (2 weeks old) grown on MS agar plates were used for extraction of total RNA. Statistical significance of the measurements was determined using a Student's *t* test (**P*<0.01). Error bars indicate S.E.M..

(**A**) Effects of abiotic stresses on *BCD1* gene expression. M, mock; Heat, 42°C; DA, dark; Man, mannitol 150 mM; Sor, Sorbitol 150 mM; Dro, drought. Numbers indicate the duration (in h) of treatment.

(**B**) Effects of growth hormones on BCD1 gene expression. The growth hormones and chemicals examined were ABA (20 μM), GA (20 μM), PAC (20 μM), IAA (20 μM), ACC (20 μM), BL (20 μM) and SA (100 μM). Numbers indicate the duration (in h) of treatment. M, mock.

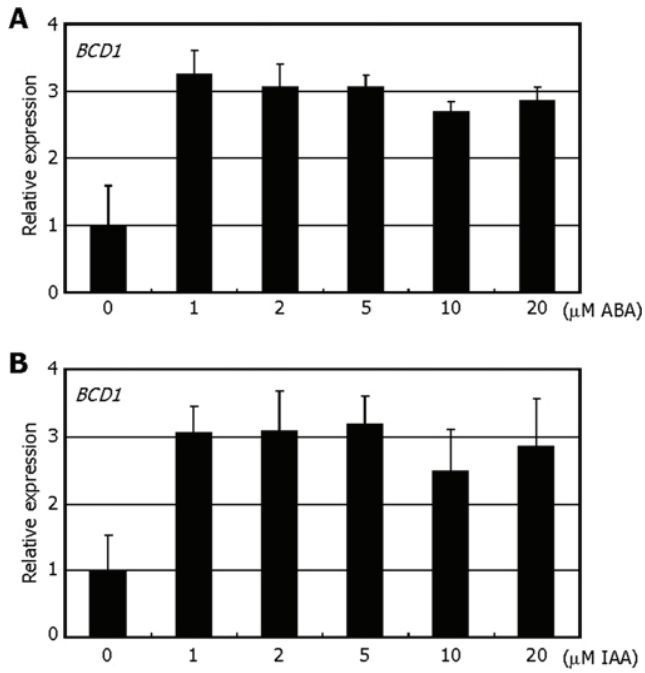

Figure 29. Effects of growth hormones on *BCD1* gene expression

Transcript levels were determined as described in **Figure 25**. Plants (2 weeks old) grown on MS agar plates were transferred to MS liquid cultures containing various concentrations of ABA (**A**) and IAA (**B**) and were incubated for 6 h. Whole plants were used for extraction of total RNA. Error bars indicate S.E.M..

the *BCD1* gene were gradually elevated as plants grew, reaching a plateau in later growth stages, when senescence symptoms are apparent (Figure 30A). For comparison, I also included a senescence marker gene *SAG12* encoding a cysteine protease (Noh and Amasino, 1999) in the gene expression assays. The temporal expression pattern of the *BCD1* gene exhibited expression kinetics similar to that of the *SAG12* gene. In addition, the *SAG12* gene was induced more rapidly in the *bcd1-1D* mutant that exhibits accelerated senescence, but slowly in the *bcd1-1* mutant that exhibits delayed senescence, compared with what is observed in Col-0 plants (Figure 30B; see also Figures 24A and 24D), suggesting that the *BCD1* gene may be related to leaf senescence.

To further investigate the potential involvement of the *BCD1* gene in leaf senescence, I measured the temporal content of chlorophylls throughout the plant growth stages in Col-0 plants, and *bcd1-1D* and *bcd1-1* mutants. It was observed that the chlorophyll content was higher in the *bcd1-1* mutant and lower in the *bcd1-1D* mutant compared with that in Col-0 plants throughout plant growth stages (Figure 30C). Taken together, these observations support that the *bcd1-1D* phenotypes exhibiting chlorosis are associated with premature leaf senescence.

Expression of the *BCD1* gene is regulated by iron availability

Chlorosis is a representative symptom of iron deficiency in plants. The *BCD1* gene is induced by osmotic stress and senescence, which is intimately linked with chlorosis caused by cellular damages (Duy *et al.*, 2011). Therefore a plausible hypothesis would be that the BCD1 protein might be related with iron transport in maintaining iron homeostasis under stress conditions.

To examine the possibility of the involvement of the BCD1 protein in iron homeostasis, I first examined whether the expression of the *BCD1*

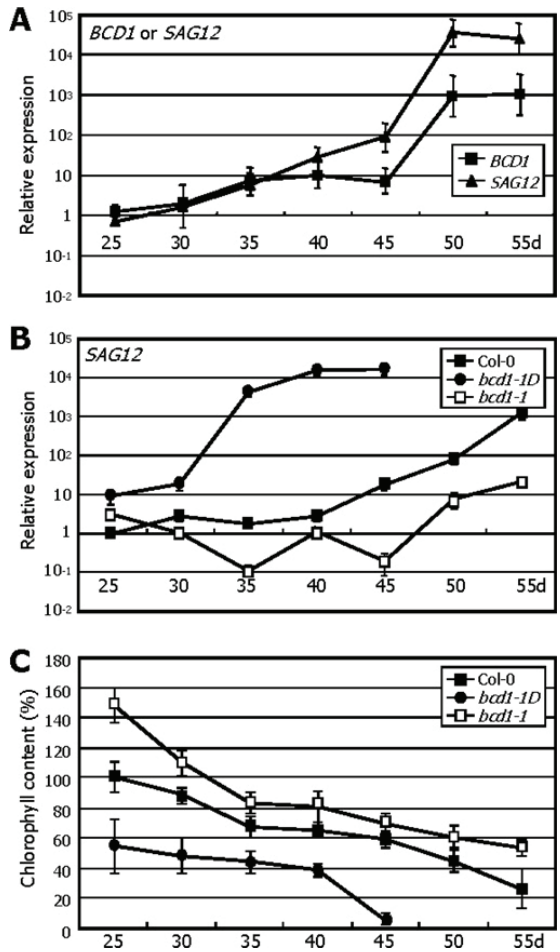

Figure 30. Temporal expression patterns of the *BCD1* gene during plant growth

(**A** and **B**) Transcript levels were determined by qRT−PCR. Biological triplicates were averaged. Error bars indicate S.E.M. (**A**) Growth-stage-dependent expression of the *BCD1* gene. Total RNA was extracted from the shoots harvested at the indicated time points (d, days after cold imbibitions). The *SAG12* gene was also included in the assays.

(**B**) Temporal expression patterns of the *SAG12* gene in *bcd1-1D* and *bcd1-1* mutants. Fifth rosette leaves of approximately 30 plants grown in soil were harvested at the indicated time points for extraction of total RNA.

(**C**) Measurements of chlorophyll content. Fifth rosette leaves of approximately 30 plants grown in soil were harvested at the indicated time points. Biological triplicates were averaged at individual time points for each plant genotype. Error bars indicate S.E.M.

gene is influenced by iron-excessive and -deficient conditions. qRT−PCR assays revealed that the *BCD1* gene was induced approximately 13-fold in the shoots when exposed to excess iron (Figure 31A). In addition, the *BCD1* expression was regulated by iron content in a dosage-dependent manner (Figure 32). Notably, the inductive effects were iron-specific. Magnesium did not affect the expression of the *BCD1* gene (Figure 31A). The *BCD1* gene was more highly expressed in the roots than in the shoots, and it was induced only slightly in the roots by excess iron (Figure 31A), suggesting that the induction of the *BCD1* gene by excess iron is physiologically more important in the shoots.

To examine the effects of iron deficiency on *BCD1* gene expression, plants were exposed to 300 μM ferrozine, which is a potent iron chelator (Long *et al*., 2010). The results showed that iron deficiency suppressed the *BCD1* gene expression primarily in the roots (Figure 31B). These observations suggest that the *BCD1* gene is regulated by iron availability.

To further examine the effects of iron availability on *BCD1* gene expression, a promoter sequence covering an approximately 2 kb sequence region upstream of the transcription start site of the *BCD1* gene was fused transcriptionally to a GUS-coding sequence, and the construct was transformed into Col-0 plants. Histochemical assays showed that GUS activity was relatively low in plants grown under normal growth conditions (Figure 31C). In contrast, excessive iron elevated the GUS activities in the vascular tissues of the leaves and roots. In the leaves, the elevation of GUS activity was most prominent in the hydathode, a specialized secretory gland that secretes water containing salts and metals. It was also detected in the root tip regions, which is also supported by the public microarray data available in the GENEVESTIGATOR database (http://www.genevestigator.com/gv/). However, it was reduced significantly in the leaves and roots when plants

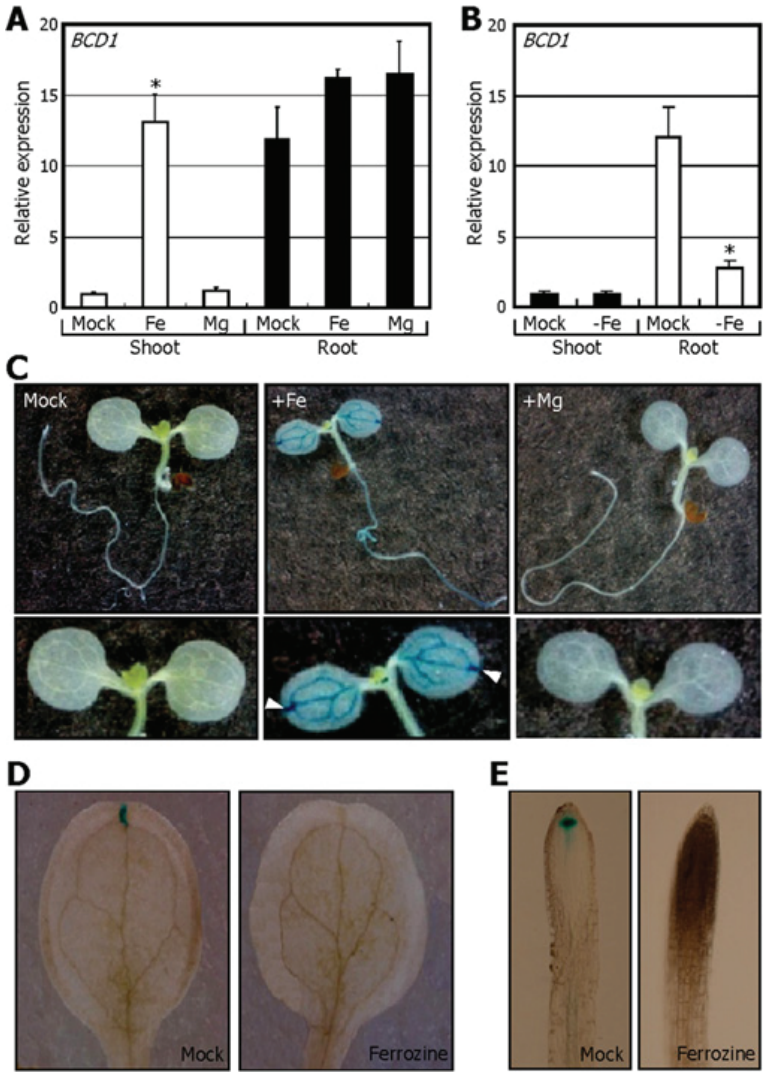

Figure 31. *BCD1* gene expression is regulated by iron availability

(**A** and **B**) Shoots and roots were harvested separately for extraction of total RNA. Transcript levels were determined by qRT−PCR. Biological triplicates were averaged and statistically treated using a Student's *t* test (**P*<0.01). Error bars indicate S.E.M. (**A**) BCD1 gene expression in response to exposure to excess iron. Plants (2 weeks old) grown on iron-sufficient agar plates were transferred to liquid cultures supplemented with excess iron (400

μM $FeSO_4$) or magnesium (6 mM $MgSO_4$) and were incubated for 24 h. (**B**) Effects of iron deficiency on *BCD1* gene expression. Plants (2 weeks old) grown on iron-sufficient agar plates were transferred to liquid cultures supplemented with 300 μM ferrozine and incubated for 24 h.
(**C**⁻**E**) Distribution of GUS activities in plant tissues. The pBCD1⁻GUS fusion construct was transformed into Col-0 plants. Transgenic plants (2 weeks old) grown on iron-sufficient agar plates were transferred to liquid cultures containing either excess amounts of iron (Fe, 400 μM $FeSO_4$) or magnesium (Mg, 6 mM $MgSO_4$) (**C**) or 300 μM ferrozine (**D** and **E**) and incubated for 24 h. The plant materials were subject to GUS staining. To detect lower GUS activity (**D** and **E**), plants were stained for longer compared with (**C**). In (**C**), the lower panels show an enlarged view of the aerial plant parts.

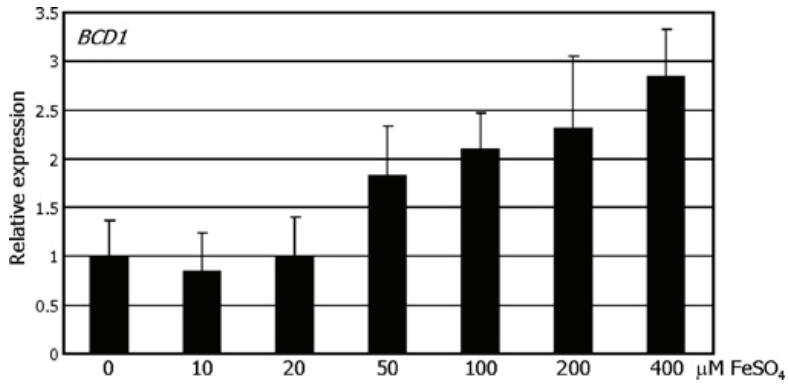

Figure 32. Effects of various concentrations of iron on *BCD1* gene expression

Transcript levels were determined as described in **Figure 25**. Plants (2 weeks old) grown on iron-sufficient agar medium plates were transferred to liquid medium cultures containing various concentrations of $FeSO_4$ and were incubated for 24 h. Whole plants were used for extraction of total RNA. Error bars indicate S.E.M.

were treated with the iron chelator ferrozine (Figures 31D and 31E). This observation is also consistent with the suppressive effects of ferrozine on *BCD1* gene expression (Figure 31B). These data confirm that the *BCD1* gene is regulated transcriptionally by iron availability.

It was also envisaged that induction of the *BCD1* gene by osmotic stress might be associated with iron concentrations in cells and thus BCD1 might play a role in iron transport when excessive iron is released into the cytosol in cells damaged by osmotic stress and senescence. Consistent with this prediction, the *BCD1* gene was synergistically induced by ABA and iron (Figure 33). In contrast, ABA induction of the *BCD1* expression was suppressed by ferrozine treatment, further supporting the role of BCD1 in iron homeostasis under stress conditions.

Iron content is lower in the *bcd1-1D* mutant

The transcriptional regulation of the *BCD1* gene by iron availability suggested that the BCD1 protein plays a role in regulating iron distribution in plants. I first measured the iron content in the *bcd1-1D* and *bcd1-1* mutants by employing the Perls iron-staining method (Long *et al*., 2010). Perls staining assays revealed that whereas ferric iron was detected at a lower level in the leaves and primary roots of the *bcd1-1D* mutant, it was detected at a higher level in the same tissues of the *bcd1-1* mutant (Figures 34A and 34B).

In the leaves, ferric iron was detected mainly in the leaf tip area in Col-0 plants. Notably, the stained area was maintained but the intensity was elevated in the *bcd1-1* mutant leaves (Figure 34A). These observations suggest that the *BCD1* gene is functional in the area, where chlorosis initiates under osmotic stress (Russin *et al*., 1996). A similar pattern was also observed in the roots: whereas the stained area was maintained, the

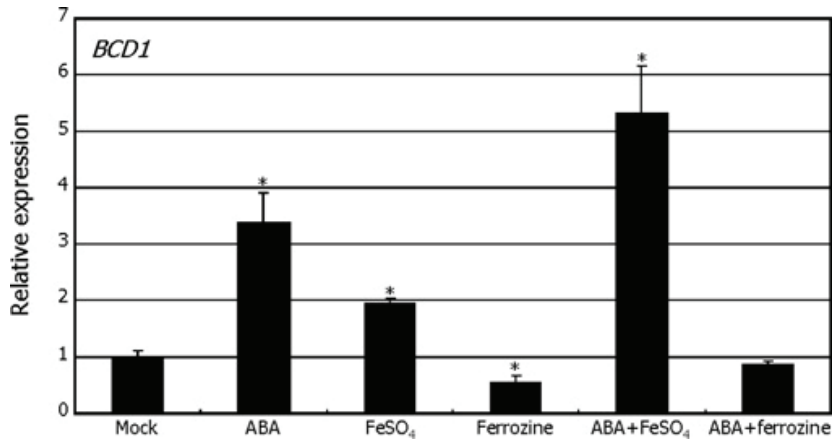

Figure 33. Effects of ABA and iron on *BCD1* gene expression

Transcript levels were determined as described in **Figure 25**. Plants (2 weeks old) grown on iron-sufficient agar medium plates were transferred to liquid medium cultures containing 20 μM ABA, 300 μM ferrozine and/or 400 μM $FeSO_4$ and were incubated for 6 h. Whole plants were used for extraction of total RNA. Statistical significance of the measurements was determined using a Student's *t* test (**P*<0.01). Error bars indicate S.E.M..

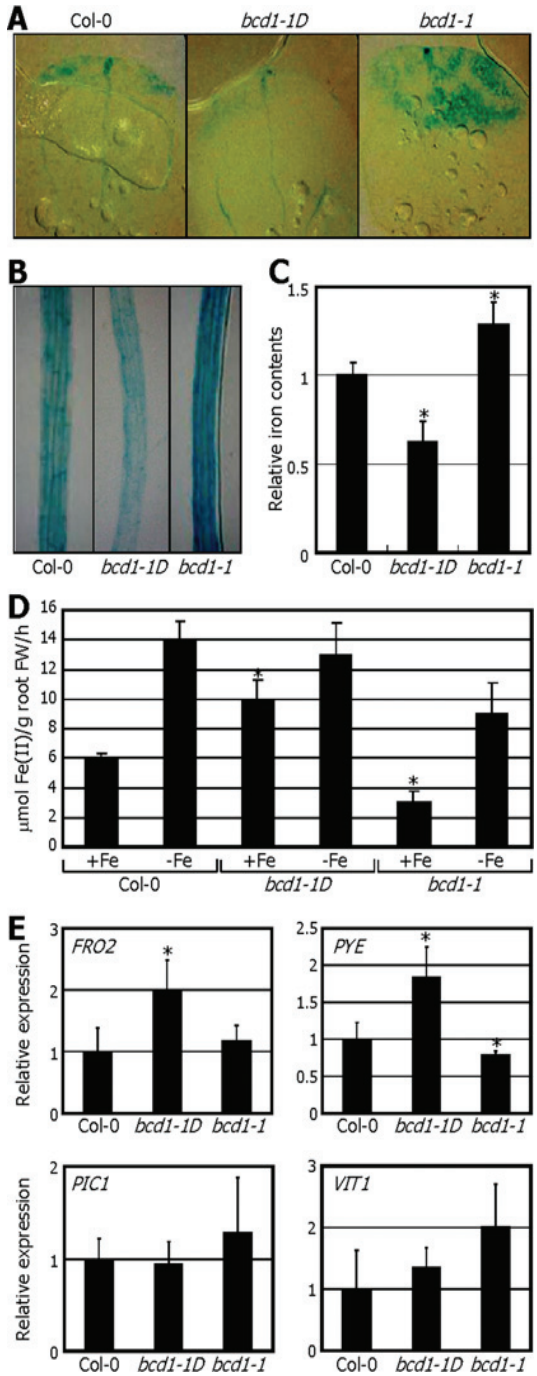

Figure 34. Iron content is reduced in the *bcd1-1D* mutant

(**A** and **B**) Plants (2 weeks old) grown on iron-sufficient agar plates were subject to Perls staining. (**A**) Perls staining of leaf samples. (**B**) Perls staining of root samples.

(**C**) Iron content in *bcd1-1D* and *bcd1-1* mutants. Whole plants (3 weeks old) grown on iron-sufficient agar plates were harvested for the measurements of iron contents. A value of 1 is equivalent to 90 p.p.m. Biological triplicates were averaged and statistically treated using a Student's *t* test (**P*<0.01). Error bars indicate S.E.M.

(**D**) Fe(III) chelate reductase activity assays. Plants (2 weeks old) grown on iron-sufficient agar medium plates were shifted to either iron-sufficient or iron-deficient agar medium plates for 3 days. Root samples were used for the assays. Biological triplicates were averaged and statistically treated using a Student's *t* test (**P*<0.01). Error bars indicate S.E.M..

(**E**) Transcript levels of iron transporter and homeostasis genes in *bcd1-1D* and *bcd1-1* mutants. Transcript levels were determined by qRT−PCR using RNA samples extracted from the shoots of 2-week-old plants grown on iron-sufficient agar plates. Biological triplicates were averaged and statistically treated using a Student's *t* test (**P*<0.01). Error bars indicate S.E.M..

intensity was lower in the *bcd1-1D* roots but higher in the *bcd1-1* roots (Figure 34B). Moreover, direct measurements of the iron content also showed that the iron concentration was lower in the *bcd1-1D* mutant but higher in the *bcd1-1* mutant (Figure 34C). It was therefore concluded that the BCD1 protein functions in modulating iron redistribution in plants, possibly by excreting excess iron from damaged plant cells under stress conditions (see the Discussion).

Fe(III) chelate reductase activity, which reflects iron availability in plants, is induced under iron-limiting conditions (Rogers and Guerinot, 2002). I found that the Fe(III) chelate reductase activity is elevated in the *bcd1-1D* mutant but reduced in the *bcd1-1* mutant when they were grown under iron-sufficient conditions (Figure 34D), which is certainly related to alterations of iron contents in the mutant plants.

To further investigate molecular mechanisms underlying the BCD1 regulation of iron homeostasis, I analysed the expression of genes involved in iron transport and metabolism, such as *FIT*, *FRO2*, *IRT1*, *POPEYE (PYE)*, *VIT1* and *PIC1*, in the mutant plants. Among the genes examined, the *FRO2* and *PYE* genes, which are induced under iron-deficient conditions to maintain iron homeostasis (Robinson *et al*., 1999; Long *et al*., 2010), were up-regulated in the *bcd1-1D* mutant (Figure 34E). The transcript level of the *IRT1* gene was also elevated slightly but reproducibly in the mutant (Figure 35). In contrast, expression of *FIT1* and genes encoding organelle-localized proteins was not influenced in the mutant.

The results suggested that the chlorotic appearance of the *bcd1-1D* mutant is caused by reduced iron content. I examined whether the *bcd1-1D* mutant phenotypes are recovered by exogenous iron feeding. The *bcd1-1D* and *bcd1-1* mutant plants were grown in soil either with or without iron complementation, and the overall growth appearance and leaf morphology were compared with those of Col-0 plants grown under identical conditions.

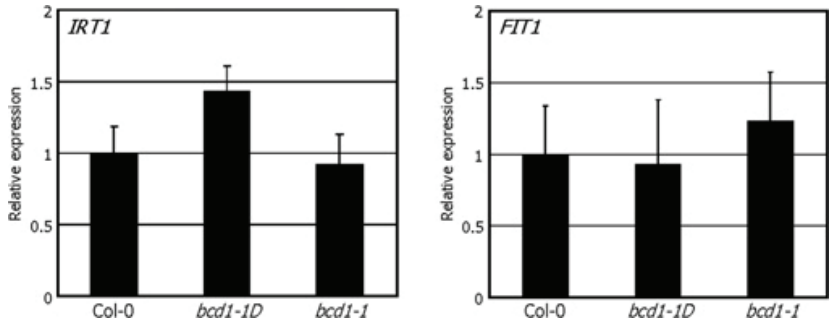

Figure 35. Transcript levels of *IRT1* and *FIT1* genes in *bcd1-1D* and *bcd1-1* mutants

Transcript levels were determined by qRT−PCR using RNA samples extracted from the shoots of 2-week-old plants grown on iron-sufficient agar plates. Biological triplicates were averaged. Error bars indicate S.E.M..

Overall plant growth and morphologies of the *bcd1-1D* and *bcd1-1* mutants were not influenced by iron feeding (Figure 36A). However, the chlorotic phenotype of the *bcd1-1D* mutant leaves was markedly recovered by iron feeding (Figure 36A). Whereas the rosette leaves of the *bcd1-1D* mutant exhibited chlorosis under normal growth conditions, it was efficiently rescued by iron feeding (Figure 36B).

I next examined whether the rescuing effect was specific to iron. The *bcd1-1D* mutant was fed with either $FeSO_4$ or $MgSO_4$ under the assay conditions described above. The leaf chlorosis of the mutant was not rescued by magnesium feeding (Figure 36C), unlike the effects of iron (Figure 36B). These observations confirm that the chlorotic phenotype of the *bcd1-1D* mutant leaves is due to iron deficiency.

BCD1 protein is localized to the Golgi complex

The plant MATE proteins characterized so far are localized to either the vacuolar membranes or plasma membranes, which are two primary sites for iron uptake and sequestration (Jeong and Guerinot, 2009). To examine where the BCD1 protein is localized in plant cells, an RFP-coding sequence was fused in-frame to the 5'-end of the *BCD1* gene, and the RFP-BCD1 fusion construct was expressed transiently in *Arabidopsis* protoplasts. Fluorescence confocal microscopy showed that RFP signals were widely distributed in a granular pattern in the cytoplasm (Figure 37A).

I therefore employed several green fluorescent protein (GFP)-tagged organelle-specific markers to determine precisely the subcellular distribution of the BCD1 protein. Each of the GFP-tagged markers and RFP-BCD1 fusion construct were coexpressed in *Arabidopsis* protoplasts. It was found that the distribution pattern of the RFP−BCD1 fusion did not overlap with those of the peroxisomal and mitochondrial markers (Figures 37A and 37B). In contrast, the RFP signals strikingly overlapped with the GFP signals from

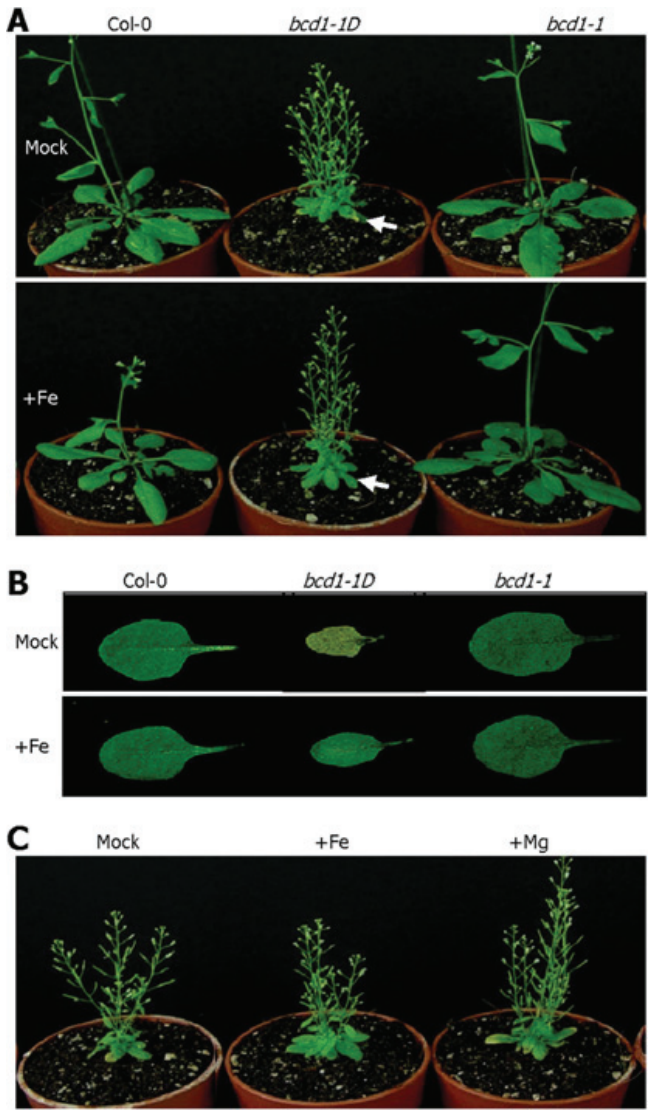

Figure 36. Recovery of the chlorotic phenotype of *bcd1-1D* mutant leaves by iron feeding

(**A** and **B**) Recovery of *bcd1-1D* leaf chlorosis by iron feeding. Plants (1 week old) grown in soil under normal conditions were watered with either tap water (Mock) or a 400 μM $FeSO_4$ solution (+Fe) for an additional 4 weeks before taking photographs. (**A**) Arrows indicate the chlorotic and

rescued rosette leaves of the *bcd1-1D* mutant. (**B**) Representative rosette leaves before and after iron feeding.

(**C**) Effects of iron and magnesium on *bcd1-1D* leaf chlorosis. *bcd1-1D* mutants (1 week old) grown in soil were fed with either 400 μM $FeSO_4$ (+Fe) or $MgSO_4$ (+Mg) solution for an additional 4 weeks under identical conditions.

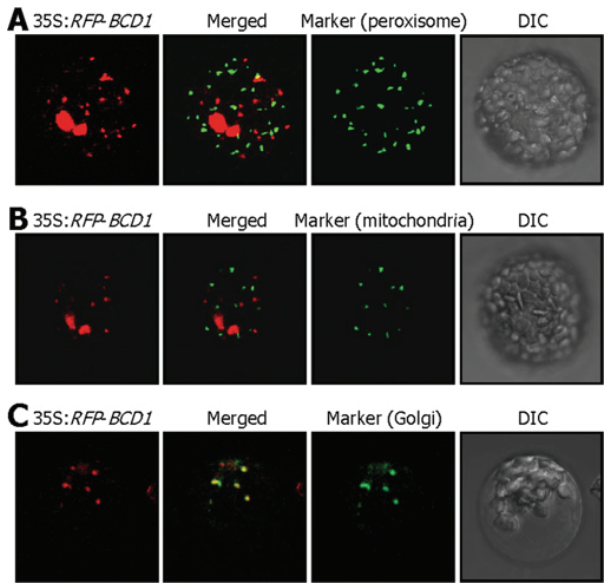

Figure 37. Golgi localization of BCD1 protein

An *RFP-BCD1* gene fusion was transiently co-expressed with intracellular organelle-specific markers in *Arabidopsis* protoplasts and visualized by DIC and fluorescence microscopy. Binary plasmids for organelle markers were obtained from the ABRC (http://www.arabidopsis.org).

(**A**) Co-expression of RFP−BCD1 with a peroxisome marker (CD3-979).

(**B**) Co-expression of RFP−BCD1 with a mitochondrial marker (CD3-987).

(**C**) Co-expression of RFP−BCD1 with a Golgi-complex marker (CD3-963).

the Golgi-specific marker (Figure 37C), showing that the BCD1 protein is localized in the Golgi complex.

Taken altogether, the observations support that the BCD1 MATE protein is associated with excretion of excess iron, which would be produced in chlorotic cells under osmotic stress conditions and senescing leaf cells.

DISCUSSION

Iron homeostasis and abiotic stress

Plants possess a wide array of homeostatic mechanisms to maintain appropriate levels of intracellular and intercellular iron, reflecting the physiological significance of iron homeostasis in diverse plant growth and developmental process and responses to environmental stresses (Tarantino *et al*., 2003; Murgia *et al*., 2007; Jeong and Guerinot, 2009). A number of iron transporters and reductases have been identified, and their roles in iron uptake, intracellular sequestration and intercellular transport have been characterized in many plant species (Curie and Briat, 2003; Jeong and Guerinot, 2009). These transporters and enzymes play a central role in iron redistribution upon stimulation by developmental and environmental cues. Iron redistribution is particularly important in damaged cells exposed to osmotic stress and senescing leaf cells. The recycling of iron certainly contributes to plant fitness and energy conservation in nature, where the amount of soluble iron is limited (Leopold, 1961; Jeong and Guerinot, 2009).

In the present study, I demonstrated that the BCD1 protein, which has 12 transmembrane domains and high sequence homology with plant MATE transporters, plays a role in iron homeostasis and, perhaps, transport of excess iron released from leaf cells damaged by osmotic stresses or senescence.

It has been comprehensively documented that senescence-associated nutrient mobilization is an active process that helps plants adapt to abrupt environmental changes and achieve reproductive success (Himelblau and Amasino, 2001). More than 40% of major nutrients in the leaves is redistributed during senescence (Himelblau and Amasino, 2001), necessitating that nutrient recycling and reallocation should be tightly controlled (Leopold,

1961; Himelblau and Amasino, 2001). Iron redistribution is a particularly important cellular process. Chloroplasts contain approximately 80% of iron present in the leaves (Graziano *et al*., 2002; Gepstein, 2004). It has been found that the transcripts of the ferritin genes accumulate to an extremely high level during leaf senescence (Murgia *et al*., 2007). Consistent with the role of ferritin as an effective storage of intracellular iron, the loss-of-function *fer1-2* mutants exhibit an early onset of senescence. In addition, a number of iron transporters would also be involved in the reallocation of nutrients in the senescence processes. For example, the YSL1 and YSL3 transporters have been implicated in the mobilization of transition metals from older leaves in *Arabidopsis* (Waters *et al*., 2006). Therefore it seems that the differential progression of senescence in the *bcd1-1D* and *bcd1-1* mutants would be due to disturbance in iron homeostasis.

Abiotic stress profoundly affects iron homeostasis. The ferritin genes are induced by oxidative stress, wounding and pathogen attacks through stress hormone signalling cascades mediated by ABA and SA (Lobreaux *et al*., 1992; Fobis-Loisy *et al*., 1995; Gaymard *et al*., 1996; Petit *et al*., 2001). The root system is a main target that is influenced at the first step by abiotic stress and iron deficiency. It has been shown that inhibition of root growth by cytokinin, osmotic stress and ABA suppresses the iron-deficiency response (Séguéla *et al*., 2008), indicating that root growth regulation is closely linked with the iron-uptake response. However, little is known about how iron redistribution is regulated and what molecular events are involved in the leaves that are exposed to disrupted iron redistribution.

I found that the *BCD1* gene is regulated by iron availability in addition to osmotic stress and senescence. Whereas the *BCD1* gene is induced by exposure to excessive iron, it is suppressed by iron deficiency. Of particular interest is that excess iron induces the *BCD1* gene in the vascular tissues of the leaves, particularly in the hydathodes through which

water containing salts and metals is secreted, supporting the notion that the BCD1 transporter is possibly involved in intercellular iron transport and/or excretion. The *bcd1-1D* mutant exhibits leaf chlorosis, certainly due to reduced iron content. The reduced iron content in the *bcd1-1D* mutant is likely to be due to ectopic expression of the *BCD1* gene and thus excess excretion of iron to the outside plant tissues. It is likely that the BCD1 protein plays a more important role under iron-excessive conditions by exporting toxic iron from the cytoplasm. The fact that the *BCD1* gene is induced during senescence and in response to osmotic stress, when excess iron is released, suggests that the BCD1 protein redistributes or evacuates excess iron released from damaged cells.

Is BCD1 an iron transporter?

Prokaryotic MATE proteins efflux antibiotics, such as kanamycin, streptomycin and norfloxacin, and toxic small organic molecules, including ethidium bromide (Morita *et al*., 1998). Plant MATE proteins are also involved in the ransport of small organic molecules, such as tetramethyl ammonium (Diener *et al*., 2001), flavonoids (Debeaujon *et al*., 2001), SA (Nawrath *et al*., 2002), plant-derived alkaloids, antibiotics and other toxic compounds (Li *et al*., 2002).

The FRD3 MATE protein plays a role in iron homeostasis (Rogers and Guerinot, 2002). Disruption of the *FRD3* gene leads to activation of the iron-deficiency response, and excessive iron accumulates in the mutant. It has been reported that the FRD3 protein mediates iron translocation from the roots to the shoots by loading citrate into the xylem (Durrett *et al*., 2007). Fe(III)-citrate is a major form of iron transport, which is thought to be involved in long-distance iron transport (Durrett *et al*., 2007).

The results suggest that the BCD1 protein contributes to iron homeostasis, on the basis of the following observations. It has a structural

characteristic of the MATE transporters and is regulated by iron availability, mainly in the vascular tissues. Furthermore, iron content is reduced in the *bcd1-1D* mutant that exhibits chlorosis, but the chlorotic leaves are rescued by exogenous iron feeding. I also found that the BCD1 protein is localized in the Golgi complex. The Golgi complex is a subcellular site where macromolecules are modified, sorted and packaged for delivery to their destinations. In particular, it also plays a role in detoxifying and secreting toxic compounds. The BCD1 transporter may function in transporting iron with its chelators, such as nicotianamine and citrate, via the Golgi-associated intercellular transport and maintain proper concentration of iron in the cytoplasm of stress-damaged cells and senescing cells.

Considering the necessity of functional diversity and specificity for iron transport in plant cells, it is envisioned that there would be multiple iron transporters or facilitators in plants. At least some of the iron transporters may be MATE members in addition the BCD1 protein. Assuming that multiple MATE proteins act as iron transporters, both high- and low-affinity systems would be required for maintenance of iron homeostasis, which can be achieved by balanced iron uptake, transport and secretion (Hall and Williams, 2003). In addition, diverse cellular and organellar transporters would be necessary to ensure iron redistribution and homeostasis. Furthermore, specific developmental and/or environmental responses would add additional complexity in the putative network of iron transport systems in plant cells. It will be interesting to screen the MATE proteins to see whether there are any functional homologues of the BCD1 protein in *Arabidopsis*.

It has recently been reported that the BCD1 protein is associated with the membranes of small organelles (Burko *et al*., 2011). It has been suggested that the BCD1 protein determines the rate of organ initiation by modulating unidentified leaf-borne signals. The previous observation may be

related to the reduced apical dominance and production of more leaves from the shoot apical meristem observed in the *bcd1-1D* mutant. The results show that the alterations in organ initiation that have been observed in the previous work may be indirect effects of iron deficiency because of overexpression of the *BCD1* gene. It is also possible that the BCD1 transporter may also mediate intercellular transport of as yet unidentified materials other than iron chelators, which would be required for organogenesis. Anatomical studies on the shoot apical meristem and leaf primordia of the *bcd1-1D* and *bcd1-1* mutants in the presence or absence of exogenous iron may help to clarify the uncertainty.

CHAPTER 3

High-sensitivity fluorescence imaging of iron in plant tissues

ABSTRACT

High-resolution imaging of spatial and temporal patterns of iron distribution is indispensable for investigating its roles in biological processes. Here, I report a method for high-sensitivity fluorescence imaging of iron, which demonstrate the amount and distribution of iron in plant tissues more precisely than conventional histochemical staining procedures. Moreover, the fluorescence turn-on method is rapid (<20 min), inexpensive to set up, and expected to be readily applicable to any plant tissues.

INTRODUCTION

Iron is a vital micronutrient that plays a critical role in a wide range of fundamental biological reactions in plants, such as electron transport chains in photosynthesis, respiration, cell division, and nitrogen fixation (Briat *et al*., 2007). The versatile roles of iron arise from its chemical property: it exists in two alternative oxidation states, ferric ion (Fe^{3+}) and ferrous ion (Fe^{2+}). However, the dual oxidation characteristic of iron potentiates oxygen toxicity by generating reactive oxygen species, which cause oxidative damage to biomolecules. Therefore, plants tightly maintain iron homeostasis through coordinated regulation of its uptake, transport, and storage (Jeong and Guerinot, 2009).

The physiological roles of iron have been explored by molecular genetic and biochemical studies of mutant plants exhibiting defects in iron metabolism and by measurements of iron contents via inductively coupled plasma mass spectrometry (Long *et al.,* 2010). In recent years, there has been a growing concern for high-resolution imaging of iron distribution in plant tissues, which is a prerequisite for understanding the dynamic iron metabolic processes in plant growth and development and environmental stress responses. X-ray fluorescence microtomography and electron microscopy coupled to inelastically scattered electrons have been adopted for investigating the specific localization of iron in plants (Lanquar *et al*., 2005; Kim *et al*., 2006). However, because of technical difficulties associated with these methods, histochemical staining methods, such as Perls staining (Seo *et al*., 2012a), are still routinely used. Although the Perls staining method has been improved (Roschzttardtz *et al*., 2009; Bournier *et al*., 2013; Roschzttardtz *et al*., 2013), a major sink of iron in plants, the leaves, is poorly stained by histochemical methods, and the resolution of iron detection remains poor. The experimental procedures involved are also complex and

time-consuming.

An array of fluorescent probes has been developed for imaging of diverse biomolecules in plants and animals. Unlike absorbance-based probes for iron detection, such as the blue precipitate of Perls staining and the black precipitate of DAB-intensified Perls (Perls/DAB) staining, fluorescence-based sensors are highly sensitive, providing nearly infinite contrast by emitting light on a dark background. In addition to visualization of specific biomolecules with high sensitivity, detection by fluorescent probes is simple, precise, and quantitative. Recently, several fluorescent probes have been synthesized for the detection of iron in cells (Xiao and Qian, 2003; Liu and Wu, 2012; Sahoo *et al*., 2012; Goswami *et al*., 2013; Hirayama *et al*., 2013). However, these have not yet been tested for their application in plant tissues.

In this study, I report a method for high-sensitivity fluorescence imaging of iron, which demonstrates the amount and distribution of iron in plant tissues.

MATERIALS AND METHODS

Synthesis of 7-(4-methylpiperazin-1-yl)-4-nitrobenzo-2-oxa-1,3-diazole (MPNBD)

MPNBD was prepared following the procedure that has been described previously (Xiao and Qian, 2003), but with some modifications. 4-chloro-7-nitrobenzofurazan (0.5 g, 2.5 mmol) was dissolved in $CHCl_3$ (20 mL). 1-methylpiperazine (0.28 mL, 2.5 mmol) was added and stirred for 30 min at room temperature. The reaction mixture was concentrated on a rotary evaporator. The residue was purified by column chromatography (SiO_2, eluent: CH_2Cl_2/MeOH = 10/1) to afford 0.43 g of orange powder in 66% yield. ^{1}H- and ^{13}C-NMR spectra were measured on a Varian NMR System 500 MHz NMR Spectrometer (Varian, Palo Alto, CA). Data were acquired as follows; chemical shifts in ppm from tetramethylsilane as an internal standard in $CDCl_3$, integration, multiplicity (s = singlet, d = doublet, t = triplet). ^{1}H-NMR (500 MHz, $CDCl_3$): δ ppm 2.32 (s, 3H), 2.61 (t, 4H), 4.06 (t, 4H), 6.25 (d, 1H), 8.35(d, 1H). ^{13}C-NMR (500 MHz, $CDCl_3$): δ ppm 145.18, 144.83, 144.78, 135.10, 123.54, 102.42, 54.55, 49.35, 45.84. HR-MS(FAB+) calculated for 264.1097 m/z, observed for 264.1097 m/z

Metal ion sensing by MPNBD

A stock solution of MPNBD (14.81 μM) and metal solutions of $FeCl_3.6H_2O$ (4.51 mM), $FeCl_2.4H_2O$ (5.90 mM), $CuCl_2.2H_2O$ (7.10 mM), $CrCl_3.6H_2O$ (4.24 mM), $CaCl_2$ (6.53 mM), $MgCl_2.6H_2O$ (6.70mM), $MnCl_2.4H_2O$ (3.48 mM), $NiCl_2$ (4.65 mM), and $ZnCl_2$ (4.81 mM) were prepared in ethanol. Metal solutions of KCl (4.60 mM) and NaCl (6.55 mM) were prepared in water. Two ml of the MPNBD stock solution and each of metal ion stock solutions were mixed. Ethanol was then added to each mixture to match the concentration of MPNBD in each mixture to 9.88 μM. The mixtures were analyzed by UV-Vis spectroscopy (Sinco, S-3100, Seoul, Korea) and

fluorophotometry (JASCO, FP-6500, Tokyo, Japan) at room temperature. Light source for fluorophotometry was the 150W Xenon lamp with a diffraction grating to select the excitation light. The emission spectra were measured in the wavelength range from 490 to 750 nm under the excitation at 470 nm.

Plant materials and growth conditions

Arabidopsis thaliana ecotype Columbia-0 (Col-0) was used. The *Arabidopsis* plants were grown on 1/2 X Murashige & Skoog (MS) media containing 0.6% (w/v) agar (hereafter referred to as MS-agar plate) in growth chamber at 22^{o}C with white light illumination (120 μmol photons $m^{-2}s^{-1}$) provided by fluorescent FLR40D/A tubes (Osram, Seoul, Korea) under long day conditions (16-hour light and 8-hour dark).

Staining of iron in *Arabidopsis* plants

Four-day-old *Arabidopsis* plants grown on MS-agar plates were used. The Perls and Perls/DAB (3,3'-diaminobenzidine) staining procedures were conducted as described previously (Mancuso *et al*., 2006; Hirayama *et al*., 2013). For the Perls staining, plants were vacuum infiltrated with a solution containing equal volumes of 4% (v/v) HCl and 4% (w/v) $K_4Fe(CN)_6$ for 15 minutes and subsequently incubated for 30 minutes in complete darkness at room temperature. For the DAB-intensified Perls staining, the Perls-stained plants were washed with distillated water, incubated in a methanol solution containing 0.01 M NaN_3 and 0.3% (v/v) H_2O_2 for 1 hour, and then washed with 0.1 M phosphate buffer (pH 7.4). For the DAB intensification, the plants were incubated for 10 to 30 minutes in 0.1 M phosphate buffer (pH 7.4) containing 0.0025% (w/v) DAB, 0.005% (v/v) H_2O_2, and 0.005% (w/v) $CoCl_2.6H_2O$.

For fluorescence imaging of iron with MPNBD, four-day-old

Arabidopsis plants were briefly washed with ethanol and vacuum infiltrated with a ethanol solution containing 50 μM MPNBD for 5 minutes. The plants were incubated in complete darkness for 10 minutes and washed with ethanol before fluorescence microscopy.

Fluorescence microscopy

Plants stained by the Perls and Perls/DAB methods were analyzed using the Olympus BX51 microscope (Olympus, Tokyo, Japan). Images were acquired using the Olympus DP70 digital camera system and processed with the DPController and DP Manager softwares (Olympus). For fluorescence detection in the MPNBD-treated plants, the U-MWB2 fluorescence detection system (excitation filter BP460-490, dichronic mirror DM500, and barrier filter BA520IF) (Olympus) was used. Light was provided by a 100W High Pressure Mercury Burner (Olympus, BH2-RFL-T3). Fluorescence images were taken with an exposure time of 250 ms at 40X magnification. High-magnification images were visualized using the Zeiss LSM510 confocal microscope (Carl Zeiss, Jena, Germany) with the following filter setup: excitation 488 nm, emission BP510-530 nm. Fluorescence images were analyzed using the ImageJ software (http://rsbweb.nih.gov/ij/), as described previously (Mancuso *et al*., 2006; Hirayama *et al*., 2013).

RESULTS

When considering fluorescent probes that may be appropriate for selective detection of iron in plant tissues, I chose MPNBD (7-(4-methylpiperazin-1-yl)-4-nitrobenz-2-oxa-1,3-diazole) as a photoinduced electron transfer (PET) fluoroionophore for the evaluation of its potential application in plants (Figure 38) (Ramachandram and Samanta, 1998; Xiao and Qian, 2003; Mistri *et al*., 2013), based on the following reasons. First, MPNBD displays high fluorescence enhancement in the presence of physiological concentrations of Fe^{3+} with low background emission. Second, chelation of Fe^{3+} by MPNBD induces emission in the green region, which is easily distinguishable from red autofluorescence in plants. In addition, it is efficiently excited by wavelengths above 430 nm, thus avoiding cellular and tissue damage.

MPNBD was synthesized according to a previously described procedure (Xiao and Qian, 2003), and the purity and structural integrity of the synthesized MPNBD were verified by NMR spectra and mass spectrometry (Figures 39-41). To establish proper detection conditions, I investigated the absorption and emission spectra of MPNBD in water and ethanol, along with the various amounts of Fe^{3+}. In ethanol, MPNBD showed a higher fluorescence response to Fe^{3+} in comparison to that observed for MPNBD in water (Figure 42), supporting the relevance of ethanol as the solvent of choice for MPNBD. It is well known that ethanol is compatible with most histological assays on plant tissues. I therefore decided to adopt the ethanol-based detection condition in the assays.

I examined fluorescence responses of MPNBD to various metal ions in ethanol, including Fe^{3+} and Fe^{2+} (Figures 43-47). Notably, treatments with Fe^{3+} and Fe^{2+} induced obvious fluorescence turn-on responses at 533 nm (Figure 43). MPNBD showed different fluorescence responses to $Fe^{3+}$and

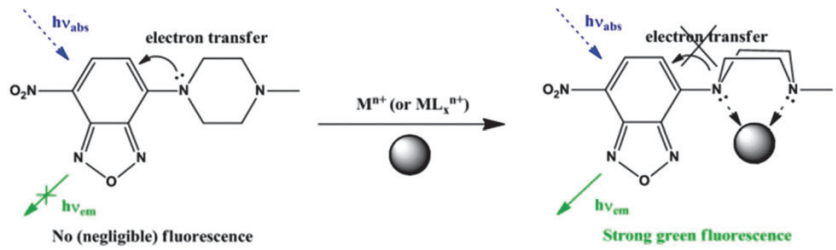

Figure 38. Chemical structure of MPNBD and its photoinduced electron transfer (PET) fluoroionophore mechanism

M, metal ion; n, oxidation number; L, solvent or other ligand molecule.

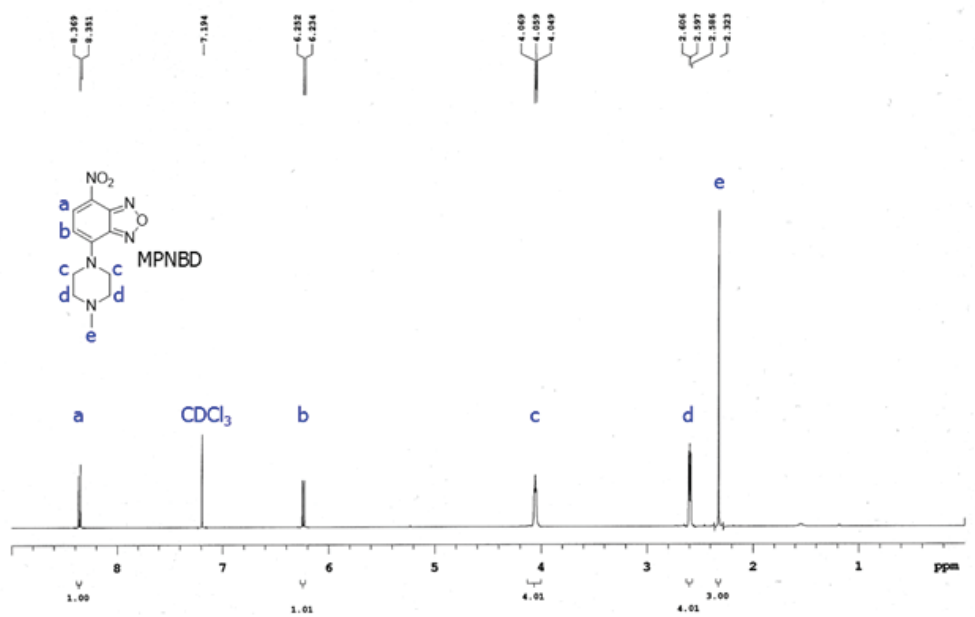

Figure 39. ^{1}H-NMR spectrum of MPNBD

The spectrum were measured by the 500 MHz Varian NMR System (Varian, Palo Alto, CA) in $CDCl_3$, showing appropriate peaks consistent with the previously reported results in Xiao and Qian, 2003. The integrated areas under the signal are reasonably proportional to the number of hydrogen atoms at each position; a : b : c : d : e = 1 : 1 : 4 : 4 : 3.

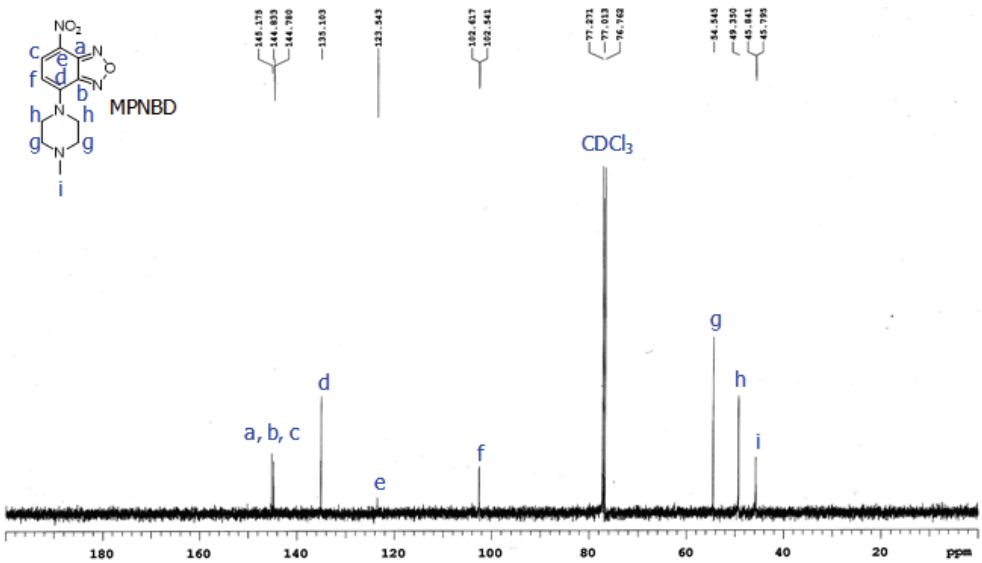

Figure 40. ^{13}C-NMR spectrum of MPNBD

The spectrum were measured by the 500 MHz Varian NMR System in $CDCl_3$, exhibiting appropriate peaks (9 peaks) consistent with the previously reported results in Xiao and Qian, 2003. The numbers at the peaks in the spectra indicate the numbers of different chemical environments where carbon atoms are located in the molecule (designated as a to I in the inset). Note that the peak intensity (or integrated area that is not shown in the spectra) is not simply proportional to the number of carbon atoms that gives rise to the signal because the nuclear overhauser effects from proton decoupling are not equal for all the carbons.

A

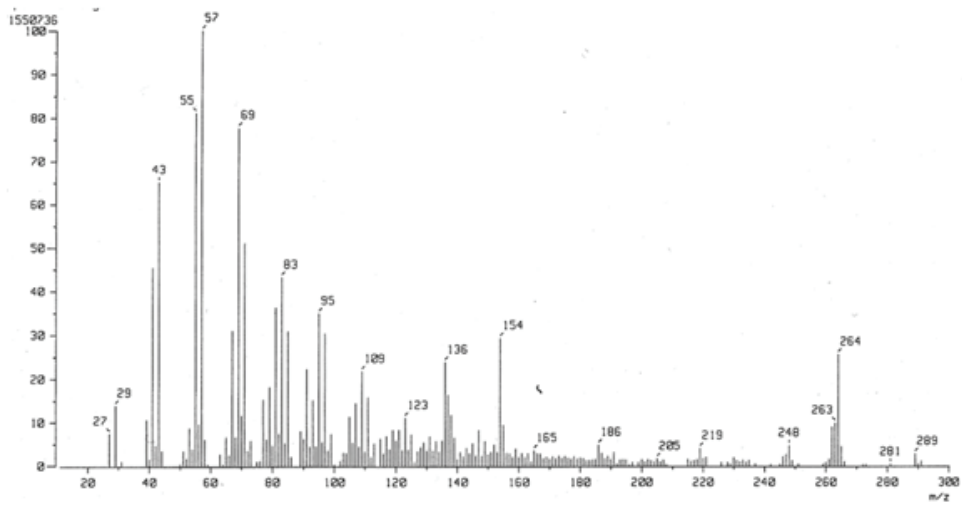

B

Observed m/z	Int%	Err[ppm / mmu]	U.S.	Composition
264.1096	100.0	-10.2 / -2.7	12.0	C 14 H 12 N 6
		-15.3 / -4.0	11.5	C 16 H 14 N 3 O
		+5.0 / +1.3	8.0	C 9 H 12 N 8 O 2
		-0.1 / +0.0	7.5	C 11 H 14 N 5 O 3
		-5.1 / -1.4	7.0	C 13 H 16 N 2 O 4
		+15.2 / +4.0	3.5	C 6 H 14 N 7 O 5
		+10.1 / +2.7	3.0	C 8 H 16 N 4 O 6
		+5.0 / +1.3	2.5	C 10 H 18 N O 7
		-17.2 / -4.5	-1.0	C 2 H 16 N 8 O 7
		+15.2 / +4.0	-2.0	C 7 H 20 O 10

Figure 41. Mass analysis of MPNBD

(**A**) Fast atom bombardment-mass spectrometry (FAB-MS).

(**B**) High resolution-mass spectrum (HR-MS) result of MPNBD. The mass of MBNBD was calculated for C11H14N5O3: 264.1096 and observed: 264.1096 by GC-MS using the JMS-700 MStation (JOEL, Tokyo, Japan).

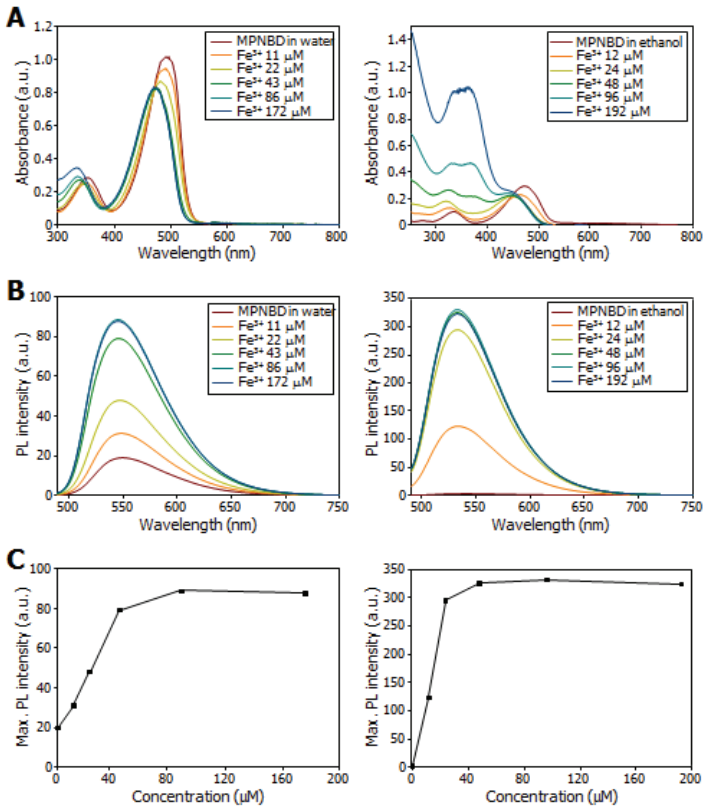

Figure 42. Comparison of fluorescence responses of MPNBD in water (42.2 μM) and ethanol (11.8 μM) to various amounts of Fe^{3+}

(**A**) Changes in absorption spectra of MPNBD upon gradual addition of Fe^{3+} in water (left) and ethanol (right).

(**B**) Changes in fluorescence spectra of MPNBD upon gradual addition of Fe^{3+} in water (left) and ethanol (right) under irradiation at 470 nm.

(**C**) Fluorescence responses of MPNBD to different concentrations of Fe^{3+} in water (left) and ethanol (right). The excitation wavelength was 470 nm and the monitored maximum photoluminescence (PL) emission wavelengths were 548 nm (in water) and 533 nm (in ethanol), respectively, which are clearly shown in (**B**). a.u., arbitrary unit.

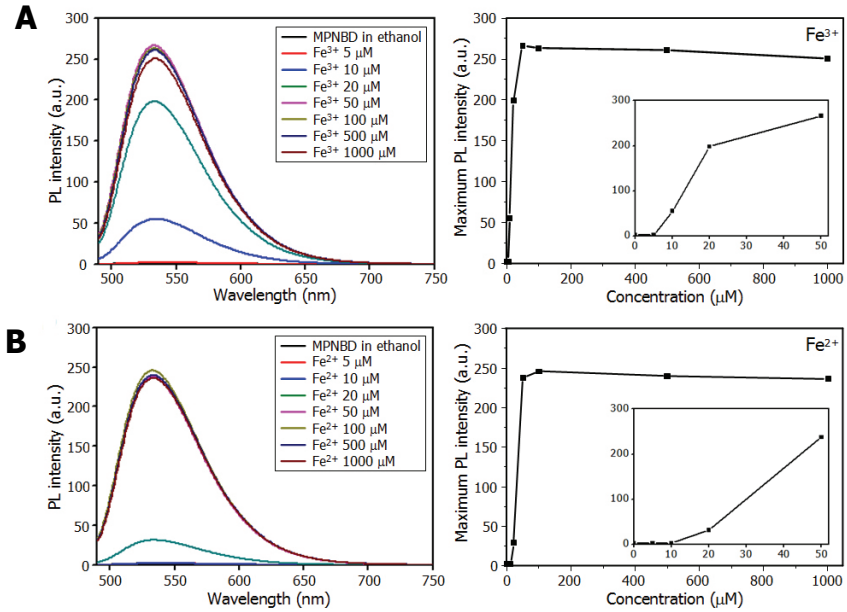

Figure 43. Fluorescence response of MPNBD to Fe^{3+} (A) and Fe^{2+} (B) ions Different concentrations of iron ions were added to MPNBD solution in ethanol, and the mixtures were subject to UV-vis spectroscopy and fluorophotometry. Fluorescence spectra obtained under the irradiation at 470 nm are shown in the left panels. Plots of maximum photoluminescence (PL) emission intensity at 533 nm are shown in the right panels. The insets show plots of maximum PL intensities in the concentration range of 0 to 50 μM for Fe^{3+} or Fe^{2+}. a.u., arbitrary unit.

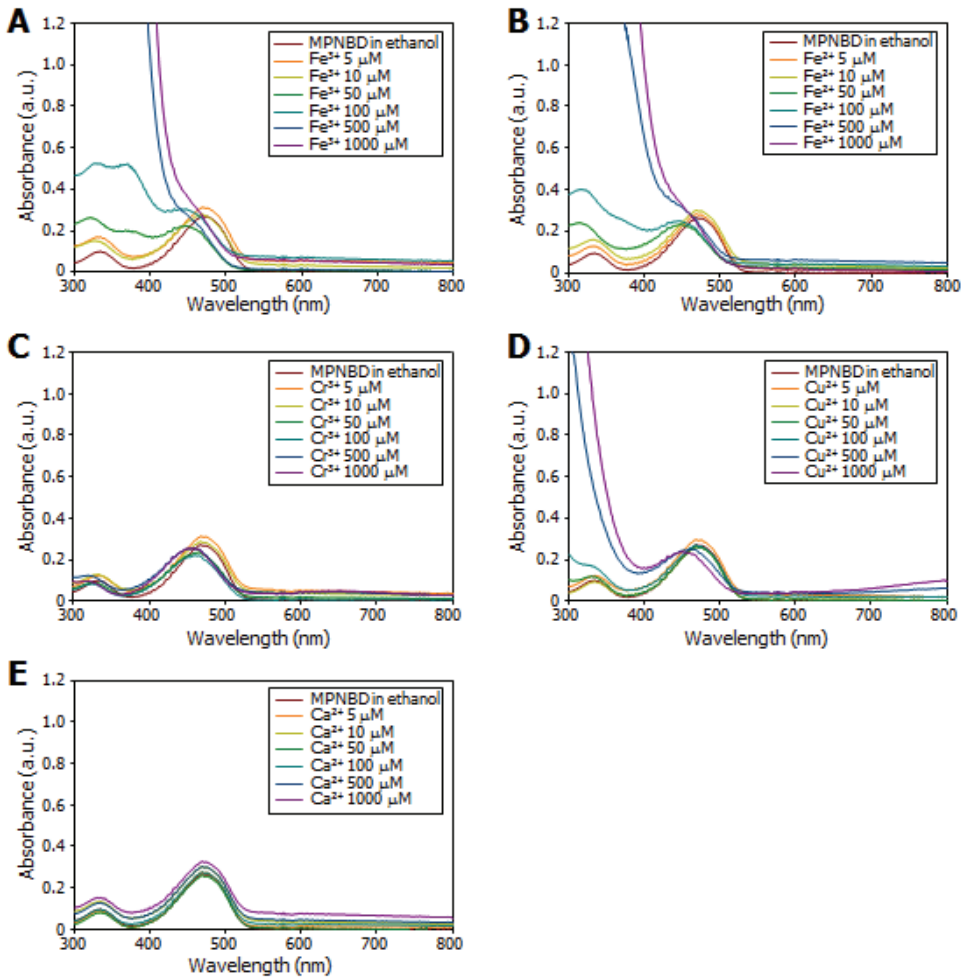

Figure 44. Absorption spectra of MPNBD (9.88 μM) in the presence of Fe^{3+}, Fe^{2+}, Cr^{3+}, Cu^{2+}, and Ca^{2+}

Changes of absorption spectra of MPNBD upon gradual addition (0 to 1000 μM) of Fe^{3+} (**A**), Fe^{2+} (**B**), Cr^{3+} (**C**), Cu^{2+} (**D**), and Ca^{2+} (**E**) in ethanol were examined. a.u., arbitrary unit.

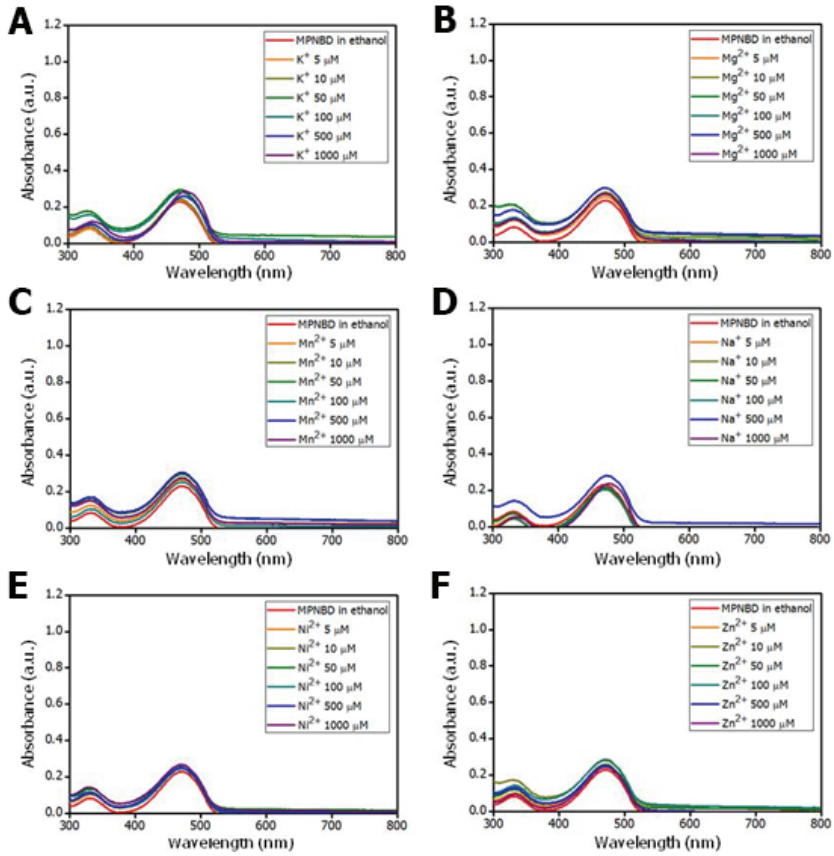

Figure 45. Absorption spectra of MPNBD (9.88 μM) in the presence of K^+, Mg^{2+}, Mn^{2+}, Na^+, Ni^{2+}, and Zn^{2+}

Changes of absorption spectra of MPNBD upon gradual addition (0 to 1000 μM) of K^+ (**A**), Mg^{2+} (**B**), Mn^{2+} (**C**), Na^+ (**D**), Ni^{2+} (**E**), Zn^{2+} (**F**) in ethanol were examined. a.u., arbitrary unit.

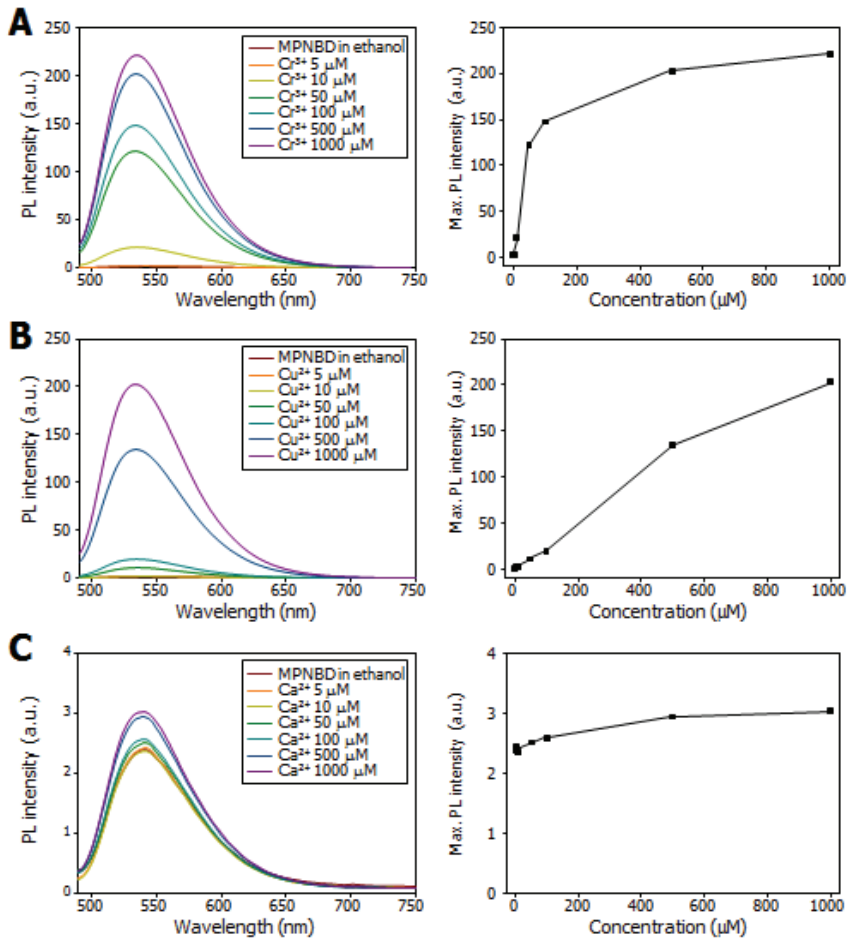

Figure 46. Fluorescence responses of MPNBD to Cr^{3+}, Cu^{2+}, and Ca^{2+}

Changes of fluorescence spectra and maximum emission intensity of MPNBD upon addition (0 to 1000 μM) of Cr^{3+} (**A**), Cu^{2+} (**B**) and Ca^{2+} (**C**) in ethanol were examined. The excitation wavelength was 470 nm and the monitored maximum photoluminescence (PL) emission wavelengths were 534 nm (Cr^{3+}, Cu^{2+}) and 540 nm (Ca^{2+}), respectively. a.u., arbitrary unit.

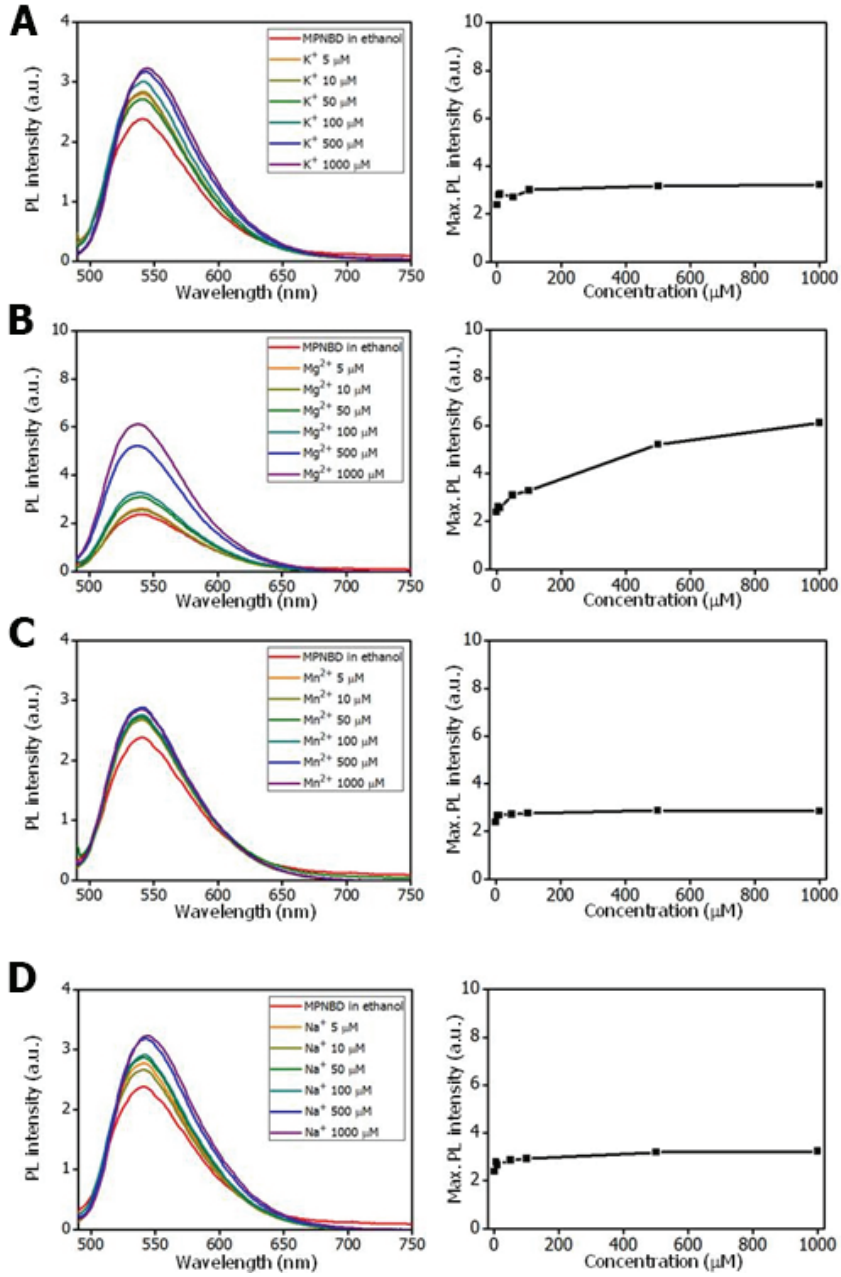
A
MPNBD in ethanol
K+ 5 μM
K+ 10 μM
K+ 50 μM
K+ 100 μM
K+ 500 μM
K+ 1000 μM
PL intensity (a.u.)
Wavelength (nm)
Max. PL intensity (a.u.)
Concentration (μM)
B
MPNBD in ethanol
Mg2+ 5 μM
Mg2+ 10 μM
Mg2+ 50 μM
Mg2+ 100 μM
Mg2+ 500 μM
Mg2+ 1000 μM
PL intensity (a.u.)
Wavelength (nm)
Max. PL intensity (a.u.)
Concentration (μM)
C
MPNBD in ethanol
Mn2+ 5 μM
Mn2+ 10 μM
Mn2+ 50 μM
Mn2+ 100 μM
Mn2+ 500 μM
Mn2+ 1000 μM
PL intensity (a.u.)
Wavelength (nm)
Max. PL intensity (a.u.)
Concentration (μM)
D
MPNBD in ethanol
Na+ 5 μM
Na+ 10 μM
Na+ 50 μM
Na+ 100 μM
Na+ 500 μM
Na+ 1000 μM
PL intensity (a.u.)
Wavelength (nm)
Max. PL intensity (a.u.)
Concentration (μM)

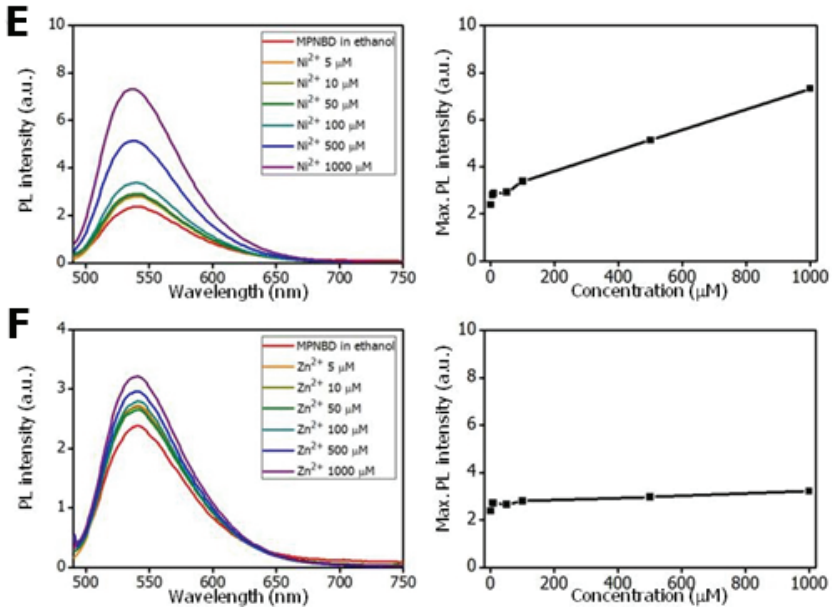

Figure 47. Fluorescence responses of MPNBD to K^+, Mg^{2+}, Mn^{2+}, Na^+, Ni^{2+}, and Zn^{2+}

Changes of fluorescence spectra and maximum emission intensities of MPNBD upon gradual addition (0 to 1000 μM) of K^+ (**A**), Mg^{2+} (**B**), Mn^{2+} (**C**), Na^+ (**D**), Ni^{2+} (**E**), and Zn^{2+} (**F**) in ethanol were examined. The excitation wavelength was 470 nm, and the monitored maximum photoluminescence (PL) emission wavelength was 541 nm. a.u., arbitrary unit.

Fe^{2+}, depending on the concentration of ions. The emission intensity induced by Fe^{3+} was higher by approximately 6-fold than that induced by Fe^{2+} at low concentrations (<50 μM) (see Insets in Figure 43). In contrast, the emission intensities of Fe^{3+} and Fe^{2+} were similar at high concentrations (>50 μM) (Figure 43).

The fluorescence signals enhanced by Fe^{3+} and Fe^{2+} were much higher than those enhanced by other metal ions that are plentiful in plants, such as K^{+}, Ca^{2+} and Mg^{2+} (Figures 46C and 47), suggesting that MPNBD is useful as a fluorescence probe for detection of iron ions in plants. The detection limit of MPNBD for Fe^{3+} was determined to be 8.08 μM (Figure 48), which is much lower than the detection limit of conventional histochemical staining methods.

I found that 50 μM Cr^{3+} elicited approximately half of the emission intensity by iron (Figure 46A). Since the concentration of Cr^{3+} is extremely low in plants, the fluorescence enrichment by Cr^{3+} would essentially be negligible in measuring the fluorescence enrichment of MPNBD by Fe^{3+} and Fe^{2+}. Fifty μM Cu^{2+} induced less than 1% of the emission intensity by iron (Figure 46B). Based on these results together with the relatively low concentration of Cu^{2+} compared to that of iron in plants, I reasoned that endogenous Cu^{2+} does not distort the sensing of iron by MPNBD.

To further evaluate the specific sensing of Fe^{3+} by MPNBD, I performed competition experiments by including other metal ions in the assays. The fluorescence intensities of the mixtures of Fe^{3+} and other metal ions were similar to that by Fe^{3+} alone (Figure 49). It was therefore concluded that the fluorescent turn-on probe MPNBD is suitable for the selective imaging of iron in plant tissues.

I next examined the validity of MPNBD as a fluorescent probe for the imaging of iron distribution in plants using the dicot model *Arabidopsis thaliana*. The *Arabidopsis* seedlings soaked in 50 μM MPNBD solution were

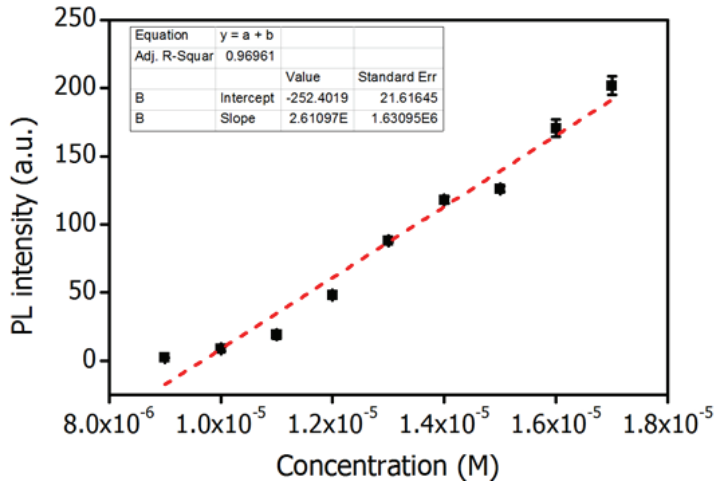

Figure 48. Calibration curve of MPNBD-Fe^{3+} in ethanol solution

The excitation wavelength was 470 nm, and the monitored maximum photoluminescence (PL) emission wavelength was 533 nm. The detection limit (DL) of Fe^{3+} ions using MPNBD was determined from the following equation: $DL = K \times SD/S$, where K=3; SD is the standard deviation of the blank solution; S is the slope of the calibration curve. $DL = K \times SD/S$ = 3 X 0.07032 / 2.61 X 10^{7} = 8.08 X 10^{-6} M. The PL intensity was measured 3 times and averaged. Vertical bars indicate the standard error of the mean.

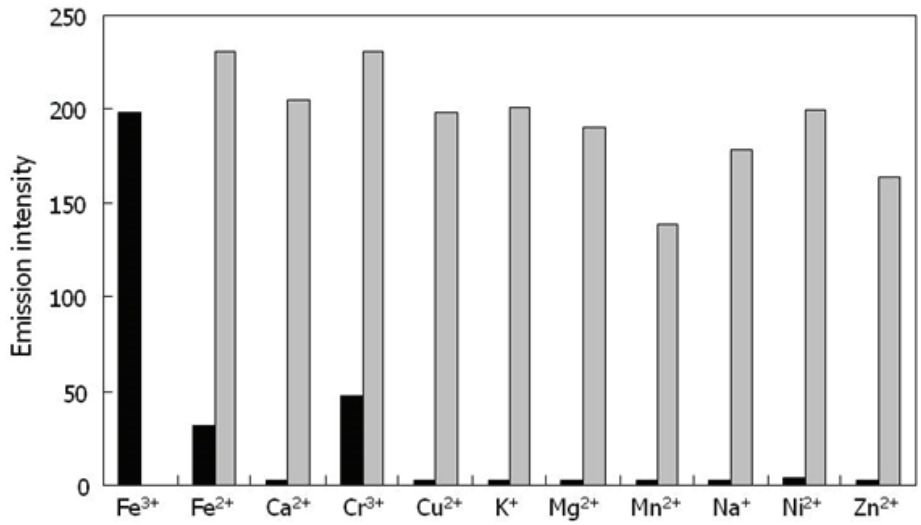

Figure 49. Fluorescence response of MPNBD to various metal ions and to mixtures of $Fe^{3+}$and other metal ions

Fluorescence responses of MPNBD to Fe^{3+}(20 μM) or 20 μM of other metal ions (black bars) and to mixtures of Fe^{3+}(20 μM) and 20 μM of other metal ions (gray bars) in ethanol solution were compared.

subject to vacuum infiltration. The seedlings were then incubated in complete darkness and washed with ethanol before fluorescence microscopy. The Perls and Perls/DAB staining methods were also conducted in parallel for comparative analysis using the *Arabidopsis* seedlings of the same age (Figure 50).

Significantly high fluorescence signals were reproducibly observed in the *Arabidopsis* plants treated with MPNBD (Figure 51). However, no detectable signals were observed in mock-treated plants, indicating that autofluorescence does not interfere with the MPNBD-mediated fluorescence emission in plants. I also found that the MPNBD probe is relatively stable. The fluorescent signals did not significantly diminish even after 3 h (Figure 52). In addition, the presence of other metal ions did not detectably interfere with the sensing of iron by MPNBD *in planta* (Figure 53). I did not include Cr^{3+} in the assays. Although MPNBD showed certain amount of fluorescence response to this metal ion (Figure 46A), its concentration is extremely low in plants.

The Perls staining gave signals primarily in the root tissues. However, it failed to detect discernible signals in the aerial plant parts, as reported previously (Green and Rogers, 2004). The improved Perls/DAB staining produced signals from both the roots and aerial plant parts. However, it suffered from low resolution, as this detection method is based on black precipitates. Notably, the MBNBD-based fluorescence turn-on assays exhibited high fluorescence signals throughout all plant organs, including the leaves, within 20 min following MPNBD treatments (Figure 50).

A prominent feature of the MPNBD-based fluorescence detection method is the high-resolution imaging of iron distribution in plants. It successfully visualized iron distribution in different plant tissues with subcellular resolution (Figure 50, see below). The localized distribution of

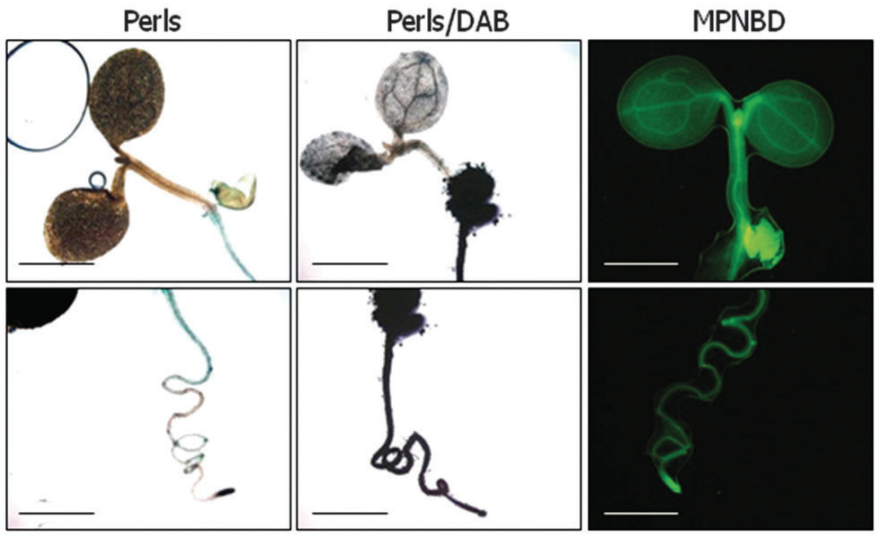

Figure 50. Comparison of different iron detection methods in plants

Four day-old whole *Arabidopsis* seedlings grown on 1/2 X Murashige & Skoog (MS) media containing 0.6% (w/v) agar (hereafter referred to as MS-agar plates) were subject to different iron detection methods as described in Table 4. The aerial plant parts are shown in the top panels, and the roots are shown in the bottom panels. Scale bars, 0.5 cm.

Perls	Perls/DAB	MPNBD
1. Vacuum infiltration for 15 min in 4% HCl/4% $K_4Fe(CN)_6$. 2. Incubation at room temperature for 30 min. 3. Wash with deionized water.	1. Vacuum infiltration for 15 min in 4% HCl/4% $K_4Fe(CN)_6$. 2. Incubation at room temperature for 30 min. 3. Wash with deionized water. 4. Incubation for 1 h in 0.01M NaN_3 / 0.3% H_2O_2 in methanol. 5. Wash with 0.1 M phosphate buffer (pH 7.4). 6. Incubation for 30 min in 0.025% DAB, 0.005% H_2O_2, 0.005% $CoCl_2$ in 0.1M phosphate buffer (pH 7.4). 7. Wash with deionized water.	1. Wash with ethanol. 2. Vacuum infiltration for 5 min in 50 μM MBNBD in ethanol. 3. Incubation at room temperature for 10 min. 4. Wash with ethanol.
~ 1 h	~ 3h	< 20 min
Poor staining in the leaves Low sensitivity (Detection limit : 375 μM)	Moderate sensitivity (Detection limit : 100 μM) Longer time	High resolution High sensitivity (Detection limit : 8.44 μM) Fast and cheap
Roschztterardtz *et al*., 2009	Roschztterardtz *et al*., 2009 Meguro *et al*., 2007	This work

Table 4. Procedures of different iron detection methods in plants.

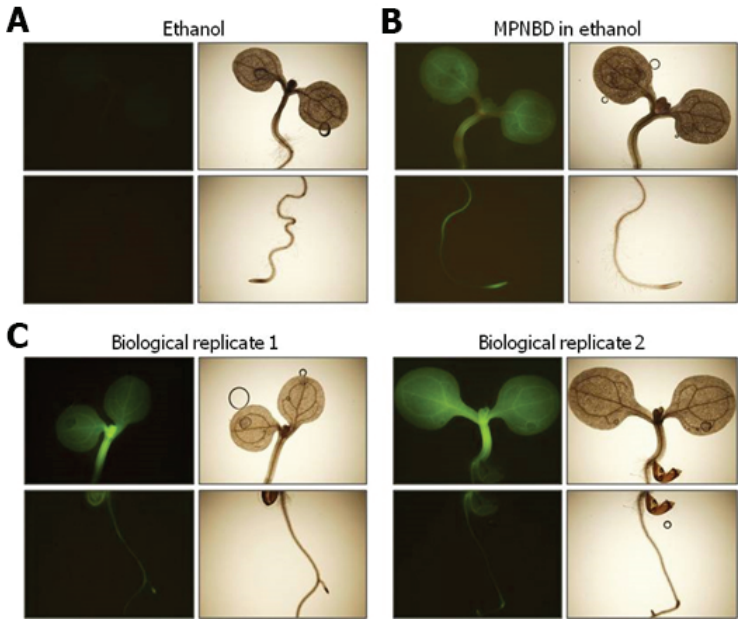

Figure 51. Images of MPNBD-treated plants

Four-day-old whole *Arabidopsis* seedlings grown on MS-agar plates were treated with either ethanol (**A**) or 50 μM MPNBD in ethanol (**B**). The seedlings were visualized by optical and fluorescence microscopy. Fluorescence images are shown in the left panels and optical microscope images are shown in the right panels. Note that no fluorescent signals were detected in the ethanol-treated plants. To evaluate the reproducibility of the MPNBD-mediated fluorescent signals in plants, two additional plants (biological replicates 1 and 2) were treated with MPNBD independently under the identical conditions (**C**).

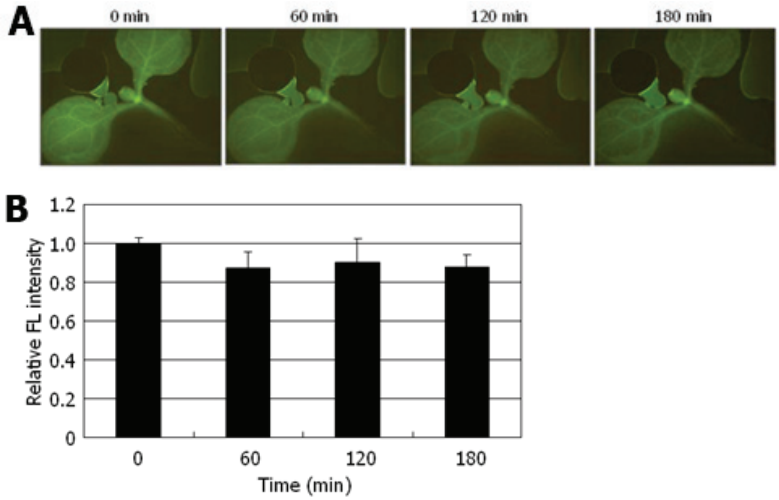

Figure 52. Stability of MPNBD fluorescent probe

Four-day-old whole *Arabidopsis* seedlings grown on MS-agar plates were treated with 50 μM MPNBD in ethanol, as described in **Figure 51**.

(**A**) Fluorescence images obtained at the indicated time points after MPNBD treatments.

(**B**) Quantification of the data in (**A**). The fluorescence (FL) intensity was measured using the ImageJ software (http://rsbweb.nih.gov/ij/), as described previously (Mancuso *et al*., 2006; Hirayama *et al*., 2013). Note that the fluorescent signals do not significantly diminish for up to 3h.

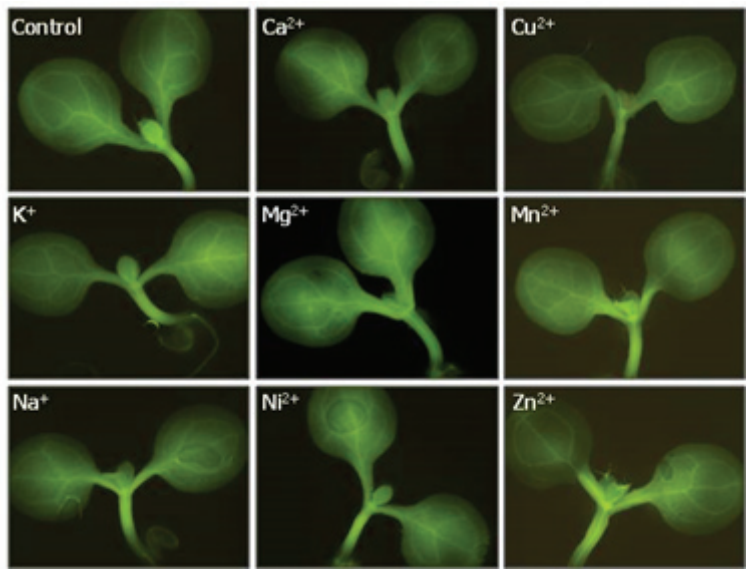

Figure 53. Effects of various metal ions on the MPNBD imaging of iron in plants

Four-day-old whole *Arabidopsis* seedlings grown on MS-agar plates were treated with 500 μM of each metal ion for 12 h and treated with 50 μM MPNBD in ethanol, as described in **Figure 51**. Note that no significant changes in fluorescent signals were detected in the presence of other metal ions.

iron in the leaf tissues is controversial. It has been reported that approximately 70% of the total iron measured in the leaves is found in the chloroplasts (Shikanai *et al*., 2003). On the other hand, a considerable amount of iron has also been detected in the vasculature of the leaves (Stacey *et al*., 2008). The MPNBD fluorescence method visualized high-resolution signals in both the chloroplasts and vasculature of the leaves (Figures 54A and 50, respectively), demonstrating that iron accumulates in both the chloroplasts and vasculature of the leaves. There was also high-level fluorescence emission in the vasculature of the stems and roots after MPNBD treatments (Figures 54B-D). Moreover, the MPNBD-assisted high-resolution imaging revealed that iron accumulates at a high level in the epidermal cells of the seed coat (Figure 54E), especially in the volcano-shaped columella and hexagonal cell wall (Figure 54F). It has been reported that Ca^{2+} is deposited in a similar pattern in the seed coat (Voiniciuc *et al*., 2013). I therefore suspected that the fluorescence emission might be from MPNBD-Ca^{2+} complex. However, the fluorescence enrichment of MPNBD by Ca^{2+} was beyond the detection limit of this assay conditions (Figure 46C), indicating that fluorescence emission in the seed coat was due to iron deposits. Nonetheless, the biological function of iron deposited in the seed coat is currently unknown.

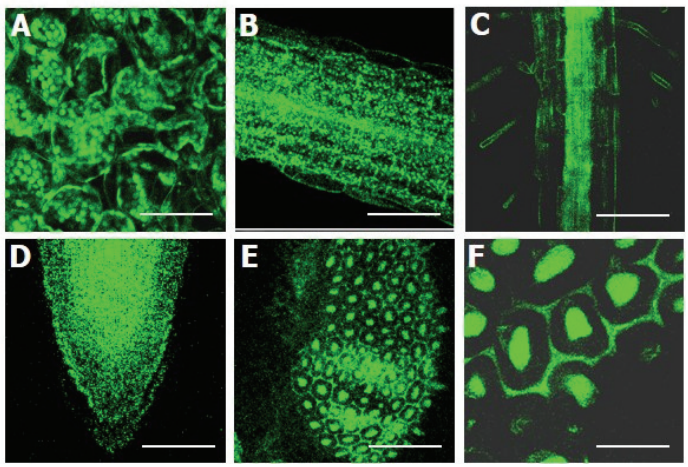

Figure 54. Fluorescence images of plants treated with MPNBD

Four-day-old, whole *Arabidopsis* seedlings grown on MS-agar plates were treated with 50 μM MPNBD and visualized by fluorescence microscopy.

(**A**) Fluorescence image of leaf epidermal cells. Scale bar, 60 μm.

(**B**) Fluorescence image of the stem. Scale bar, 120 μm.

(**C** and **D**) Fluorescence image of the root stem (**C**) and the root tip region (**D**). Scale bars, 110 μm (**C**) and 60 μm (**D**).

(**E** and **F**) Fluorescence images of developing seeds. *Arabidopsis* seeds were cold-imbibed for 3 days in complete darkness and allowed to germinate for 12 hours before MPNBD treatments. An enlarged view (**F**) of the developing seed (**E**) is shown. Scale bars, 110 μm (**E**) and 40 μm (**F**).

DISCUSSION

The data demonstrate that the fluorescence turn-on probe MPNBD is able to image the distribution of total iron in all plant tissues with high resolution and high sensitivity (Table 4). In addition, the MPNBD-assisted fluorescence detection method can be readily applied to all plant organs with a simple procedure and low cost. Furthermore, due to the high binding affinity of MPNBD to iron, it is unnecessary to treat plant samples with acids to release iron from iron complexes prior to MPNBD treatment. Since the MPNBD method is based on fluorescence emission, sectioning of plants tissues is not necessary for small plants, such as *Arabidopsis*.

In conclusion, the MPNBD fluorescence method provides high-resolution imaging of total iron in plant tissues. Therefore, dynamic information on the redox chemistry of iron can be obtained if it is applied in conjunction with Fe^{3+}- and Fe^{2+}-specific fluorescent probes. This method is potentially useful for the isolation of mutant plants that are defective in iron metabolism and deposit in a high-throughput manner.

CHAPTER 4

Self-directed control of the diurnal CONSTANS dynamics in *Arabidopsis* photoperiodic flowering

ABSTRACT

The circadian clock control of *CONSTANS* (*CO*) transcription and the light regulation of CO stability coordinately regulate photoperiodic flowering by triggering rhythmic expression of the floral integrator *FLOWERING LOCUS T* (*FT*). The diurnal pattern of CO accumulation is modulated sequentially by distinct E3 ubiquitin ligases, such as HIGH EXPRESSION OF OSMOTICALLY RESPONSIVE GENES 1 (HOS1) in the morning, FLAVIN-BINDING, KELCH REPEAT, F-BOX 1 (FKF1) in late afternoon, and CONSTITUTIVE PHOTOMORPHOGENIC 1 (COP1) at night. In particular, CO is stabilized by FKF1 in late afternoon only under long days. Here, I show that CO abundance is not simply regulated by the E3 enzymes in a passive manner but also self-regulated actively through dynamic interactions between two CO isoforms. CO alternative splicing produces two protein variants, the full-size COα and the C-terminally truncated COβ. Notably, COβ, which is resistant to the E3 enzymes, induces the interactions of COα with CO-destabilizing HOS1 and COP1 but inhibits the association of COα with CO-stabilizing FKF1. These observations demonstrate that CO plays an active role in sustaining its diurnal accumulation dynamics in *Arabidopsis* photoperiodic flowering.

INTRODUCTION

Plants precisely regulate flowering time by integrating developmental and environmental signals into the flowering genetic pathways to achieve reproductive success. Seasonal changes in day length or photoperiod are one of the major environmental factors that affect flowering time (Kobayashi and Weigel, 2007; Amasino, 2010). In *Arabidopsis*, CONSTANS (CO) transcription factor plays a key role in photoperiodic flowering by triggering rhythmic expression of the floral integrator *FLOWERING LOCUS T* (*FT*) (Corbesier *et al*., 2007; Andrés and Coupland, 2012; Song and Imaizumi, 2013). The CO function is modulated through diverse molecular mechanisms, such as transcriptional control by the circadian clock (Suárez-López *et al*., 2001), regulation of CO stability by ubiquitin/proteasome-dependent degradation (Valverde *et al*., 2004), and interactions with other regulatory factors (Wenkel *et al*., 2006; Song *et al*., 2012a; Endo *et al*., 2013). Among these, the distinct pattern of diurnal CO accumulation, which peaks in late afternoon, is critical for flowering induction under long days (LDs) (Valverde *et al*., 2004).

The CO stability is modulated by a group of E3 ubiquitin ligases. HIGH EXPRESSION OF OSMOTICALLY RESPONSIVE GENES 1 (HOS1) degrades CO in the early morning (Lazaro *et al*., 2012), and CONSTITUTIVE PHOTOMORPHOGENIC 1 (COP1) directs CO degradation at night (Jang *et al*., 2008; Liu *et al*., 2008). Notably, FLAVIN-BINDING, KELCH REPEAT, F-BOX 1 (FKF1) works synergistically with blue light signals in the late afternoon to stabilize CO under LDs (Song *et al*., 2012b). Despite recent advances in our understanding of molecular mechanisms underlying the diurnal CO accumulation, it is currently unknown whether CO plays a self-regulatory role in the diurnal CO dynamics.

It is known that the susceptibility of proteins to ubiquitin-mediated

protein degradation is influenced by their interactions with other proteins in plants and animals. For instance, the interaction between LONG AFTER FAR-RED LIGHT 1 and LONG HYPOCOTYL IN FAR-RED 1, which are positive regulators of phytochrome A signaling in *Arabidopsis*, stabilizes each other by inhibiting COP1-mediated polyubiquitination (Jang *et al*., 2007). The zinc finger protein Miz1 protects the oncoprotein Myc from the HectH9 E3 ligase-mediated ubiquitination in human cells (Adhikary *et al*., 2005). In addition, the dimeric form of CYTOPLASMIC POLYADENYLATION ELEMENT-BINDING PROTEIN is more rapidly degraded than its monomeric form because of the higher affinity of the dimeric form for β-TRANSDUCIN REPEAT-CONTAINING PROTEIN, a F-box protein of E3 ligase complex (Lin *et al*., 2012). Conversely, homodimer of the neuronal NITRIC-OXIDE SYNTHASE is more resistant to ubiquitination-mediated proteolysis compared to its monomeric form (Bender *et al*., 2000; Dunbar *et al*., 2004).

Recently, alternative splicing and dynamic interactions between the protein isoforms have emerged as a novel mechanism that regulates transcription factor activity in *Arabidopsis* (Seo *et al*., 2011; James *et al*., 2012; Seo *et al*., 2012b; Steiger and Brown, 2013). CIRCADIAN CLOCK ASSOCIATED 1 (CCA1), a core clock component, undergoes alternative splicing, producing two protein variants, CCA1α and CCA1β (Seo *et al*., 2012b; James *et al*., 2012). Inhibition of the CCA1α activity by the non-DNA binding CCA1β mediates the physiological link between the clock function and freezing tolerance (Seo *et al*., 2012b). An alternatively spliced INDETERMINATE DOMAIN 14 (IDD14) variant, IDD14β, also negatively regulates the DNA binding of IDD14α by forming heterodimers (Seo *et al*., 2011).

Here, I demonstrated that CO undergoes alternative splicing, producing the full-size COα, which is equivalent to the well-known CO

protein, and the C-terminally truncated COβ. COα and COβ form homo- and hetero-dimers in the nucleus. COβ inhibits COα function by forming heterodimers in photoperiodic flowering. Notably, COβ is resistant to ubiquitin/proteasome-dependent degradation and, most importantly, facilitates COα degradation by enhancing the interaction of COα with CO-destabilizing HOS1 and COP1 but reducing the interaction of COα with CO-stabilizing FKF1. I propose that the diurnal CO dynamics is not simply regulated by E3 enzymes in a passive manner but also self-regulated in an active manner through dynamic interactions between the two CO isoforms.

MATERIALS AND METHODS

Plant materials and growth conditions

All *Arabidopsis thaliana* lines used were in Columbia (Col-0) background. Plants were grown in soil or on ½ X Murashige and Skoog (MS)-agar plates (hereafter referred to as MS-agar plates) at 23°C under either long day (LD, 16-h light and 8-h dark) or short day (SD, 8-h light and 16-h dark) conditions. White light illumination at light intensity of 120 μmol photons $m^{-2}s^{-1}$ was provided by fluorescent FLR40D/A tubes (Osram, Seoul, Korea).

To generate transgenic plants overproducing COβ, a full-size *COβ* cDNA was subcloned under the control of the cauliflower mosaic virus (CaMV) 35S promoter into the binary pK7WG2D vector (Invitrogen, Carlsbad, CA), and the vector constructs were transformed into Col-0 plants, resulting in 35S:*COβ*. A MYC-coding sequence was fused in-frame to the 5' end of a full-size *COα* cDNA or to the 3' end of a full-size *COβ* cDNA, and the fusions were subcloned under the control of the CaMV 35S promoter into the binary pK7WG2D vector (Invitrogen). The vector constructs were transformed into Col-0 plants, resulting in 35S:*MYC-COα* and 35S:*COβ-MYC*, respectively. To generate transgenic plants expressing COβ under the control of a β-estradiol-inducible promoter, a full-size *COβ* cDNA was subcloned into the pER8 vector (Zuo *et al*., 2000).

Agrobacterium tumefaciens-mediated transformation of *Arabidopsis* plants was conducted according to a modified floral dip method (Clough and Bent, 1998).

Gene expression analysis

Quantitative real-time RT-PCR (qRT-PCR) was employed to examine the levels of gene transcripts. Extraction of total RNA, reverse transcription, and

quantitative polymerase chain reaction were performed following the optimization rules that have been proposed to ensure accurate and reproducible measurements (Udvardi *et al*., 2008).

qRT-PCR reactions were routinely performed in 96-well blocks with an Applied Biosystems 7500 Real-Time PCR System (Foster City, CA) using the SYBR Green I master mix in a volume of 20 μl. PCR primers were designed using the Primer Express Software installed in the system and listed in Table 5. The two-step thermal cycling profile employed was 15 s at 95^{o}C for denaturation and 1 min at 60-65^{o}C, depending on the calculated melting temperatures of PCR primers, for annealing and polymerization. An *eIF4A* gene (At3g13920) was included as internal control in each PCR reaction to normalize the variations in the amounts of cDNA used.

All qRT-PCR reactions were performed in biological triplicates using total RNA samples extracted separately from three independent plant materials that were grown under identical experimental conditions. The comparative $\Delta\Delta C_T$ method was employed to evaluate relative quantities of each product amplified from the samples. The threshold cycle (C_T) was automatically determined for each reaction by using the default parameters of the system.

Absolute quantification of gene transcripts

Absolute quantification of gene transcripts was performed as described previously (Kwon *et al*., 2014). Gene-specific sequences were subcloned into the pGADT7 vector (Clontech, Mountain View, CA), and an absolute standard curve of each transcript was obtained by a series of 10-fold dilutions covering from 10^{-19} to 10^{-22} mol/μl, as described previously (Bustin, 2000; Whelan *et al*., 2003; Kwon *et al*., 2014). Quantitative RT-PCR was performed using the SYBR GreenI master mix with gene-specific primers listed in Table 5.

Flowering time measurement

Plants were grown in soil at 23°C under LDs until flowering. Flowering time was measured by counting the number of rosette leaves at the time of a 1-cm-high flower bolt. Approximately 20-30 plants were counted and averaged for each measurement.

Transcriptional activation activity assay

For transient expression assay using *Arabidopsis* mesophyll protoplasts, a series of reporter and effector vectors was constructed. The reporter plasmid contains 4 copies of the GAL4 upstream activation sequence (UAS) and the β-glucuronidase (*GUS*) gene. To construct the effector plasmids, full-size *COα* and *COβ* cDNAs were fused to the GAL4 DNA-binding domain (BD)-coding sequence, and the fusion was subcloned into an expression vector containing the CaMV 35S promoter. The reporter and effector vectors were cotransformed into *Arabidopsis* protoplasts by the polyethylene glycol (PEG)-mediated transformation method (Yoo *et al*., 2007). GUS activity was measured by the fluorometric method as described previously (Jefferson *et al*., 1987). A CaMV 35S promoter-luciferase (LUC) construct was also cotransformed as internal control, and LUC assays were performed using the Luciferase Assay System kit (Promega, Madison, WI).

Yeast two-hybrid assay

Yeast two hybrid assays were performed using the BD Matchmaker system (Clontech). The pGADT7 vector was used for GAL4 activation domain (AD), and the pGBKT7 vector was used for GAL4 BD. Yeast strain AH109 (Leu-, Trp-, Ade-, His-), which harbors chromosomally integrated reporter genes *lacZ* and *HIS* under the control of the GAL1 promoter, was used for transformation. Full-size *COα* and *COβ* cDNAs were subcloned into the pGADT7 and pGBKT7 vectors. Transformation of AH109 cells was

performed according to the manufacturer's procedure. Colonies obtained were restreaked on medium lacking Leu, Trp, His, and Ade. To confirm the results on cell growth on selective media, β-Gal assays were also performed according to the system procedure.

Yeast three-hybrid assay

The pBridge vector (Clontech) harboring genes encoding the bait-BD fusion and the third protein (bait mate), and the pGATD7 vector (Clontech) harboring a gene encoding the prey-AD fusion were used for yeast three-hybrid assays, as described previously (Liu *et al*., 2011). Full-size *COα*, *HAP5a*, *HOS1*, and *COP1* cDNAs were subcloned into the pBridge vector, resulting in a series of BD fusion constructs. A full-size *COβ* cDNA was subcloned into the *Not*I and *Bgl*II-digested pBridge vector so that its expression was driven by the methionine (Met)-repressible pMET25 promoter. The expression constructs were cotransformed into yeast AH109 cells. Colonies were restreaked on media lacking Leu, Trp, and His and supplemented with or without Met. To confirm the results on cell growth on selective media, β-Gal assays were also performed according to the manufacturer's procedure.

***In vivo* ubiquitination assay**

For *in vivo* detection of ubiquitinated CO proteins, 35S:*MYC-COα* transgenic plants expressing a full-size *COβ* cDNA under the control of a β-estradiol-inducible promoter were grown for 10 d on MS-agar plates under LDs and then treated with 100 μM β-estradiol and/or 50 μM MG132 for 12 h under constant light. Approximately 30 seedlings were ground in liquid nitrogen and resuspended in extraction buffer (50 mM Tris, pH 7.5, 150 mM sodium chloride, 1% Trion X-100, 1 mM EDTA, 10% glycerol, 0.5 mM PMSF) supplemented with protease inhibitor cocktail (Sigma-Aldrich, St.

Louis, MO). The crude extracts were then incubated with an anti-MYC antibody conjugated to agarose beads (Sigma) for 12 h at 4°C. The beads were recovered by brief centrifugation and washed five times, each with 1 ml of fresh extraction buffer. The bound proteins were eluted with 1 X SDS-PAGE loading buffer by boiling for 5 min and subjected to SDS-PAGE. Immunological detection of CO proteins was performed using anti-MYC (Millipore, Billerica, MA) and anti-ubiquitin (Santa Cruz Biotechnology, Santa Cruz, CA) antibodies.

***In vitro* pull-down assay**

A full-size *COβ* cDNA was subcloned into the pMAL-c2X *Escherichia coli* expression vector containing a maltose binding protein (MBP)-coding sequence (New England Biolabs, Ipswich,MA). Recombinant MBP and MBP-COβ proteins were produced in *E. coli* Rosetta2 (DE3) pLysS strain (Novagen, Madison, WI). Protein synthesis was induced by adding 0.2 mM isopropyl-1-thio-β-D-galactopyranoside at 20°C overnight. Cells were harvested and resuspended in MBP buffer (20 mM Tris, pH 7.4, 200 mM sodium chloride, 1 mM EDTA, 10 mM 2-mercaptoethanol, 1 mM PMSF) supplemented with protease inhibitor cocktail (Sigma-Aldrich). Cell lysates were prepared by three cycles of freezing and thawing followed by centrifugation at 30,000 X g for 30 min. The supernatants containing soluble MBP or MBP-COβ proteins were stored at -80°C until use. The pGADT7-COα construct, which harbors the T7 RNA polymerase promoter upstream of multiple cloning sequence, was used to produce ^{35}S-labeled COα polypeptide by *in vitro* translation using the T_NT-coupled reticulocyte lysate system (Promega).

The ^{35}S-labeled COα polypeptides were incubated with 1 μg of MBP or MBP-COβ protein bound to amylose resin (New England Biolabs) in 1 ml of binding buffer (50 mM Tris, pH 8.0, 100 mM sodium chloride,

10% glycerol, 1% triton X-100, 1 mM PMSF) supplemented with protease inhibitor cocktail (Sigma-Aldrich) and 5% skim milk for 12 h at 4°C. The beads were washed five times with washing buffer (25 mM Tris, pH 8.0, 100 mM sodium chloride). Bound proteins were eluted with 1 X SDS-PAGE loading buffer by boiling for 10 min and subjected to SDS-PAGE and autoradiography.

Bimolecular fluorescence complementation (BiFC) assay

BiFC assays were conducted as described previously (Seo *et al*., 2012b). Full-size *COα* and *COβ* cDNAs were fused in-frame to the 3' end of a gene sequence encoding the N-terminal half of enhanced YFP in the pSATN-nEYFP-C1 vector (E3081) or to the 3' end of a gene sequence encoding the C-terminal half of enhanced YFP in the pSATN-cEYFP-C1 vector (E3082). The expression constructs were cotransformed into *Arabidopsis* mesophyll protoplasts by the PEG-calcium transfection method (Yoo *et al*., 2007). Transformed protoplasts were incubated for 16 h under constant light, and reconstitution of YFP fluorescence was monitored by fluorescence microscopy using a Zeiss LSM510 confocal microscope (Carl Zeiss, Jena, Germany) with the following filter setup: 514 nm for excitation, 535-590 nm for YFP, 690-730 nm for autofluorescence.

Protein stability assay

To examine the protein stability of COα in the presence of COβ, 35S:*MYC-COα* transgenic plants expressing *COβ* under the control of a β-estradiol-inducible promoter were grown for 10 d on MS-agar plates under LDs and transferred to MS liquid culture supplemented with various concentrations of β-estradiol and MG132 in the light for 12 h. Whole plants were harvested for the extraction of total proteins. COα proteins were detected immunologically using an anti-MYC antibody (Millipore).

To study the effects of COβ on the protein stability of COα in the dark, the plants described above were examined as described previously (Jang *et al*., 2005). Ten-day-old plants were preincubated in MS liquid culture supplemented with 50 μM MG132 alone or 100 μM β-estradiol and 50 μM MG132 for 12 h in the light. Plants were washed three times with fresh MS liquid culture and then transferred to MS liquid culture supplemented with 1 mM cycloheximide. The plants were then incubated in the dark for up to 120 min, and whole plants were harvested for the extraction of total proteins. COα proteins were detected immunologically using an anti-MYC antibody (Millipore).

Primers	Usage	Sequences
eIF4a-F	qRT-PCR	5′-TGACCACACAGTCTCTGCAA
eIF4a-R	qRT-PCR	5′-ACCAGGGAGACTTGTTGGAC
CO-F	qRT-PCR	5′-ACGCCATCAGCGAGTTCC
COα-R	qRT-PCR	5′-AAATGTATGCGTTATGGTTAATGG
COβ-R	qRT-PCR	5′-TGCTGCGTTATGGGAAGATG
FT-F	qRT-PCR	5′-GGTGGAGAAGACCTCAGGAA
FT-R	qRT-PCR	5′-ATTGTAGAAAACTGCGGCCA
CO-F1	RT-PCR	5′-ATGTTGAAACAAGAGAGTAACGAC
CO-F2	RT-PCR	5′-CATAACGCAGCAGGGTGA
CO-R	RT-PCR	5′-TCAGAATGAAGGAACAATCCC
CO-5′UTR-F	RT-PCR	5′-ATTAGCCCCTTCTTTCAGATACCAG
CO-3′UTR-R	RT-PCR	5′-GAAAGAAGAATACTATAGTTTTAATTAGCCAAAAC
TUB-F	RT-PCR	5′-CTCAAGAGGTTCTCAGCAGTA
TUB-R	RT-PCR	5′-TCACCTTCTTCATCCGCAGTT
CO-YFP-F	BiFC	5′-ATGTCGACATGTTGAAACAAGAGAGTAACGACATAG
COα-YFP-R	BiFC	5′-ATGGATCCTCAGAATGAAGGAACAATCCCA
COβ-YFP-R	BiFC	5′-ATGGATCCTCACCCTGCTGCGTTATGG
CO-yeast-F	Y2H/Y3H	5′-CCGAATTCATGTTGAAACAAGAGAGTAACGAC
COα-yeast-R	Y2H/Y3H	5′-TTGGATCCTCAGAATGAAGGAACAATCCC
COβ-yeast-R	Y2H/Y3H	5′-TTGGATCCTCACCCTGCTGCGTTATG
COβ-Y3H-F	Y3H	5′-ATAAGAATGCGGCCGCAATGTTGAAACAAGAGAG
COβ-Y3H-R	Y3H	5′-GGAAGATCTTCACCCTGCTGCGTTATG
HAP5a-F	Y3H	5′-GGGAATTCATGGATACCAACAACCAGCAAC
HAP5a-R	Y3H	5′-GGGTCGACTTAACCTTGGCCGTCGAGATTC
HOS1-F	Y3H	5′-ATACCATGGAGATGGATACGAGAGAAATCAACG
HOS1-R	Y3H	5′-TACCCGGGTCATCTTGCTGCGAATCTACG
COP1-F	Y3H	5′-GCGAATTCATGGAAGAGATTTCGACGGATC
COP1-R	Y3H	5′-GCGTCGACTCACGCAGCGAGTACCAGAAC
FKF1-F	Y3H	5′-GGAATTCCATATGATGGCGAGAGAACATGCGAT
FKF1-R	Y3H	5′-GGAATTCCATATGTTACAGATCCGAGTCTTGCCG
MYC-COα-F	cloning	5′-GCTGGCGCGCCATCAAACTTACTACATCTGAGTT
MYC-COα-R	cloning	5′-CAGGACGTCCAGAATGAAGGAACAATCCCATATC
COβ-MYC-F	cloning	5′-ATGGCGCGCCATGTTGAAACAAGAGAGTAACGACATAG
COβ-MYC-R	cloning	5′-ATGACGTCTGCCCTGCTGCGTTATGGGA
35S:COβ-F	cloning	5′-AAAAAGCAGGCTCTATGTTGAAACAAGAGAGTAACGAC
35S:COβ-R	cloning	5′-AGAAAGCTGGGTTTCACCCTGCTGCGTTATG
COβ-ER8-F	cloning	5′-TTGGCGCGCCATGTTGAAACAAGAGAGTAACGAC
COβ-ER8-R	cloning	5′-GGACTAGTTCACCCTGCTGCGTTATG

Table 5. Primers used in the study.

The primers were designed according to the Primer3 software (version 0.4.0, http://primer3.sourceforge.net/releases.php) in a way that they have calculated melting temperatures in a range of 50-65^{o}C. F and R, forward and reverse, respectively. Y2H, yeast two-hybrid assay; Y3H, yeast three-hybrid assay; BiFC, bimolecular fluorescence complementation assay.

RESULTS

CO alternative splicing and interactions between two CO isoforms

I identified two CO variants in The *Arabidopsis* Information Resource (TAIR) database, suggesting that *CO* undergoes alternative splicing. Recent studies have shown that dynamic interactions between alternatively spliced protein isoforms constitute a self-regulatory circuit in diverse physiological functions (Seo *et al*., 2011; Seo *et al*., 2012b). I therefore investigated whether *CO* alternative splicing is important for CO function during photoperiodic flowering.

I first examined whether *CO* undergoes alternative splicing. RT-PCR analysis using exon- and intron-specific primer sets detected two transcripts, designated *COα* and *COβ* (Figures 55A, 55B and 56). DNA sequencing revealed that *COβ* contained an intron that was absent in *COα* (Figure 57), suggesting that *CO* alternative splicing is mediated by intron retention, which is the most common type of alternative splicing in plants (Tiwari *et al*., 2010). The predicted COα contains two copies of B-box-type zinc finger (ZF) domains in the N-terminal region and the C-terminal CO, CO-LIKE, TOC1 (CCT) domain (Figures 55C and 58), which mediates DNA binding and protein-protein interactions (Laubinger *et al*., 2006; Wenkel *et al*., 2006; Tiwari *et al*., 2011). It is equivalent to the well-characterized CO protein (Figure 55C and 58). In contrast, the predicted COβ lacks the CCT domain.

RNA splice variants harboring premature termination codons are either translated into distinct proteins, i.e., productive, or they are degraded by nonsense-mediated decay (NMD) pathways (Kalyna *et al*., 2012) and considered unproductive. The level of *COβ* transcripts was unchanged in plants treated with cycloheximide (CHX), a potent inhibitor of NMD (Hori and Watanabe, 2005) (Figure 59). It was also unaffected in *upf1-5* and *upf3-1* mutants defective in NMD (Hori and Watanabe, 2005; Arciga-Reyes

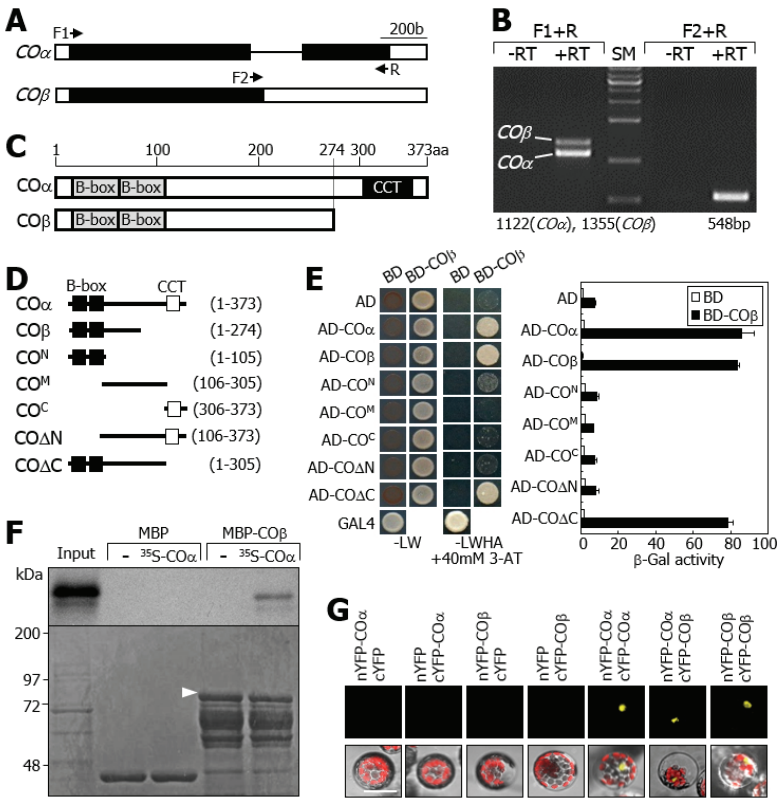

Figure 55. CO alternative splicing and isoform interactions

(**A**) Genomic structure and RNA splice variants of *CO*. Black boxes, exons; white boxes, untranslated regions. F and R, forward and reverse primers, respectively. b, base.

(**B**) Detection of RNA splice variants by RT-PCR. RT, reverse transcription. SM, size marker. bp, base pair.

(**C**) Domain structure of CO isoforms. aa, amino acid.

(**D** and **E**) Yeast two-hybrid. Serial deletions of CO were used to examine interactions between COα and COβ (**D**). COα-COβ interactions were examined by cell growth on selective media lacking Leu (L), Trp (W), His (H), and Ade (A) and by β-Gal assays (**E**, left and right panels, respectively). Bars indicate standard error of the mean (SE) of three

measurements.

(**F**) *In vitro* pull-down assay. Recombinant MBP-COβ and *in vitro* translated, ^{35}S-labeled COα polypeptide were used. Arrowhead, MBP-COβ. kDa, kilodalton.

(**G**) BiFC analysis. CO dimer formation in *Arabidopsis* protoplasts was visualized by differential interference contrast (DIC) and fluorescence microscopy. Scale bar, 20 μm.

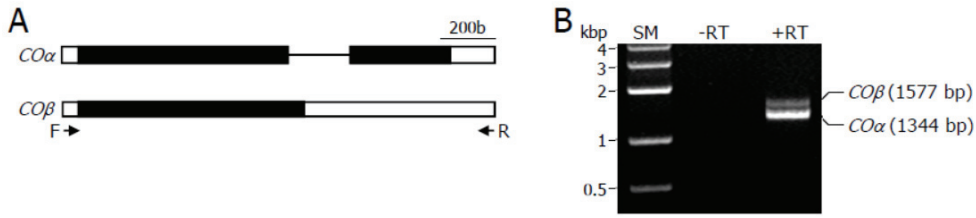

Figure 56. Alternatively spliced RNA variants of *CO* gene

(**A**) Genomic structure of *CO*. The *CO* gene consists of 2 exons and 1 intron. Black and white boxes indicate exons and untranslated regions, respectively. F and R are forward and reverse primers, respectively. b, base. (**B**) Detection of alternatively spliced RNA variants. A cDNA pool prepared from ten-day-old Col-0 plants grown on ½ X Murashige and Skoog (MS)-agar plates (hereafter, referred to as MS-agar plates) under long days (16-h light and 8-h dark) was examined by RT-PCR. RT, reverse transcription. SM, size marker. kbp, kilobase pair. The PCR products were sequenced (see **Figure 57**).

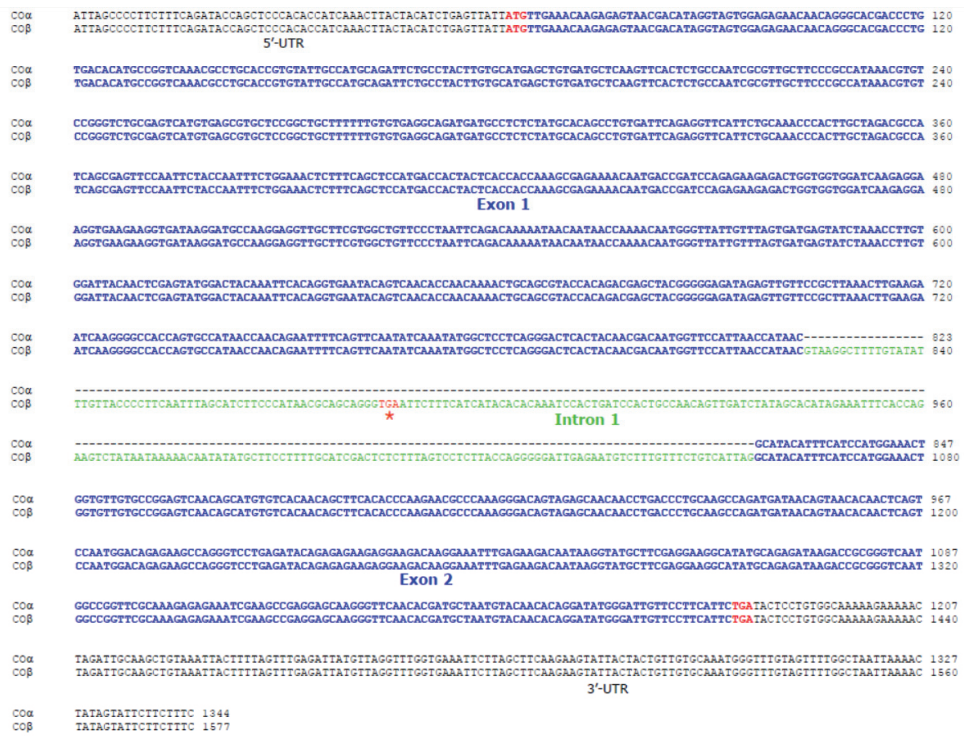

Figure 57. Nucleotide sequences of *COα* and *COβ* cDNAs

The nucleotide sequences of the PCR products amplified in **Figure 56** were determined by direct DNA sequencing and aligned using the ClustalW software (http://www.ebi.ac.uk/tools/msa/clustalw2/). Sequence analysis revealed that *CO* alternative splicing occurred by the retention of intron 1. As a result of the alternative splicing event, a premature termination codon was generated in the *COβ* transcript (red asterisk). The start and stop codons are marked in red. 5'-UTR and 3'-UTR, 5' and 3' untranslated regions, respectively.

Figure 58. Amino acid sequences of COα and COβ protein isoforms

Amino acid sequences were aligned using the ClustalW software (http://www.ebi.ac.uk/tools/msa/clustalw2/). Zinc finger domains (B-boxes) are marked in red, and the C-terminal CO, CO-LIKE, TOC1 (CCT) domain is marked in blue.

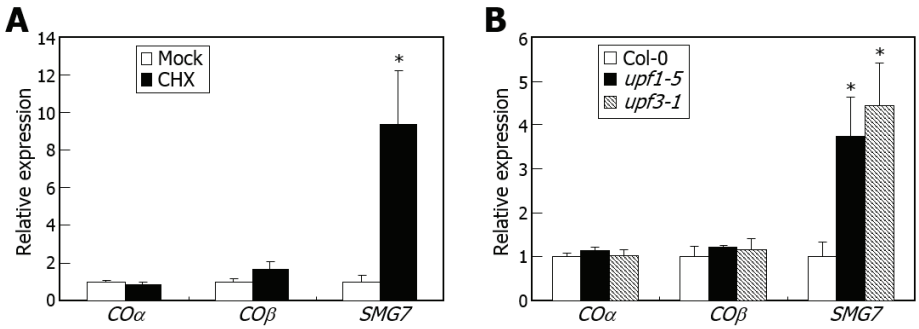

Figure 59. Sensitivity of *COβ* transcripts to nonsense-mediated mRNA decay

Ten-day-old Col-0 plants grown on MS-agar plates under LDs were subsequently incubated in MS liquid culture containing 20 μM cycloheximide (CHX) for 12 h before harvesting whole plant materials for total RNA extraction (**A**). The *upf1-5* and *upf3-1* mutants, which are defective in NMD (Hori and Watanabe, 2005; Arciga-Reyes *et al*., 2006), were used for total RNA extraction without CHX treatment (**B**). Steady-state levels of *COα* and *COβ* transcripts were examined by quantitative real-time RT-PCR (qRT-PCR). *SMG7* gene, which is involved in NMD (Rayson *et al*., 2012), was included in the assays as control. Biological triplicates were averaged and statistically analyzed using Student *t*-test (**P*< 0.01). Bars indicate standard error of the mean.

et al., 2006) (Figure 59B), suggesting that *CO* alternative splicing is productive and that *COβ* encodes a CO isoform.

Most transcription factors act as dimers to enhance DNA-binding specificity (Izawa *et al*., 1993; Vinson *et al*., 1993). I therefore examined whether COβ interacts with COα. Yeast two-hybrid assays using a series of COα deletions showed that COβ heterodimerizes with COα via the N-terminal ZF-containing region (Figures 55D and 55E). COα and COβ also formed homodimers (Figures 55E and 55G). The COα-COβ interaction was verified by *in vitro* pull-down assays using recombinant maltose-binding protein (MBP)-COβ fusion and ^{35}S-labeled COα polypeptides (Figure 55F). I also examined the COα-COβ interaction by bimolecular fluorescence complementation (BiFC) assay in *Arabidopsis* protoplasts (Figure 55G), indicating that COα and COβ form dimers in the nucleus.

COβ-mediated attenuation of COα function in flowering induction

Alternatively spliced protein isoforms often act as dominant negative regulators of plant transcription factors (Seo *et al*., 2011; Seo *et al*., 2012b). I hypothesized that COβ would suppress COα function, possibly by forming nonfunctional heterodimers.

I produced transgenic plants overexpressing a *MYC-COα* fusion driven by the cauliflower mosaic virus (CaMV) 35S promoter, resulting in 35S:*COα* (Figure 60). The 35S:*COα* plants exhibited early flowering (Figures 61A and 61B), as previously reported in plants overexpressing *CO* (Onouchi *et al*., 2000; Valverde *et al*., 2004; Lazaro *et al*., 2012; Song *et al*., 2012b). Notably, transgenic plants overexpressing *COβ* (35S:*COβ*) exhibited severely late flowering, as was observed in a *co* null mutant, *co-101* (Figures 61A and 61B). In addition, the early flowering of 35S:*COα* plants was suppressed in 35S:*COα* X 35S:*COβ* plants (Figures 61A and 61B). *COβ* was expressed more than 100-fold in the 35S:*COβ* and 35S:*COα*

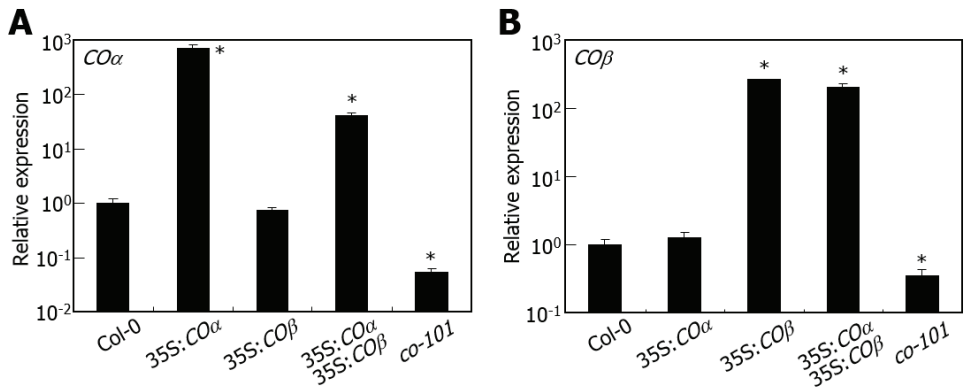

Figure 60. Levels of *COα* and *COβ* transcripts in *COα*- and *COβ*-overexpressing plants

A *MYC-COα* fusion, in which a MYC-coding sequence was fused in-frame to the 5'-end of the full-size *COα* cDNA, or a full-size *COβ* cDNA was overexpressed driven by the cauliflower mosaic virus (CaMV) 35S promoter in Col-0 plants, resulting in 35S:*COα* and 35S:*COβ*. The two transgenic plants were crossed to produce 35S:*COα* 35S:*COβ*. Levels of *COα* and *COβ* transcripts were examined by qRT-PCR (**A** and **B**, respectively). Ten-day-old whole plants grown on MS-agar plates under LDs were used for total RNA extraction. Biological triplicates were averaged and statistically analyzed (*t*-test, **P*< 0.01). Bars indicate standard error of the mean.

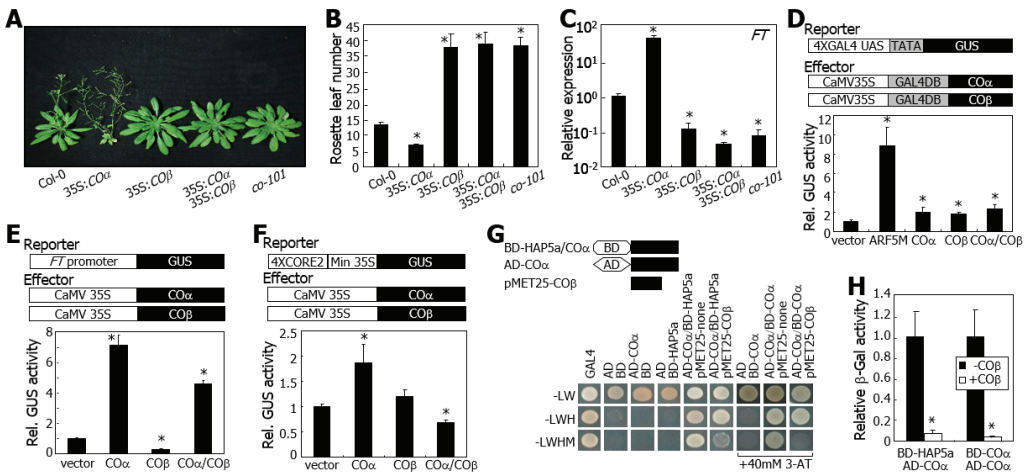

Figure 61. COβ inhibits COα function in the induction of flowering

(**A** and **B**) Flowering time. Five-week-old plants grown under LDs were photographed (**A**). Rosette leaves of 30 plants were counted and statistically analyzed using Student *t*-test (**P*< 0.01) (**B**). Bars, SE.

(**C**) *FT* expression. One-week-old plants grown on MS-agar plates were harvested at zeitgeber time 14 (ZT14). Biological triplicates of qRT-PCR were averaged and statistically treated (*t*-test, **P*< 0.01).

(**D**) Transcriptional activation activity of CO proteins in *Arabidopsis* protoplasts. ARF5M is a transcriptional activator (Tiwari *et al*., 2003).

(**E**) Inhibition of COα activity by COβ. The reporter and effector vectors were cotransformed into *Arabidopsis* protoplasts. Bars, SE (*t*-test, **P*< 0.01; $n = 5$).

(**F**) Inhibition of COα binding to DNA by COβ. The reporter vector harbors four copies of CO-responsive elements (COREs) fused to a minimal CaMV 35S promoter. Bars, SE (*t*-test, **P*< 0.01; $n = 3$).

(**G** and **H**) Inhibition of COα-COα and COα-HAP5a interactions by COβ. Yeast three-hybrid assays were performed using the pMET25-COβ expression vector (**G**, upper panel). Dimer formation was monitored by measuring cell growth on selective media (**G,** lower panel) and β-Gal assay (**H**). Bars, SE (*t*-test, **P*< 0.01, $n = 3$). 3-AT, 3-amino-1,2,4-triazole.

35S:*COβ* plants (Figures 60 and 62), indicating that the delay of flowering by *COβ* overexpression is not due to cosuppression of *COα* and *COβ*. Furthermore, the flowering times of the transgenic plants correlated with *FT* expression (Figure 61C). These observations indicate that COα function is attenuated by *COβ* overexpression.

To verify that the delayed flowering caused by *COβ* overexpression occurs via COα, *COβ* was overexpressed in *co-101* mutant, resulting in 35S:*COβ co-101*. The delayed flowering of *co-101* mutant was not affected by *COβ* overexpression (Figure 63), indicating that the COβ-mediated delay of flowering is mediated by COα.

Inhibition of COα DNA binding by COβ

I tested whether COβ inhibits COα–mediated transcriptional activation by measuring transient β-glucuronidase (GUS) expression in *Arabidopsis* protoplasts. COα and COβ both were able to activate GUS expression when introduced separately into the protoplast (Figure 61D). The result indicates that the transcriptional activation activities of COα and COβ are similar (Figure 61D), most likely because COβ has the glutamine (Gln)-rich region that mediates the transcriptional activation activity of CO (Tiwari *et al*., 2010). Importantly, COβ coexpression did not interfere with the ability of COα to activate the reporter, showing that COβ does not affect the transcriptional activation activity of COα.

FT is a direct target of CO (Samach *et al*., 2000; Wenkel *et al*., 2006; Tiwari *et al*., 2010). I examined whether COβ influences the COα-mediated activation of *FT* by transient GUS expression assays in *Arabidopsis* protoplasts using a reporter, in which a 2-kb promoter sequence of *FT* was fused to the *GUS* gene. GUS activity was significantly increased by COα overexpression but reduced by COβ overexpression (Figue 61E). In addition, COβ coexpression compromised the COα-mediated elevation of

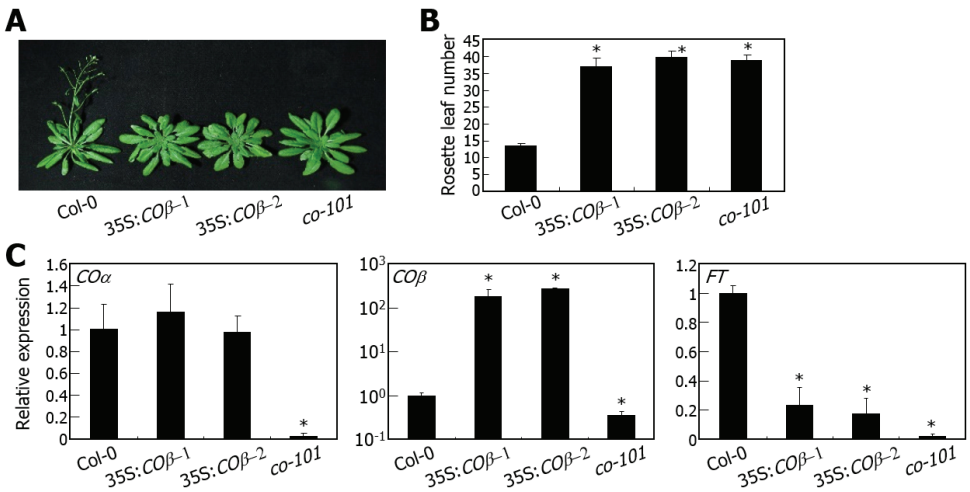

Figure 62. Flowering phenotype of *COβ*-overexpressing plants in Col-0 background

(**A** and **B**) Flowering time. A full-size *COβ* cDNA was overexpressed driven by the CaMV 35S promoter in Col-0 plants. The 35S:*COβ-1* transgenic line is equivalent to the 35S:*COβ* transgenic line described in **Figure 61A**. One additional line (35S:*COβ-2*) was included in the assays. Five-week-old plants grown in soil under LDs were photographed (**A**). Rosette leaf numbers of 20 plants were averaged and statistically analyzed (*t*-test, **P*< 0.01) (B). Bars indicate standard error of the mean.

(**C**) Levels of *COα*, *COβ*, and *FT* transcripts. Ten-day-old whole plants grown on MS-agar plates under LDs were harvested for total RNA extraction. Transcript levels were examined by qRT-PCR. Biological triplicates were averaged and statistically analyzed (*t*-test, **P*< 0.01). Bars indicate standard error of the mean.

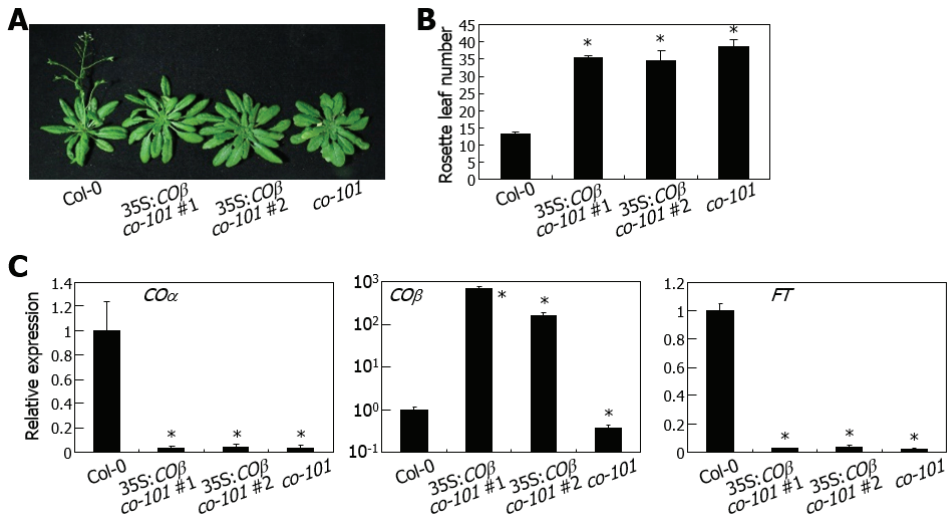

Figure 63. Flowering phenotype of *COβ*-overexpressing plants in *co-101* background

(**A** and **B**) Flowering time. A full-size *COβ* cDNA was overexpressed driven by the CaMV 35S promoter in the *CO*-deficient *co-101* mutant. Two independent transgenic lines (#1 and #2) were included in the assays. Plant growth (**A**) and flowering time measurements (**B**) were conducted as described in **Figures 62A and 62B**. Bars indicate standard error of the mean (*t*-test, **P*< 0.01).

(**C**) Levels of *COα*, *COβ*, and *FT* transcripts. Plant growth and qRT-PCR were conducted as described in **Figure 62C**. Bars indicate standard error of the mean (*t*-test, **P*< 0.01).

GUS activity.

COβ is nuclear-localized and sustains the transcription factor activity like COα (Figures 55G and 61D). I therefore suspected that the suppression of COα activity by COβ would be caused by a reduction of the binding of COα to *FT* promoter. To examine this, four copies of the CO-responsive element 2 (CORE2), which is responsible for DNA binding of CO (Tiwari *et al*., 2010), were fused to a minimal CaMV 35S promoter to drive *GUS* expression. The assays showed that COβ did not discernibly bind to DNA (Figure 61F); however, it reduced the binding of COα to DNA. Together with the interaction of COβ with COα, these observations indicate that COβ inhibits COα function by forming non-DNA binding heterodimers.

CO forms dimers with the HAP5a transcription factor to bind DNA (Wenkel *et al*., 2006). As shown above, COα and COβ are both capable of forming homodimers in yeast two-hybrid assays (Figure 55G). I found that COβ inhibited the formation of COα-HAP5a and COα-COα dimers (Figures 61G and 61H). This result suggests that COβ competitively interacts with COα to exclude COα-containing dimers from DNA, thus reducing CO activity, and consequently, *FT* expression.

Differential protein stabilities of CO isoforms

A critical question was how *CO* alternative splicing is associated with photoperiodic flowering. The diurnal accumulation of *COα* and *COβ* transcripts was not significantly affected by photoperiods (Figure 64A), although absolute quantitation of *COα* and *COβ* transcripts indicated that the relative levels of *COβ* transcripts were higher under short days (SDs) (Figures 64B and 64C). Moreover, *COβ* transcript levels did not differ significantly between LDs and SDs during zeitgeber time (ZT) 12-20, when CO is functionally important for photoperiodic flowering (Valverde *et al*., 2004), suggesting that *CO* alternative splicing is not physiologically

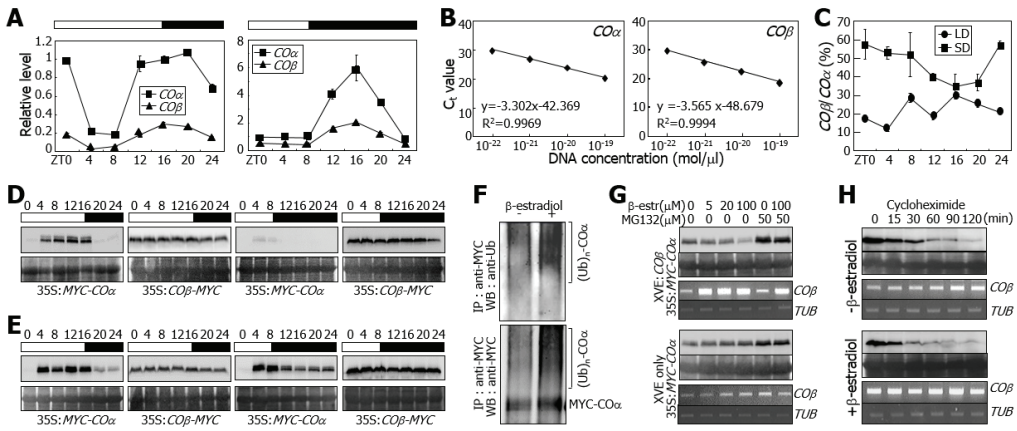

Figure 64. COβ facilitates COα degradation

(**A**) Accumulation of *COα* and *COβ* transcripts under LDs and SDs. Ten-day old whole plants grown on MS-agar plates were harvested at varying ZT points. Transcript levels were examined by qRT-PCR of biological triplicates (bars, SE; *t*-test, **P*< 0.01).

(**B** and **C**) Absolute quantification of *COα* and *COβ* transcripts. Ten-day old whole plants grown on MS-agar plates were harvested at varying ZT points. A series of 10-fold dilutions of plasmid DNA containing either *COα* or *COβ* cDNA was used to generate the standard curve (**B**). Ratios of *COβ*/*COα* were then calculated (**C**). Biological triplicates were averaged (bars, SE).

(**D** and **E**) Diurnal CO accumulation. MYC-COα and COβ-MYC fusions were overexpressed under control of the CaMV 35S promoter in Col-0 plants. Ten-day old plants grown on MS-agar plates were mock-treated (**D**) or treated with 50 μM MG132 (**E**) at ZT0. CO proteins were immunologically detected using anti-MYC antibody. Parts of Coomassie blue-stained gels were presented as loading control.

(**F**) Induction of COα ubiquitination by COβ. *COβ* cDNA expression was driven by the β-estradiol-inducible promoter in 35S:*COα* plants. Ten-day-old plants were incubated in MS liquid culture containing 50 μM MG132 and/or

100 μM β-estradiol for 12 h. Protein extracts were immunoprecipitated (IP) using anti-MYC antibody and subjected to immunological assays using anti-ubiquitin (upper panel) and anti-MYC (lower panel) antibodies.

(**G**) COβ-mediated degradation of COα in the light. The plants described in (**F**), grown for 10 d under LDs, were transferred to MS liquid culture containing varying concentrations of β-estradiol and MG132 for 12 h in the light. COα was immunologically detected as described in (**D**). Transcript levels were examined by RT-PCR. A tubulin gene (*TUB*) was used as an RNA quality control.

(**H**) COβ-mediated degradation of COα in the dark. The plants described in (**F**) were preincubated in MS liquid culture containing MG132 and/or β-estradiol for 12 h and transferred to fresh MS liquid culture containing 1 mM cycloheximide in the dark. Immunological assays and RT-PCR were performed as described in (**G**).

important at the RNA level.

I next examined the diurnal accumulation of CO proteins. Whereas COα reached peak levels during ZT12-16 under LDs, it was barely detected under SDs (Figure 64D), as reported previously (Valverde *et al*., 2004; Jang *et al*., 2008; Liu *et al*., 2008; Lazaro *et al*., 2012; Song *et al*., 2012b). Notably, COβ levels remained unchanged under both LDs and SDs, suggesting that the physiological significance of CO alternative splicing is exerted more prominently at the protein level than at the RNA level. It is known that CO protein stability is regulated through ubiquitin/proteasome-dependent pathways (Valverde *et al*., 2004). I therefore examined the diurnal patterns of COα and COβ accumulation in the presence of MG132, a potent proteasome inhibitor (Tsubuki *et al*., 1996). Whereas COα levels remained high even under SDs, COβ levels were not influenced by MG132 under either LDs or SDs (Figure 64E). These results indicate that COβ, unlike COα, is resistant to ubiquitin/proteasome-dependent degradation.

Facilitation of COα degradation by COβ

It has been documented that dynamic dimer formation influences protein stability (Bender *et al*., 2000; Dunbar *et al*., 2004; Adhikary *et al*., 2005; Jang *et al*., 2007; Lin *et al*., 2012). Therefore, one interesting question was whether COβ affects the susceptibility of COα to ubiquitin/proteasome-dependent degradation. I first examined whether COβ affects COα ubiquitination by expressing *COβ* under the β-estradiol-inducible promoter in 35S:*COα* plants. The level of polyubiquitinated COα was elevated significantly by the induction of *COβ* expression (Figures 64F and 65). Additionally, COα degradation was amplified by increasing concentrations of the inducer in the light (Figure 64G). Moreover, the effects of COβ on COα degradation was reduced in the presence of MG132

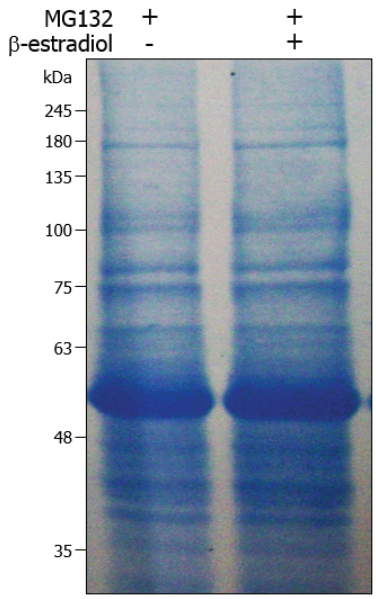

Figure 65. Preparation of total protein extracts for *in vivo* ubiquitination assay

Plants grown on MS-agar plates for 10 d under LDs were transferred to MS liquid culture containing 50 μM MG132 alone or 50 μM MG132 and 100 μM β-estradiol for 12 h. Whole plants were used for the preparation of total protein extracts. Approximately 20 μg of total protein extracts were loaded on 10% SDS-PAGE and stained with Coomassie blue R250. kDa, kilodalton.

(Figure 64G), indicating that COβ induces the ubiquitin/proteasome-mediated degradation of COα. I also performed the assays on protein stability in the dark, because COP1-mediated degradation of CO at night is also important for photoperiodic control of flowering (Jang *et al*., 2008; Liu *et al*., 2008). The 35S:*COα* transgenic plants expressing *COβ* driven by a β-estradiol-inducible promoter was preincubated in MS liquid culture for 12 h in the presence of MG132 alone or MG132 and inducer in the light and transferred to fresh MS liquid culture containing cycloheximide in the dark. I found that COα was degraded more rapidly in the presence of COβ production, further supporting the role of COβ in COα degradation (Figure 64H).

Effects of COβ on the interactions between COα and E3 ligases

A question was how COβ facilitates COα degradation. I investigated the effects of COβ on the interaction of COα with CO-destabilizing and -stabilizing E3 ligases by yeast three-hybrid assay, in which *COβ* expression was driven by a methionine-repressible promoter (Figure 66A). Surprisingly, COβ enhanced the interaction of COα with the CO-degrading enzymes HOS1 and COP1, but inhibited the interaction with CO-stabilizing enzyme FKF1, as examined by cell growth on selective media (Figure 66B) and β-Gal activity assay (Figure 66C). These results suggest that COβ modulates the accessibility of COα to the E3 enzymes.

Altogether, the data demonstrate that CO plays an active role in regulating its own diurnal protein dynamics during the induction of photoperiodic flowering. In the morning and at night, COβ triggers CO degradation by promoting its accessibility to HOS1 and COP1 (Figure 66D). In contrast, FKF1 protects CO by competing with COβ in late afternoon, contributing to the sharp accumulation of CO and flowering induction under LDs. The data provide a novel paradigm for enzyme reactions. Unlike the

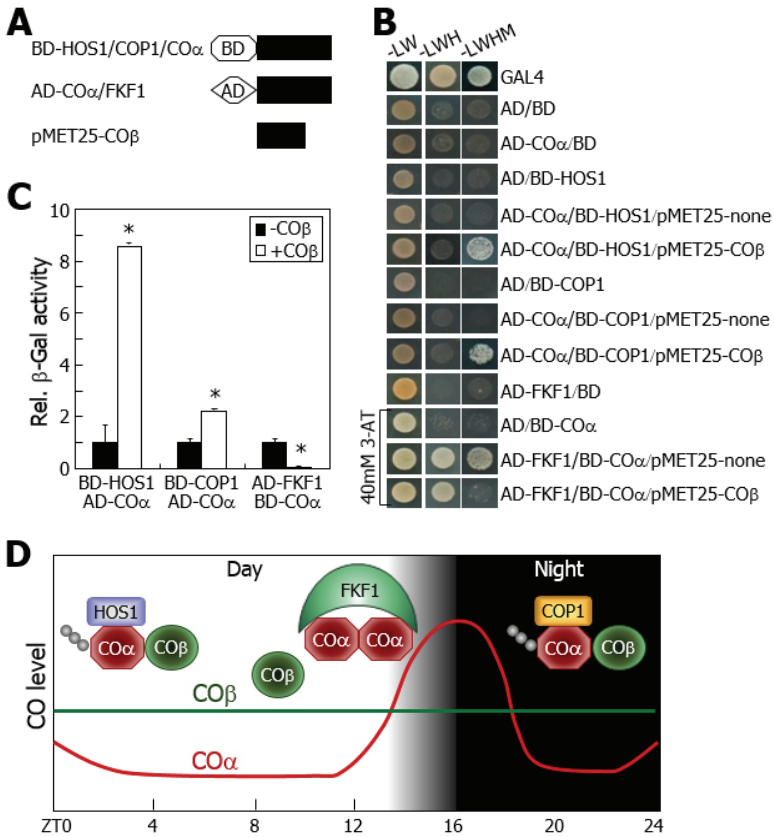

Figure 66. Self-directed control of the diurnal CO dynamics

(**A-C**) Interactions between CO isoforms and E3 enzymes. A set of expression constructs containing genes encoding CO, HOS1, FKF1, and COP1 was generated (**A**). Yeast three-hybrid assays were performed to examine tripartite interactions by measuring cell growth on selective media (**B**) and β-Gal activity (**C**). In (**C**), bars are SE of four measurements (*t*-test, **P*< 0.01).

(**D**) Schematic diagram illustrating the self-directed control of the diurnal CO dynamics. COα-COβ heterodimers are susceptible to HOS1 in the morning and COP1 at night, while COα-COα homodimers are resistant to E3 ubiquitin ligases.

passive role of substrates in most enzymatic reactions, CO plays a rather active role in the E3 enzyme reactions.

DISCUSSION

Regulation of the diurnal COα accumulation by COβ

In the last decade, elucidation of molecular players and regulatory mechanisms underlying the light-dependent CO accumulation dynamics has improved our understanding of photoperiodic flowering. It has been shown that a small group of E3 enzymes is responsible for the diurnal CO dynamics (Jang *et al*., 2008; Liu *et al*., 2008; Lazaro *et al*., 2012; Song *et al*., 2012b). Recently, it has been reported that CO-interacting proteins other than E3 enzymes also influence the CO protein stability (Endo *et al*., 2013; Song *et al*., 2014). The data showed that COβ is such a CO-interacting protein.

The most notable feature of COβ is its ability to modulate the accessibility of COα to E3 ubiquitin ligases. I found that COβ increases the interaction of COα with CO-destabilizing E3 enzymes, HOS1 and COP1. HOS1 is responsible for the degradation of CO during the daytime (Lazaro *et al*., 2012), and COP1 directs the CO degradation at night (Jang *et al*., 2008; Liu *et al*., 2008). I observed that COβ overproduction causes COα destabilization in both light and dark conditions. Moreover, COβ reduces the interaction of COα with FKF1, which stabilizes CO in late afternoon under LDs (Song *et al*., 2012b). My proposed working scenario depicts that under LDs, COβ assists HOS1 in the morning and COP1 at night to degrade CO. However, in late afternoon, FKF1 protects CO from the ubiquitin/proteasome-degradation, and CO accumulates to a high level.

Alternative splicing provides diverse regulatory mechanisms at the transcriptional and post-transcriptional levels by producing multiple RNA isoforms and in some cases protein isoforms that are functionally distinct from the authentic proteins (Seo *et al*., 2011; Jame *et al*., 2012; Seo *et al*., 2012b; Staiger and Brown, 2013). A self-regulatory role of alternative

splicing has also been reported in recent years (Seo *et al*., 2011; Seo *et al*., 2012b). One common feature of these regulatory schemes is that the DNA binding activity of authentic transcription factors is negatively regulated by the protein variant. I found that COβ also excludes COα from DNA binding. It is interesting that COβ also modulates the accessibility of COα to E3 ubiquitin ligases, further extending the functional repertoire provided by alternative splicing.

Active role of substrate in enzyme reactions

It has been reported that PROTEIN KINASE Cγ (PKCγ), a substrate of HEAT-SHOCK PROTEIN 90 (HSP90), regulates the activity of HSP90 by protein phosphorylation in *Arabidopsis* (Lu *et al*., 2014). Although it is widely believed that the stability of substrates is simply regulated by HSPs in a passive manner, PKCγ phosphorylates HSP90 to modulate the binding affinity of HSP90 to ATP and co-chaperone proteins (Lu *et al*., 2014), indicating that PKCγ plays a rather active role in the chaperoning process.

The functional relationship between PKCγ and HSP90 is similar to what I observed with the regulation of COα (CO) accessibility to E3 enzymes by COβ. In the proposed working scenario underlying the CO degradation by E3 ligases, CO is not simply targeted by E3 enzymes. Instead, CO acts as a self-regulator of its diurnal accumulation through the dynamic interaction between the two protein isoforms and the modulation of its accessibility to E3 enzymes, supporting the physiological significance of COβ.

COβ is resistant to E3 enzymes unlike COα, and its accumulation does not discernibly change throughout the entire day, suggesting that the protein level of COβ correlates with the accumulation of *COβ* transcripts. The *COβ* transcript level peaks in early morning and at night under LDs, but the early morning peak disappears under SDs (Figure 64A), although the

fluctuations are not as prominent as those of the *COα* transcript level. It is remarkable that the diurnal accumulation patterns of the *COβ* transcripts are somewhat similar to the well-established *CO* transcription patterns under LDs and SDs (Andrés and Coupland, 2012). Therefore, it is possible that the distinct patterns of *CO* transcription under different photoperiods is required primarily not for the production of COα but for the production of the COβ inhibitor. This notion might explain the discrepancy between the diurnal accumulation patterns of CO protein and CO transcript.

REFERENCES

Adhikary, S., Marinoni, F., Hock, A., Hulleman, E., Popov, N., Beier, R., Bernard, S., Quarto, M., Capra, M., Goettig, S., Kogel, U., Scheffner, M., Helin, K. and Eilers, M. (2005) The ubiquitin ligase HectH9 regulates transcriptional activation by Myc and is essential for tumor cell proliferation. *Cell* 123, 409-421.

Amasino, R. (2010) Seasonal and developmental timing of flowering. *Plant J.* **61**, 1001-1013.

Andrés, F. and Coupland, G. (2012) The genetic basis of flowering responses to seasonal cues. *Nat. Rev. Genet.* **13**, 627-639.

Arciga-Reyes, L., Wootton, L., Kieffer, M. and Davies, B. (2006) UPF1 is required for nonsense-mediated mRNA decay (NMD) and RNAi in *Arabidopsis*. *Plant J.* **47**, 480-489.

Bauer, P., Ling, H. Q. and Guerinot, M. L. (2007) FIT, the FER-LIKE IRON DEFICIENCY INDUCED TRANSCRIPTION FACTOR in *Arabidopsis*. *Plant Physiol. Biochem.* **45**, 260-261.

Belin, C., deFranco, P. O., Bourbousse, C., Chaignepain, S., Schmitter, J. M., Vavasseur, A., Giraudat, J., Barbier-Brygoo, H. and Thomine, S. (2006) Identification of features regulating OST1 kinase activity and OST1 function in guard cells. *Plant Physiol*. **141**, 1316-1327.

Bender, A. T., Demady, D. R. and Osawa, Y. (2000) Ubiquitination of neuronal nitric-oxide synthase *in vitro* and *in vivo*. *J. Biol. Chem.* **275**,

17407-17411.

Boudsocq, M., Barbier-Brygoo, H. and Lauri`ere, C. (2004) Identification of nine sucrose nonfermenting 1-related protein kinases 2 activated by hyperosmotic and saline stresses in *Arabidopsis thaliana*. *J. Biol. Chem*. **279**, 41758-41766.

Bournier, M., Tissot, N., Mari, S., Boucherez, J., Lacombe, E., Briat, J. F. and Gaymard, F. (2013) *Arabidopsis ferritin 1* (AtFer1) gene regulation by the phosphate starvation response 1 (AtPHR1) transcription factor reveals a direct molecular link between iron and phosphate homeostasis. *J. Biol. Chem*. **288**, 22670-22680.

Briat, J. F., Curie, C. and Gaymard, F. (2007) Iron utilization and metabolism in plants. *Curr. Opin. Plant Biol.* **10**, 276-282.

Burko, Y., Geva, Y., Refael-Cohen, A., Shleizer-Burko, S., Shani, E., Berger, Y., Halon, E., Chuck, G., Moshelion, M. and Ori, N. (2011) From organelle to organ: ZRIZI MATE-type transporter is an organelle transporter that enhances organ initiation. *Plant Cell Physiol*. **52**, 518-527.

Bustin, S. A. (2000) Absolute quantification of mRNA using real-time reverse transcription polymerase chain reaction assays. *J. Mol. Endocrinol.* **25**, 169-193.

Choi, K., Kim, S., Kim, S. Y., Kim, M., Hyun, Y., Lee, H., Choe, S., Kim, S. G., Michaels, S. and Lee, I. (2005) *SUPPRESSOR OF FRIGIDA3* encodes a nuclear ACTIN-RELATED PROTEIN6 required for floral repression in *Arabidopsis*. *Plant Cell* **17**, 2647-2660.

Christmann, A., Moes, D., Himmelbach, A., Yang, Y., Tang, Y. and Grill, E. (2006) Integration of abscisic acid signalling into plant responses. *Plant Biol*. **8**, 314-325.

Clough, S. J. and Bent, A. F. (1998) Floral dip: a simplified method for *Agrobacterium*-mediated transformation of *Arabidopsis thaliana*. *Plant J.* **16**, 735-743.

Colangelo, E. P. and Guerinot, M. L. (2004) The essential basic helix-loop-helix protein FIT1 is required for the iron deficiency response. *Plant Cell* **16**, 3400-3412.

Corbesier, L., Vincent, C., Jang, S., Fornara, F., Fan, Q., Searle, I., Giakountis, A., Farrona, S., Gissot, L., Turnbull, C. and Coupland, G. (2007) FT protein movement contributes to long-distance signaling in floral induction of *Arabidopsis*. *Science* **316**, 1030-1033.

Curie, C., Panaviene, Z., Loulergue, C., Dellaporta, S. L., Briat, J. F. and Walker, E. L. (2001) Maize *yellow stripe1* encodes a membrane protein directly involved in Fe(III) uptake. *Nature* **409**, 346-349.

Curie, C. and Briat, J. F. (2003) Iron transport and signaling in plants. *Annu. Rev. Plant Biol.* **54**, 183-206.

Curie, C., Cassin, G., Couch, D., Divol, F., Higuchi, K., Le Jean, M., Misson, J., Schikora, A., Czernic, P. and Mari, S. (2009) Metal movement within the plant: contribution of nicotianamine and yellow stripe 1-like transporters. *Ann. Bot.* **103**, 1-11.

Debeaujon, I., Peeters, A. J., Léon-Kloosterziel, K. M. and Koornneef, M.

(2001) The *TRANSPARENT TESTA12* gene of *Arabidopsis* encodes a multidrug secondary transporter-like protein required for flavonoid sequestration in vacuoles of the seed coat endothelium. *Plant Cell* **13**, 853-871.

Déjardin, A., Sokolov, L. N. and Kleczkowski, L. A. (1999) Sugar/osmoticum levels modulate differential abscisic acid-independent expression of two stress-responsive sucrose synthase genes in *Arabidopsis*. *Biochem. J.* **2**, 503-509.

Diener, A. C., Gaxiola, R. A. and Fink, G. R. (2001) *Arabidopsis ALF5*, a multidrug efflux transporter gene family member, confers resistance to toxins. *Plant Cell* **13**, 1625-1638.

Dunbar, A. Y., Kamada, Y., Jenkins, G. J., Lowe, E. R., Billecke, S. S. and Osawa, Y. (2004) Ubiquitination and degradation of neuronal nitric-oxide synthase *in vitro*: dimer stabilization protects the enzyme from proteolysis. *Mol. Pharmacol.* **66**, 964-969.

Durrett, T. P., Gassmann, W. and Rogers, E. E. (2007) The FRD3-mediated efflux of citrate into the root vasculature is necessary for efficient iron translocation. *Plant Physiol*. **144**, 197-205.

Duy, D., Stübe, R., Wanner, G. and Philippar, K. (2011) The chloroplast permease PIC1 regulates plant growth and development by directing homeostasis and transport of iron. *Plant Physiol*. **155**, 1709-1722.

Eide, D., Broderius, M., Fett, J. and Guerinot, M. L. (1996) A novel iron-regulated metal transporter from plants identified by functional expression in yeast. *Proc. Natl. Acad. Sci. U.S.A.* **93**, 5624-5628.

Endo, M., Tanigawa, Y., Murakami, T., Araki, T. and Nagatani, A. (2013) PHYTOCHROME-DEPENDENT LATE-FLOWERING accelerates flowering through physical interactions with phytochrome B and CONSTANS. *Proc. Natl. Acad. Sci. U.S.A.* **110**, 18017-18022.

Fobis-Loisy, I., Loridon, K., Lobr´eaux, S., Lebrun, M. and Briat, J. F. (1995) Structure and differential expression of two maize ferritin genes in response to iron and abscisic acid. *Eur. J. Biochem*. **231**, 609-619.

Fujii, H., Chinnusamy, V., Rodrigues, A., Rubio, S., Antoni, R., Park, S.Y., Cutler, S. R., Sheen, J., Rodriguez, P. L. and Zhu, J. K. (2009) *In vitro* reconstitution of an abscisic acid signalling pathway. *Nature* **462**, 660-664.

Fujii, H., Verslues, P. E. and Zhu, J. K. (2007) Identification of two protein kinases required for abscisic acid regulation of seed germination, root growth, and gene expression in *Arabidopsis*. *Plant Cell* **19**, 485-494.

Fujita, Y., Nakashima, K., Yoshida, T., Katagiri, T., Kidokoro, S., Kanamori, N., Umezawa, T., Fujita, M., Maruyama, K., Ishiyama, K., Kobayashi, M., Nakasone, S., Yamada, K., Ito, T., Shinozaki, K. and Yamaguchi-Shinozaki, K. (2009) Three SnRK2 protein kinases are the main positive regulators of abscisic acid signaling in response to water stress in *Arabidopsis. Plant Cell Physiol*. **50**, 2123-2132.

Fukao, Y., Ferjani, A., Tomioka, R., Nagasaki, N., Kurata, R., Nishimori, Y., Fujiwara, M. and Maeshima, M. (2011) iTRAQ analysis reveals mechanisms of growth defects due to excess zinc in *Arabidopsis*. *Plant Physiol*. **155**, 1893-1907.

Gaymard, F., Boucherez, J. and Briat, J. F. (1996) Characterization of a ferritin mRNA from *Arabidopsis thaliana* accumulated in response to iron through an oxidative pathway independent of abscisic acid. *Biochem. J.* **318**, 67-73.

Geiger, D., Scherzer, S., Mumm, P., Stange, A., Marten, I., Bauer, H., Ache, P., Matschi, S., Liese, A., Al-Rasheid, K. A., Romeis, T. and Hedrich, R. (2009) Activity of guard cell anion channel SLAC1 is controlled by drought-stress signaling kinase-phosphatase pair. *Proc. Natl. Acad. Sci. U.S.A.* **106**, 21425-21430.

Gepstein, S. (2004) Leaf senescence-not just a 'wear and tear' phenomenon. *Genome Biol*. **5**, 212.

Goswami, S., Aich, K., Das, S., Das, A. K., Sarkar, D., Panja, S., Mondal, T. K. and Mukhopadhyay, S. (2013) A red fluorescence 'off-on' molecular switch for selective detection of Al^{3+}, Fe^{3+} and Cr^{3+}: experimental and theoretical studies along with living cell imaging. *Chem. Commun*. **49**, 10739-10741.

Grässer, F. A. and König, S. (1992) Phosphorylation of SV40 large T antigen at threonine residues results in conversion to a lower apparent molecular weight form. *Arch. Virol*. **126**, 313-320.

Graziano, M., Beligni, M. V. and Lamattina, L. (2002) Nitric oxide improves internal iron availability in plants. *Plant Physiol*. **130**, 1852-1859.

Green, L. S. and Rogers, E. E. (2004) FRD3 controls iron localization in

Arabidopsis. *Plant Physiol*. **136**, 2523-2531.

Grotz, N. and Guerinot, M. L. (2006) Molecular aspects of Cu, Fe and Zn homeostasis in plants. *Biochim. Biophys. Acta* **1763**, 595-608.

Guerinot, M. L. and Yi, Y. (1994) Iron: nutritious, noxious, and not readily available. *Plant Physiol.* **104**, 815-820.

Guo, F. Q. and Crawford, N. M. (2005) *Arabidopsis* nitric oxide synthase1 is targeted to mitochondria and protects against oxidative damage and dark-induced senescence. *Plant Cell* **17**, 3436-3450.

Gutierrez, L., Mauriat, M., Guénin, S., Pelloux, J., Lefebvre, J. F., Louvet, R., Rusterucci, C., Moritz, T., Guerineau, F., Bellini, C. and Van Wuytswinkel, O. (2008) The lack of a systematic validation of reference genes: a serious pitfall undervalued in reverse transcription-polymerase chain reaction (RT-PCR) analysis in plants. Plant *Biotechnol. J.* **6**, 609-618.

Halford, N. G. and Hey, S. J. (2009) Snf1-related protein kinases (SnRKs) act within an intricate network that links metabolic and stress signalling in plants. *Biochem. J.* **419**, 247-259.

Hall, J. L. and Williams, L. E. (2003) Transition metal transporters in plants. *J. Exp. Bot*. **54**, 2601-2613.

Himelblau, E. and Amasino, R. M. (2001) Nutrients mobilized from leaves of *Arabidopsis thaliana* during leaf senescence. *J. Plant Physiol*. **158**, 1317-1323.

Hirayama, T., Okuda, K. and Nagasawa, H. (2013) A highly selective turn-on fluorescent probe for iron(II) to visualize labile iron in living cells. *Chem. Sci*. **4**, 1250-1256.

Hori, K. and Watanabe, Y. (2005) UPF3 suppresses aberrant spliced mRNA in *Arabidopsis*. *Plant J.* **43**, 530-540.

Hrabak, E. M., Chan, C. W., Gribskov, M., Harper, J. F., Choi, J. H., Halford, N., Kudla, J., Luan, S., Nimmo, H. G., Sussman, M. R., Thomas, M., Walker-Simmons, K., Zhu, J. K. and Harmon, A. C. (2003) The *Arabidopsis* CDPK-SnRK superfamily of protein kinases. *Plant Physiol*. **132**, 666-680.

Hubbard, K. E., Nishimura, N., Hitomi, K., Getzoff, E. D. and Schroeder, J. I. (2010) Early abscisic acid signal transduction mechanisms: newly discovered components and newly emerging questions. *Genes Dev*. **24**, 1695-1708.

Hvorup, R. N., Winnen, B., Chang, A. B., Jiang, Y., Zhou, X. F. and Saier, Jr, M. H. (2003) The multidrug/oligosaccharidyl-lipid/polysaccharide (MOP) exporter superfamily. *Eur. J. Biochem*. 270, 799-813.

Iwata, Y. and Koizumi, N. (2005) An *Arabidopsis* transcription factor, AtbZIP60, regulates the endoplasmic reticulum stress response in a manner unique to plants. *Proc. Natl. Acad. Sci. U.S.A*. **102**, 5280-5285.

Izawa, T., Foster, R. and Chua, N. H. (1993) Plant bZIP protein DNA binding specificity. *J. Mol. Biol.* **230**, 1131-1144.

Jakoby, M., Wang, H. Y., Reidt, W., Weisshaar, B. and Bauer, P. (2004) FRU (BHLH029) is required for induction of iron mobilization genes in *Arabidopsis thaliana*. *FEBS Lett.* **577**, 528-534.

James, A. B., Syed, N. H., Bordage, S., Marshall, J., Nimmo, G. A., Jenkins, G. I., Herzyk, P., Brown, J. W. and Nimmo, H. G. (2012) Alternative splicing mediates responses of the *Arabidopsis* circadian clock to temperature changes. *Plant Cell* **24**, 961-981.

Jang, I. C., Yang, J. Y., Seo, H. S. and Chua, N. H. (2005) HFR1 is targeted by COP1 E3 ligase for post-translational proteolysis during phytochrome A signaling. *Genes Dev.* 19, 593-602.

Jang, I. C., Yang, S. W., Yang, J. Y., Chua, N. H. (2007) Independent and interdependent functions of LAF1 and HFR1 in phytochrome A signaling. *Genes Dev.* **21**, 2100-2111.

Jang, S., Marchal, V., Panigrahi, K. C., Wenkel, S., Soppe, W., Deng, X. W., Valverde, F. and Coupland, G. (2008) *Arabidopsis* COP1 shapes the temporal pattern of CO accumulation conferring a photoperiodic flowering response. *EMBO J.* **27**, 1277-1288.

Jefferson, R. A., Kavanagh, T. A. and Bevan, M. W. (1987) GUS fusions: beta-glucuronidase as a sensitive and versatile gene fusion marker in higher plants. *EMBO J.* **6**, 3901-3907.

Jeong, J. and Guerinot, M. L. (2009) Homing in on iron homeostasis in plants. *Trends Plant Sci*. **14**, 280-285.

Kalyna, M., Simpson, C. G., Syed, N. H., Lewandowska, D., Marquez, Y., Kusenda, B., Marshall, J., Fuller, J., Cardle, L., McNicol, J., Dinh, H. Q., Barta, A. and Brown, J. W. (2012) Alternative splicing and nonsense-mediated decay modulate expression of important regulatory genes in *Arabidopsis*. *Nucleic Acids Res.* **40**, 2454-2469.

Kennelly, P. J. and Krebs, E. G. (1991) Consensus sequences as substrate specificity determinants for protein kinases and protein phosphatases. *J. Biol. Chem.* **266**, 15555-15558.

Kim, S. A., Punshon, T., Lanzirotti, A., Li, L., Alonso, J. M., Ecker, J. R., Kaplan, J. and Guerinot, M. L. (2006) Localization of iron in *Arabidopsis* seed requires the vacuolar membrane transporter VIT1. *Science* **314**, 1295-1298.

Kim, S. A., Yoon, J. H., Lee, S. H. and Ahn, S. G. (2005) Polo-like kinase 1 phosphorylates heat shock transcription factor 1 and mediates its nuclear translocation during heat stress. *J. Biol. Chem*. **280**, 12653-12657.

Kim, S. G., Lee, S., Ryu, J. and Park, C. M. (2010) Probing protein structural requirements for activation of membrane-bound NAC transcription factors in *Arabidopsis* and rice. *Plant Sci*. **178**, 239-244.

Kim, S. Y., Kim, S. G., Kim, Y. S., Seo, P. J., Bae, M., Yoon, H. K. and Park, C. M. (2007) Exploring membrane-associated NAC transcription factors in *Arabidopsis*: implications for membrane biology in genome regulation. *Nucleic Acids Res.* **35**, 203-213.

Kim, Y. S., Kim, S. G., Park, J. E., Park, H. Y., Lim, M. H., Chua, N. H.

and Park, C. M. (2006) A membrane-bound NAC transcription factor regulates cell division in *Arabidopsis*. *Plant Cell* **18**, 3132-3144.

Klatte, M., Schuler, M., Wirtz, M., Fink-Straube, C., Hell, R. and Bauer, P. (2009) The analysis of *Arabidopsis* nicotianamine synthase mutants reveals functions for nicotianamine in seed iron loading and iron deficiency responses. *Plant Physiol.* **150**, 257-271.

Klimczak, L. J., Schindler, U. and Cashmore, A. R. (1992) DNA binding activity of the *Arabidopsis* G-box binding factor GBF1 is stimulated by phosphorylation by casein kinase II from broccoli. *Plant Cell* **4**, 87-98.

Kobayashi, Y. and Weigel, D. (2007) Move on up, it's time for change-mobile signals controlling photoperiod-dependent flowering. *Genes Dev* **21**, 2371-2384.

Kwon, Y. J., Park, M. J., Kim, S. G., Baldwin, I. T. and Park, C. M. (2014) Alternative splicing and nonsense-mediated decay of circadian clock genes under environmental stress conditions in *Arabidopsis*. *BMC Plant Biol.* **14**, 136.

Lanquar, V., Lelièvre, F., Bolte, S., Hamès, C., Alcon, C., Neumann, D., Vansuyt, G., Curie, C., Schröder, A., Krämer, U. Barbier-Brygoo, H. and Thomine, S. (2005) Mobilization of vacuolar iron by AtNRAMP3 and AtNRAMP4 is essential for seed germination on low iron. *EMBO J.* **24**, 4041-4051.

Laubinger, S., Marchal, V., Le Gourrierec, J., Wenkel, S., Adrian, J., Jang, S., Kulajta, C., Braun, H., Coupland, G. and Hoecker, U. (2006)

Arabidopsis SPA proteins regulate photoperiodic flowering and interact with the floral inducer CONSTANS to regulate its stability. *Development* **133**, 3213-3222.

Lazaro, A., Valverde, F., Piñeiro, M. and Jarillo, J. A. (2012) The *Arabidopsis* E3 ubiquitin ligase HOS1 negatively regulates CONSTANS abundance in the photoperiodic control of flowering. *Plant Cell* **24**, 982-999.

Lee, S. C., Lan, W., Buchanan, B. B. and Luan, S. (2009) A protein kinase-phosphatase pair interacts with an ion channel to regulate ABA signaling in plant guard cells. *Proc. Natl. Acad. Sci. U.S.A*. **106**, 21419-21424.

Leopold, A. C. (1961) Senescence in plant development: the death of plants or plant parts may be of positive ecological or physiological value. *Science* **134**, 1727-1732.

Li, L., He, Z., Pandey, G. K., Tsuchiya, T. and Luan, S. (2002) Functional cloning and characterization of a plant efflux carrier for multidrug and heavy metal detoxification. *J. Biol. Chem*. **277**, 5360-5368.

Lin, C. L., Huang, Y. T. and Richter, J. D. (2012) Transient CPEB dimerization and translational control. *RNA* **18**, 1050-1061.

Ling, H. Q., Koch, G., Bäumlein, H. and Ganal, M. W. (1999) Map-based cloning of chloronerva, a gene involved in iron uptake of higher plants encoding nicotianamine synthase. *Proc. Nal. Acad. Sci. U.S.A*. **96**, 7098-7103.

Liu, B., Zuo, Z., Liu, H., Liu, X. and Lin, C. (2011) *Arabidopsis* cryptochrome 1 interacts with SPA1 to suppress COP1 activity in response to blue light. *Genes Dev.* **25**, 1029-1034.

Liu, J., Magalhaes, J. V., Shaff, J. and Kochian, L. V. (2009) Aluminum-activated citrate and malate transporters from the MATE and ALMT families function independently to confer *Arabidopsis* aluminum tolerance. *Plant J.* **57**, 389-399.

Liu, J. X., Srivastava, R., Che, P. and Howell, S. H. (2007a) An endoplasmic reticulum stress response in *Arabidopsis* is mediated by proteolytic processing and nuclear relocation of a membrane-associated transcription factor, bZIP28. *Plant Cell* **19**, 4111-4119.

Liu, J. X., Srivastava, R., Che, P. and Howell, S. H. (2007b) Salt stress responses in *Arabidopsis* utilize a signal transduction pathway related to endoplasmic reticulum stress signaling. *Plant J.* **51**, 897-909.

Liu, L. J., Zhang, Y. C., Li, Q. H., Sang, Y., Mao, J., Lian, H. L., Wang, L. and Yang, H. Q. (2008) COP1-mediated ubiquitination of CONSTANS is implicated in cryptochrome regulation of flowering in *Arabidopsis*. *Plant Cell* **20**, 292-306.

Liu, S. R. and Wu, S. P. (2012) New water-soluble highly selective fluorescent chemosensor for Fe(III) ions and its application to living cell imaging. *Sens. Actuators B* **171−172**, 1110-1116.

Liu, Y. G., Mitsukawa, N., Oosumi, T. and Whittier, R. F. (1995) Efficient isolation and mapping of *Arabidopsis thaliana* T-DNA insert junctions by

thermal asymmetric interlaced PCR. *Plant J.* **8**, 457-463.

Lobreaux, S., Massenet, O. and Briat, J. F. (1992) Iron induces ferritin synthesis in maize plantlets. *Plant Mol. Biol*. **19**, 563-575.

Long, T. A., Tsukagoshi, H., Busch, W., Lahner, B., Salt, D. E. and Benfey, P. N. (2010) The bHLH transcription factor POPEYE regulates response to iron deficiency in *Arabidopsis* roots. *Plant Cell* **22**, 2219-2236.

Lu, X. A., Wang, X., Zhuo, W., Jia, L., Jiang, Y., Fu, Y. and Luo, Y. (2014) The regulatory mechanism of a client kinase controlling its own release from Hsp90 chaperone machinery through phosphorylation. *Biochem. J.* **457**, 171-183.

Ma, Y., Szostkiewicz, I., Korte, A., Moes, D., Yang, Y., Christmann, A. and Grill, E. (2009) Regulators of PP2C phosphatase activity function as abscisic acid sensors. *Science* **324**, 1064-1068.

Magalhaes, J. V., Liu, J., Guimarães, C. T., Lana, U. G., Alves, V. M., Wang, Y. H., Schaffert, R. E., Hoekenga, O. A., Pineros, M. A., Shaff, J. E., Klein. P. E., Carneiro, N. P., Coelho, C. M., Trick, H. N. and Kochian, L. V. (2007) A gene in the multidrug and toxic compound extrusion (MATE) family confers aluminum tolerance in sorghum. *Nat. Genet*. **39**, 1156-1161.

Mancuso, M. R., Davis, R., Norberg, S. M., O'Brien, S., Sennino, B., Nakahara, T., Yao, V. J., Inai, T., Brooks, P., Freimark, B., Shalinsky, D. R., Hu-Lowe, D. D. and McDonald, D. M. (2006) Rapid vascular

regrowth in tumors after reversal of VEGF inhibition. *J. Clin. Invest.* **116**, 2610-2621.

Marinova, K., Pourcel, L., Weder, B., Schwarz, M., Barron, D., Routaboul, J. M., Debeaujon, I. and Klein, M. (2007) The *Arabidopsis* MATE transporter TT12 acts as a vacuolar flavonoid/H^+-antiporter active in proanthocyanidin-accumulating cells of the seed coat. *Plant Cell* **19**, 2023-2038.

Meguro, R., Asano, Y., Odagiri, S., Li, C., Iwatsuki, H. and Shoumura, K. (2007) Nonheme-iron histochemistry for light and electron microscopy: a historical, theoretical and technical review. *Arch. Histol. Cytol.* **70**, 1-19.

Melcher, K., Ng, L. M., Zhou, X. E., Soon, F. F., Xu, Y., Suino-Powell, K. M., Park, S. Y., Weiner, J. J., Fujii, H., Chinnusamy, V., Kovach, A., Li, J., Wang, Y., Li, J., Peterson, F. C., Jensen, D. R., Yong, E. L., Volkman, B. F., Cutler, S. R., Zhu, J. K. and Xu, H. E. (2009) A gate-latch-lock mechanism for hormone signalling by abscisic acid receptors. *Nature* **462**, 602-608.

Mistri, T., Alam, R., Dolai, M., Mandal, S. K., Khuda-Bukhsh, A. R. and Ali, M. (2013) A 7-nitrobenz-2-oxa-1,3-diazole based highly sensitive and selective turn-on chemosensor for copper(II) ion with intracellular application without cytotoxicity. *Org. Biomol. Chem.* **11**, 1563-1569.

Miura, K., Jin, J. B., Lee, J., Yoo, C. Y., Stirm, V., Miura, T., Ashworth, E. N., Bressan, R. A., Yun, D. J. and Hasegawa, P. M. (2007) SIZ1-mediated sumoylation of ICE1 controls *CBF3/DREB1A* expression and freezing tolerance in *Arabidopsis*. *Plant Cell* **19**, 1403-1414.

Mizoguchi, M., Umezawa, T., Nakashima, K., Kidokoro, S., Takasaki, H., Fujita, Y., Yamaguchi-Shinozaki, K. and Shinozaki, K. (2010) Two closely related subclass II SnRK2 protein kinases cooperatively regulate drought-inducible gene expression. *Plant Cell Physiol*. **51**, 842-847.

Mok, J., Kim, P. M., Lam, H. Y., Piccirillo, S., Zhou, X., Jeschke, G. R., Sheridan, D. L., Parker, S. A., Desai, V., Jwa, M. Cameroni, E., Niu, H., Good, M., Remenyi, A., Ma, J. L., Sheu, Y. J., Sassi, H. E., Sopko, R., Chan, C. S., De Virgilio, C., Hollingsworth, N. M., Lim, W. A., Stern, D. F., Stillman, B., Andrews, B. J., Gerstein, M. B., Snyder, M. and Turk, B. E. (2010) Deciphering protein kinase specificity through large-scale analysis of yeast phosphorylation site motifs. *Sci. Signaling* **3**, ra12.

Mori, S. (1999) Iron acquisition by plants. *Curr. Opin. Plant Biol*. **2**, 250-253.

Morita, Y., Kodama, K., Shiota, S., Mine, T., Kataoka, A., Mizushima, T. and Tsuchiya, T. (1998) NorM, a putative multidrug efflux protein, of *Vibrio parahaemolyticus* and its homolog in *Escherichia coli*. *Antimicrob. Agents Chemother.* **42**, 1778-1782.

Morita, Y., Kataoka, A., Shiota, S., Mizushima, T. and Tsuchiya, T. (2000) NorM of *vibrio parahaemolyticus* is an Na^+-driven multidrug efflux pump. *J. Bacteriol.* **182**, 6694-6697.

Murgia, I., Vazzola, V., Tarantino, D., Cellier, F., Ravet, K., Briat, J. F. and Soave, C. (2007) Knock-out of ferritin *AtFer1* causes earlier onset of age-dependent leaf senescence in *Arabidopsis*. *Plant Physiol. Biochem.* **45**,

898-907.

Mustilli, A. C., Merlot, S., Vavasseur, A., Fenzi, F. and Giraudat, J. (2002) *Arabidopsis* OST1 protein kinase mediates the regulation of stomatal aperture by abscisic acid and acts upstream of reactive oxygen species production. *Plant Cell* **14**, 3089-3099.

Nakashima, K., Fujita, Y., Kanamori, N., Katagiri, T., Umezawa, T., Kidokoro, S., Maruyama, K., Yoshida, T., Ishiyama, K., Kobayashi, M., Shinozaki, K. and Yamaguchi-Shinozaki, K. (2009) Three *Arabidopsis* SnRK2 protein kinases, SRK2D/SnRK2.2, SRK2E/SnRK2.6/OST1 and SRK2I/SnRK2.3, involved in ABA signaling are essential for the control of seed development and dormancy. *Plant Cell Physiol*. **50**, 1345-1363.

Nardozzi, J. D., Lott, K. and Cingolani, G. (2010) Phosphorylation meets nuclear import: a review. *Cell Commun. Signaling* **8**, 32-48.

Nawrath, C., Heck, S., Parinthawong, N. and M´etraux, J. P. (2002) EDS5, an essential component of salicylic acid-dependent signaling for disease resistance in *Arabidopsis*, is a member of the MATE transporter family. *Plant Cell* **14**, 275-286.

Noh, Y. S. and Amasino, R. M. (1999) Identification of a promoter region responsible for the senescence-specific expression of *SAG12*. *Plant Mol. Biol.* **41**, 181-194.

Oh, S. A., Park, J. H., Lee, G. I., Paek, K. H., Park, S. K. and Nam, H. G. (1997) Identification of three genetic loci controlling leaf senescence in *Arabidopsis thaliana*. *Plant J.* **12**, 527-535.

Olsen, A. N., Ernst, H. A., Leggio, L. L. and Skriver, K. (2005) DNA-binding specificity and molecular functions of NAC transcription factors. *Plant Sci*. **169**, 785-797.

Omote, H., Hiasa, M., Matsumoto, T., Otsuka, M. and Moriyama, Y. (2006) The MATE proteins as fundamental transporters of metabolic and xenobiotic organic cations. *Trends Pharmacol. Sci*. **27**, 587-593.

Onouchi, H., Igeño, M. I., Périlleux, C., Graves, K. and Coupland, G. (2000) Mutagenesis of plants overexpressing *CONSTANS* demonstrates novel interactions among *Arabidopsis* flowering-time genes. *Plant Cell* **12**, 885-900.

Park, S. Y., Fung, P., Nishimura, N., Jensen, D. R., Fujii, H., Zhao, Y., Lumba, S., Santiago, J., Rodrigues, A., Chow, T. F., Alfred, S. E., Bonetta, D., Finkelstein, R., Provart, N. J., Desveaux, D., Rodriguez, P. L., McCourt, P., Zhu, J. K., Schroeder, J. I., Volkman, B. F. and Cutler, S. R. (2009) Abscisic acid inhibits type 2C protein phosphatases via the PYR/PYL family of START proteins. *Science* **324**, 1068-1071.

Petit, J. M., Briat, J. F. and Lobr´eaux, S. (2001) Structure and differential expression of the four members of the *Arabidopsis thaliana* ferritin gene family. *Biochem. J.* **359**, 575-582.

Ramachandram, B. and Samanta A. (1998) Transition metal ion induced fluorescence enhancement of 4-(N,N-Dimethylethylenediamino)-7-nitrobenz-2-oxa-1,3-diazole *J. Phys. Chem. A*. **102**, 10579-10587.

Ravet, K., Touraine, B., Boucherez, J., Briat, J. F., Gaymard, F. and Cellier,

F. (2009) Ferritins control interaction between iron homeostasis and oxidative stress in *Arabidopsis*. *Plant J.* **57**, 400-41.

Rayson, S., Arciga-Reyes, L., Wootton, L., De Torres Zabala, M., Truman, W., Graham, N., Grant, M. and Davies, B. (2012) A role for nonsense-mediated mRNA decay in plants: pathogen responses are induced in *Arabidopsis thaliana* NMD mutants. *PLoS One* **7**, e31917.

Robinson, N. J., Procter, C. M., Connolly, E. L. and Guerinot, M. L. (1999) A ferric-chelate reductase for iron uptake from soils. *Nature* **397**, 694-697.

Rogers, E. E. and Guerinot, M. L. (2002) FRD3, a member of the multidrug and toxin efflux family, controls iron deficiency responses in *Arabidopsis*. *Plant Cell* **14**, 1787-1799.

Roschzttardtz, H., Conéjéro, G., Curie, C. and Mari, S. (2009) Identification of the endodermal vacuole as the iron storage compartment in the *Arabidopsis* embryo. *Plant Physiol*. **151**, 1329-1338.

Roschzttardtz, H., Conéjéro, G., Divol, F., Alcon, C., Verdeil, J. L., Curie, C. and Mari, S. (2013) New insights into Fe localization in plant tissues. *Front. Plant Sci*. **4**, 350.

Russin, W. A., Evert, R. F., Vanderveer, P. J., Sharkey, T. D. and Briggs, S. P. (1996) Modification of a specific class of plasmodesmata and loss of sucrose export ability in the sucrose export defective1 maize mutant. *Plant Cell* **8**, 645-658.

Ryu, H., Kim, K., Cho, H., Park, J., Choe, S. and Hwang, I. (2007)

Nucleocytoplasmic shuttling of BZR1 mediated by phosphorylation is essential in *Arabidopsis* brassinosteroid signaling. *Plant Cell* **19**, 2749-2762.

Sahoo, S. K., Sharma, D., Bera, R. K., Crisponi, G. and Callan, J. F. (2012) Iron(III) selective molecular and supramolecular fluorescent probes. *Chem. Soc. Rev*. **41**, 7195-7227.

Samach, A., Onouchi, H., Gold, S. E., Ditta, G. S., Schwarz-Sommer, Z., Yanofsky, M. F. and Coupland, G. (2000) Distinct roles of CONSTANS target genes in reproductive development of *Arabidopsis*. *Science* **288**, 1613-1616.

Sato, A., Sato, Y., Fukao, Y., Fujiwara, M., Umezawa, T., Shinozaki, K., Hibi, T., Taniguchi, M., Miyake, H., Goto, D. B. and Uozumi, N. (2009) Threonine at position 306 of the KAT1 potassium channel is essential for channel activity and is a target site for ABA-activated SnRK2/OST1/SnRK2.6 protein kinase. *Biochem. J.* **424**, 439-448.

Seeger, M. A., Diederichs, K., Eicher, T., Brandst¨atter, L., Schiefner, A., Verrey, F. and Pos, K. M. (2008) The AcrB efflux pump: conformational cycling and peristalsis lead to multidrug resistance. *Curr. Drug Targets* **9**, 729-749.

Séguéla, M., Briat, J. F., Vert, G. and Curie, C. (2008) Cytokinins negatively regulate the root iron uptake machinery in *Arabidopsis* through a growth-dependent pathway. *Plant J.* **55**, 289-300.

Seo, P. J., Kim, M. J., Park, J. Y., Kim, S. Y., Jeon, J., Lee, Y. H., Kim, J. and Park, C. M. (2010) Cold activation of a plasma

membrane-tethered NAC transcription factor induces a pathogen resistance response in *Arabidopsis*. *Plant J*. **61**, 661-671.

Seo, P. J., Kim, M. J., Ryu, J. Y., Jeong, E. Y. and Park, C. M. (2011) Two splice variants of the IDD14 transcription factor competitively form nonfunctional heterodimers which may regulate starch metabolism. *Nat. Commun.* **2**:303.

Seo, P. J. and Park, C. M. (2010) A membrane-bound NAC transcription factor as an integrator of biotic and abiotic stress signals. *Plant Signaling Behav*. **5**, 481-483.

Seo, P. J., Park, J., Park, M. J., Kim, Y. S., Kim, S. G., Jung, J. H. and Park, C. M. (2012a) A Golgi-localized MATE transporter mediates iron homeostasis under osmotic stress in *Arabidopsis*. *Biochem. J*. **442**, 551-561.

Seo, P. J., Park, M. J., Lim, M. H., Kim, S. G., Lee, M., Baldwin, I. T. and Park, C. M. (2012b) A self-regulatory circuit of CIRCADIAN CLOCK-ASSOCIATED1 underlies the circadian clock regulation of temperature responses in *Arabidopsis*. *Plant Cell* **24**, 2427-2442.

Seo, P. J., Xiang, F., Qiao, M., Park, J. Y., Lee, Y. N., Kim, S. G., Lee, Y. H., Park, W. J. and Park, C. M. (2009) The MYB96 transcription factor mediates abscisic acid signaling during drought stress response in *Arabidopsis*. *Plant Physiol.* **151**, 275-289.

Seltmann, M. A., Stingl, N. E., Lautenschlaeger, J. K., Krischke, M., Mueller, M. J. and Berger, S. (2010) Differential impact of lipoxygenase 2 and jasmonates on natural and stress-induced senescence in

Arabidopsis. *Plant Physiol*. **152**, 1940-1950.

Shikanai, T., Müller-Moulé, P., Munekage, Y., Niyogi, K. K. and Pilon, M. (2003) PAA1, a P-type ATPase of *Arabidopsis*, functions in copper transport in chloroplasts. *Plant Cell* **15**, 1333-1346.

Shin, R., Alvarez, S., Burch, A. Y., Jez, J. M. and Schachtman, D. P. (2007) Phosphoproteomic identification of targets of the *Arabidopsis* sucrose nonfermenting-like kinase SnRK2.8 reveals a connection to metabolic processes. *Proc. Natl. Acad. Sci. U.S.A*. **104**, 6460-6465.

Sirichandra, C., Gu, D., Hu, H. C., Davanture, M., Lee, S., Djaoui, M., Valot, B., Zivy, M., Leung, J., Merlot, S. and Kwak, J. M. (2009) Phosphorylation of the *Arabidopsis* AtrbohF NADPH oxidase by OST1 protein kinase. *FEBS Lett*. **583**, 2982-2986.

Song, Y. H., Estrada, D. A., Johnson, R. S., Kim, S. K., Lee, S. Y., MacCoss, M. J., and Imaizumi, T. (2014) Distinct roles of FKF1, GIGANTEA, and ZEITLUPE proteins in the regulation of CONSTANS stability in *Arabidopsis* photoperiodic flowering. *Proc. Natl. Acad. Sci. U.S.A*. **111**, 17672-17677.

Song, Y. H., Ito, S. and Imaizumi, T. (2013) Flowering time regulation: photoperiod- and temperature-sensing in leaves. *Trends Plant Sci.* **18**, 575-583.

Song, Y. H., Lee, I., Lee, S. Y., Imaizumi, T. and Hong, J. C. (2012a) CONSTANS and ASYMMETRIC LEAVES 1 complex is involved in the induction of *FLOWERING LOCUS T* in photoperiodic flowering in *Arabidopsis*. *Plant J.* **69**, 332-342.

Song, Y. H., Smith, R. W., To, B. J., Millar, A. J. and Imaizumi, T. (2012b) FKF1 conveys timing information for CONSTANS stabilization in photoperiodic flowering. *Science* **336**, 1045-1049.

Srivastava, R., Chen, Y., Deng, Y., Brandizzi, F. and Howell, S. H. (2012) Elements proximal to and within the transmembrane domain mediate the organelle-to-organelle movement of bZIP28 under ER stress conditions. *Plant J.* **70**, 1033-1042.

Stacey, M. G., Patel, A., McClain, W. E., Mathieu, M., Remley, M., Rogers, E. E., Gassmann, W., Blevins, D. G. and Stacey, G. (2008) The *Arabidopsis* AtOPT3 protein functions in metal homeostasis and movement of iron to developing seeds. *Plant Physiol.* **146**, 589-601.

Staiger, D. (2002) Chemical strategies for iron acquisition in plants. *Angew. Chem. Int. Ed. Engl.* **41**, 2259-2264.

Staiger, D. and Brown, J. W. (2013) Alternative splicing at the intersection of biological timing, development, and stress responses. *Plant Cell* **25**, 3640-56.

Suárez-López, P., Wheatley, K., Robson, F., Onouchi, H., Valverde, F. and Coupland, G. (2001) *CONSTANS* mediates between the circadian clock and the control of flowering in *Arabidopsis*. *Nature* **410**, 1116-1120.

Tarantino, D., Petit, J. M., Lobreaux, S., Briat, J. F., Soave, C. and Murgia, I. (2003) Differential involvement of the IDRS cis-element in the developmental and environmental regulation of the *AtFer1* ferritin gene from *Arabidopsis*. *Planta* **217**, 709-716.

Tiwari, S. B., Hagen, G. and Guilfoyle, T. (2003) The roles of auxin response factor domains in auxin-responsive transcription. *Plant Cell* **15**, 533-543.

Tiwari, S. B., Shen, Y., Chang, H. C., Hou, Y., Harris, A., Ma, S. F., McPartland, M., Hymus, G. J., Adam, L., Marion, C., Belachew, A., Repetti, P. P., Reuber, T. L. and Ratcliffe, O. J. (2010) The flowering time regulator CONSTANS is recruited to the *FLOWERING LOCUS T* promoter via a unique *cis*-element. *New Phytol.* **187**, 57-66.

Tsubuki, S., Saito, Y., Tomioka, M., Ito, H. and Kawashima, S. (1996) Differential inhibition of calpain and proteasome activities by peptidyl aldehydes of di-leucine and tri-leucine. *J. Biochem.* **119**, 572-576.

Touzé, T., Eswaran, J., Bokma, E., Koronakis, E., Hughes, C. and Koronakis, V. (2004) Interactions underlying assembly of the *Escherichia coli* AcrAB-TolC multidrug efflux system. *Mol. Microbiol.* **53**, 697-706.

Udvardi, M. K., Czechowski, T. and Scheible, W. R. (2008) Eleven golden rules of quantitative RT-PCR. *Plant Cell* **20**, 1736-1737.

Uno, Y., Furihata, T., Abe, H., Yoshida, R., Shinozaki, K. and Yamaguchi-Shinozaki, K. (2000) *Arabidopsis* basic leucine zipper transcription factors involved in an abscisic acid-dependent signal transduction pathway under drought and high-salinity conditions. *Proc. Natl. Acad. Sci. U.S.A.* **97**, 11632-11637.

Umezawa, T., Nakashima, K., Miyakawa, T., Kuromori, T., Tanokura, M., Shinozaki, K. and Yamaguchi-Shinozaki, K. (2010) Molecular basis of

the core regulatory network in ABA responses: sensing, signaling and transport. *Plant Cell Physiol*. **51**, 1821-1839.

Umezawa, T., Yoshida, R., Maruyama, K., Yamaguchi-Shinozaki, K. and Shinozaki, K. (2004) SRK2C, a SNF1-related protein kinase2, improves drought tolerance by controlling stress-responsive gene expression in *Arabidopsis thaliana. Proc. Natl. Acad. Sci. U.S.A.* **101**, 17306-17311.

Vahisalu, T., Puzõrjova, I., Brosch´e, M., Valk, E., Lepiku, M., Moldau, H., Pechter, P., Wang, Y. S., Lindgren, O., Salojärvi, J. Loog, M., Kangasjärvi, J. and Kollist, H. (2010) Ozone-triggered rapid stomatal response involves the production of reactive oxygen species, and is controlled by SLAC1 and OST1. *Plant J.* **62**, 442-453.

Valverde, F., Mouradov, A., Soppe, W., Ravenscroft, D., Samach, A. and Coupland, G. (2004) Photoreceptor regulation of CONSTANS protein in photoperiodic flowering. *Science* **303**, 1003-1006.

Varotto, C., Maiwald, D., Pesaresi, P., Jahns, P., Salamini, F. and Leister, D. (2002) The metal ion transporter IRT1 is necessary for iron homeostasis and efficient photosynthesis in *Arabidopsis thaliana*. *Plant J.* **31**, 589-599.

Vert, G. and Chory, J. (2006) Downstream nuclear events in brassinosteroid signalling. *Nature* **441**, 96-100.

Vert, G., Grotz, N., Dédaldéchamp, F., Gaymard, F., Guerinot, M. L., Briat, J. F. and Curie, C. (2002) IRT1, an *Arabidopsis* transporter essential for iron uptake from the soil and for plant growth. *Plant Cell* **14**, 1223-1233.

Vinson, C. R., Hai, T. and Boyd, S. M. (1993) Dimerization specificity of the leucine zipper-containing bZIP motif on DNA binding: Prediction and rational design. *Genes Dev.* **7**, 1047-1058.

Voiniciuc, C., Dean, G. H., Griffiths, J. S., Kirchsteiger, K., Hwang, Y. T., Gillett, A., Dow, G., Western, T. L., Estelle, M. and Haughn, G. W. (2013) Flying saucer1 is a transmembrane RING E3 ubiquitin ligase that regulates the degree of pectin methylesterification in *Arabidopsis* seed mucilage. *Plant Cell* **25**, 944-959.

Wang, B. B. and Brendel, V. (2006) Genomewide comparative analysis of alternative splicing in plants. *Proc. Natl. Acad. Sci. U.S.A* **103**, 7175-7180.

Waters, B. M., Chu, H. H., Didonato, R. J., Roberts, L. A., Eisley, R. B., Lahner, B., Salt, D. E. and Walker, E. L. (2006) Mutations in *Arabidopsis yellow stripe-like1* and *yellow stripe-like3* reveal their roles in metal ion homeostasis and loading of metal ions in seeds. *Plant Physiol*. **141**, 1446-1458.

Weiner, J. J., Peterson, F. C., Volkman, B. F. and Cutler, S. R. (2010) Structural and functional insights into core ABA signaling. *Curr. Opin. Plant Biol.* **13**, 495-502.

Weigel, D., Ahn, J. H., Bl´azquez, M. A., Borevitz, J. O., Christensen, S. K., Fankhauser, C., Ferrándiz, C., Kardailsky, I., Malancharuvil, E. J., Neff, M. M., Nguyen, J. T., Sato, S., Wang, Z. Y., Xia, Y., Dixon, R. A., Harrison, M. J., Lamb, C. J., Yanofsky, M. F. and Chory, J. (2000) Activation tagging in *Arabidopsis*. *Plant Physiol*. **122**, 1003-1013.

Wenkel, S., Turck, F., Singer, K., Gissot, L., Le Gourrierec, J., Samach, A. and Coupland, G. (2006) CONSTANS and the CCAAT box binding complex share a functionally important domain and interact to regulate flowering of *Arabidopsis*. *Plant Cell* **18**, 2971-2984.

Whelan, J. A., Russell, N. B. and Whelan, M. A. (2003) A method for the absolute quantification of cDNA using real-time PCR. *J. Immunol. Methods* **278**, 261-269.

Xiao, Y. and Qian, X. (2003) Novel highly efficient fluoroionophores with a peri-effect and strong electron-donating receptors: TICT-promoted PET and signaling response to transition metal cations with low background emission. *Tetrahedron Lett*. **44**, 2087-2091.

Xu, Z. S., Liu, L., Ni, Z. Y., Liu, P., Chen, M., Li, L. C., Chen, Y. F. and Ma, Y. Z. (2009) W55a encodes a novel protein kinase that is involved in multiple stress responses. *J. Integr. Plant Biol*. **51**, 58-66.

Yang, S. D., Seo, P. J., Yoon, H. K. and Park, C. M. (2011) The *Arabidopsis* NAC transcription factor VNI2 integrates abscisic acid signals into leaf senescence via the *COR/RD* genes. *Plant Cell* **23**, 2155-2168.

Yi, Y. and Guerinot, M. L. (1996) Genetic evidence that induction of root Fe(III) chelate reductase activity is necessary for iron uptake under iron deficiency. *Plant J.* **10**, 835-844.

Yoo, S. D., Cho, Y. H. and Sheen, J. (2007) *Arabidopsis* mesophyll protoplasts: a versatile cell system for transient gene expression analysis. *Nat. Protoc.* **2**, 1565-1572.

Yoon, H. K., Kim, S. G., Kim, S. Y. and Park, C. M. (2008) Regulation of leaf senescence by NTL9-mediated osmotic stress signaling in *Arabidopsis*. *Mol. Cells* **25**, 438-445.

Yoshida, T., Fujita, Y., Sayama, H., Kidokoro, S., Maruyama, K., Mizoi, J., Shinozaki, K. and Yamaguchi-Shinozaki, K. (2010) AREB1, AREB2, and ABF3 are master transcription factors that cooperatively regulate ABRE-dependent ABA signaling involved in drought stress tolerance and require ABA for full activation. *Plant J.* **61**, 672-685.

Yoshida, R., Hobo, T., Ichimura, K., Mizoguchi, T., Takahashi, F., Aronso, J., Ecker, J. R. and Shinozaki, K. (2002) ABA-activated SnRK2 protein kinase is required for dehydration stress signaling in *Arabidopsis*. *Plant Cell Physiol*. **43**, 1473-1483.

Yoshida, R., Umezawa, T., Mizoguchi, T., Takahashi, S., Takahashi, F. and Shinozaki, K. (2006) The regulatory domain of SRK2E/OST1/SnRK2.6 interacts with ABI1 and integrates abscisic acid (ABA) and osmotic stress signals controlling stomatal closure in *Arabidopsis*. *J. Biol. Chem*. **281**, 5310-5318.

Yuan, Y., Wu, H., Wang, N., Li, J., Zhao, W., Du, J., Wang, D. and Ling, H. Q. (2008) FIT interacts with AtbHLH38 and AtbHLH39 in regulating iron uptake gene expression for iron homeostasis in *Arabidopsis*. *Cell Res*. **18**, 385-397.

Yuan, Y. X., Zhang, J., Wang, D. W. and Ling, H. Q. (2005) AtbHLH29 of *Arabidopsis thaliana* is a functional ortholog of tomato FER involved in controlling iron acquisition in strategy I plants. *Cell Res.* **15**, 613-621.

Zancani, M., Peresson, C., Biroccio, A., Federici, G., Urbani, A., Murgia, I., Soave, C., Micali, F., Vianello, A. and Macr`ı, F. (2004) Evidence for the presence of ferritin in plant mitochondria. *Eur. J. Biochem*. **271**, 3657-3664.

Zhao, J. and Dixon, R. A. (2009) MATE transporters facilitate vacuolar uptake of epicatechin 3'-O-glucoside for proanthocyanidin biosynthesis in *Medicago truncatula* and *Arabidopsis*. *Plant Cell* **21**, 2323-2340.

Zhu, G., Fujii, K., Liu, Y., Codrea, V., Herrero, J. and Shaw, S. (2005) A single pair of acidic residues in the kinase major groove mediates strong substrate preference for P-2 or P-5 arginine in the AGC, CAMK, and STE kinase families. *J. Biol. Chem*. **280**, 36372-36379.

Zuo, J., Niu, Q. W. and Chua, N. H. (2000) An estrogen receptor-based transactivator XVE mediates highly inducible gene expression in transgenic plants. *Plant J.* **24**, 265-273.

PUBLICATION LIST

1. **Park, M. J.***, Jung, H. S.*, Kim, Y. J., Kwon, Y. J., Lee, J. K. and Park, C. M. (2014) High-sensitivity fluorescence imaging of iron in plant tissues. *Chem. Commun.* **50**, 8547-8549. (*equal contribution)

2. Kwon, Y. J.*, **Park, M. J.***, Kim, S. G., Baldwin, I. T. and Park, C. M. (2014) Alternative splicing and nonsense-mediated decay of circadian clock genes under environmental stress conditions in *Arabidopsis*. *BMC Plant Biol.* **14**, 136. (*equal contribution)

3. Jung, J. H.*, Lee, H. J.*, **Park, M. J.*** and Park, C. M. (2014) Beyond ubiquitination: proteolytic and nonproteolytic roles of HOS1. *Trends Plant Sci.* **19**, 538-545. (*equal contribution)

4. Seo, P. J., **Park, M. J.** and Park, C. M. (2013) Alternative splicing of transcription factors in plant responses to low temperature stress: mechanisms and functions. *Planta* **237**, 1415-1424.

5. Seo, P. J.*, Jung, J. H.*, **Park, M. J.**, Lee, K. and Park, C. M. (2013) Controlled turnover of CONSTANS protein by the HOS1 E3 ligase regulates floral transition at low temperatures. *Plant Signal. Behav.* **8**, e23780 (*equal contribution)

6. Kim, M. J.*, **Park, M. J.***, Seo, P. J.*, Song, J. S., Kim, H. J. and Park, C. M. (2012) Controlled nuclear import of the transcription factor NTL6 reveals a cytoplasmic role of SnRK2.8 in the drought-stress response. *Biochem. J.* **448**, 353-363. (*equal contribution)

7. **Park, M. J.**, Seo, P. J. and Park, C. M. (2012) CCA1 alternative splicing as a way of linking the circadian clock to temperature response in *Arabidopsis*. *Plant Signal. Behav.* **7**, 1194-1196.

8. Seo, P. J., **Park, M. J.**, Lim, M. H., Kim, S. G., Lee, M., Baldwin, I. T. and Park, C. M. (2012) A self-regulatory circuit of CIRCADIAN CLOCK-ASSOCIATED1 underlies the circadian clock regulation of temperature responses in *Arabidopsis*. *Plant Cell* **24**, 2427-2442.

9. Seo, P. J.*, Park, J.*, **Park, M. J.***, Kim, Y. S, Kim, S. G., Jung, J. H. and Park, C. M. (2012) A Golgi-localized MATE transporter mediates iron homeostasis under osmotic stress in *Arabidopsis*. *Biochem. J.* **442**, 551-561. (*equal contribution)

10. Seo, P. J.*, Lee, S. B.*, Suh, M. C., **Park, M. J.**, Go, Y. S. and Park, C. M. (2011) The MYB96 transcription factor regulates cuticular wax biosynthesis under drought conditions in *Arabidopsis*. *Plant Cell* **23**, 1138-1152. (*equal contribution)

국문초록

식물은 동물과 다르게 일생을 한 장소에서 살아가며, 살아가기 부적절한 환경으로부터 회피할 수도 없다. 그 결과 식물은 여러 가지 환경 조건을 인지하고, 이에 적응하기 위한 다양하고 효과적인 전략들을 진화적으로 얻게 되었다. 예컨대, 막결합 전사인자의 막으로부터 이탈은 급격한 환경 스트레스에 식물이 보다 빠르게 반응하는 데 기여함이 잘 알려져 있다.

본 연구에서는 식물이 환경 변화에 대응하는 여러 가지 메커니즘에 대해 알아보았다.

1장에서는 막결합 전사인자의 조절 기작에 대해 살펴보았다. NTL6는 애기장대의 원형질막에 결합한 상태로 존재하는 전사인자로 가뭄 저항성 증가에 기여한다. SnRK2.8은 세포질에서 NTL6와 상호작용을 하며, 특히 SnRK2.8은 NTL6의 142번째 아미노산인 Thr (Thr^{142})을 인산화함을 증명하였다. 또한 SnRK2.8에 의한 NTL6의 인산화는 NTL6의 세포핵으로의 이동에 필요함을 알 수 있었다. 게다가 NTL6 과량발현식물의 가뭄저항성 표현형은 *snrk2.8-1* 돌연변이에 의해 감소되었다. 이러한 결과들은 SnRK2.8에 의한 인산화와, 막으로부터의 이탈 모두 NTL6에 의한 가뭄 저항성 증가에 중요함을 가리킨다.

2장에서는 삼투 스트레스 하에서의 철 항상성 유지에 있어서 BCD1의 기능을 연구하였다. *BCD1* 유전자의 발현은 과량의 철에 의해 증가하고, 철의 결핍에 의해 감소한다. 또한 고염분이나 가뭄과 같은 삼투 스트레스에 의해서도 발현이 증가한다. *BCD1*의 발현이 증대된 *bcd1-D* 돌연변이는 정상식물에 비해 식물체 내 철 함량이 감소한 반면, *bcd1-1* 돌연변이는 반대로 철 함량이 증가하였다. 또한 BCD1은 세포 내에서 골지체 부분에 존재함을 확인하였다. 이러한 관찰들을 바탕으로, BCD1이 스트레스에 의한 세포 손상에 의해 발생하는 과량의 철을 재분배함으로써 철 항상성 유지에 기여할 것으로 생각할 수 있다.

식물에서 철에 대해 연구할 때에, Perls staining과 같은 전통적인 조직화학적 염색법들이 널리 쓰이고 있다. 본 연구에서도 2장에서 애기

장대 내 철의 위치를 확인하기 위하여 Perls staining 방법을 사용하였다. 그러나 이 방법은 낮은 해상도와 비교적 높은 검출 한계라는 한계를 가지고 있다. 이에 식물체 내 철 검출을 개선하기 위하여, **3장**에서는 새로운 철 형광 검출법에 대해 소개하고자 한다. 이 방법은 기존의 방법보다 비교적 정확하게 식물 조직 내 철의 양과 분포를 알 수 있다.

계절 변화에 따른 낮의 길이 변화는 식물의 개화시기를 결정하는 중요한 환경 요인 중 하나이다. 애기장대에서는 생체시계와 빛 신호에 의해 조절되는 CO 단백질의 일주기 리듬이 낮의 길이 인지 및 광주기에 따른 개화시기 조절에 있어서 중심적인 역할을 한다. 이러한 CO 단백질의 일주기 리듬을 조절하는 다양한 메커니즘이 알려졌으나, 아직 CO 자체가 이러한 조절에 어떠한 기여를 하는지는 연구된 바 없다. **4장**에서는 CO가 선택적 재조합에 의해 두 가지 단백질 동형 (isoform), 기존에 알려진 CO 단백질과 같은 COα 단백질과 C말단이 줄어든 COβ 단백질을 만들어 냄을 확인하였다. 특히, COβ 단백질은 COα 단백질과 E3 효소들과의 상호작용에 영향을 미침으로써 COα 단백질의 분해를 촉진함을 확인하였으며, 이는 CO가 자신의 단백질 일주기 리듬 조절에 기여함을 의미한다.

주요어 : 막 결합 전사인자, 철 항상성, 생체 내 철 형광 검출, 광주기, 개화시기, 선택적 재조합

학번 : 2010-20277